UFBA

UNIVERSIDADE FEDERAL DA BAHIA
ESCOLA POLITÉCNICA
PROGRAMA DE PÓS GRADUAÇÃO EM ENGENHARIA INDUSTRIAL - PEI

MESTRADO EM ENGENHARIA INDUSTRIAL

FERNANDO ANTONIO SOARES CALHAU

Simple model predictive control strategies coupled to artificial intelligence-based disturbance modeling for microgrid energy management system

PEI
Programa de Pós-Graduação em Engenharia Industrial

SIMPLE MODEL PREDICTIVE CONTROL STRATEGIES COUPLED TO ARTIFICIAL INTELLIGENCE-BASED DISTURBANCE MODELING FOR MICROGRID ENERGY MANAGEMENT SYSTEM

Fernando Antonio Soares Calhau

Dissertação de Mestrado apresentada ao Programa de Pós-graduação em Engenharia Industrial, da Universidade Federal da Bahia, como parte dos requisitos necessários à obtenção do título de Mestre em Engenharia Industrial.

Orientadores: Márcio A. F. Martins
Rodrigo L. Meira

Salvador
Agosto de 2025

C152 Calhau, Fernando Antonio Soares.

Simple model predictive control strategies coupled to artificial intelligence-based disturbance modeling for microgrid energy management system / Fernando Antonio Soares Calhau. – Salvador, 2025.

125f.: il.; color.

Orientadores: Prof. Dr. Márcio A. F. Martins.
Prof. Dr. Rodrigo L. Meira.

Dissertação (mestrado) – Programa de Pós-Graduação em Engenharia Industrial, Escola Politécnica, Universidade Federal da Bahia, 2025.

1. Controle preditivo. 2. Energia – sistema de gerenciamento. 3. Inteligência artificial. I. Martins, Márcio A. F. II. Meira, Rodrigo L. III. Universidade Federal da Bahia. IV. Título.

CDD: 629.836

Ficha catalográfica elaborada pela Biblioteca Bernadete Sinay Neves, Escola Politécnica – UFBA.

Simple model predictive control strategies coupled to artificial intelligence-based disturbance modeling for microgrid energy management system

Fernando Antonio Soares Calhau

Dissertação submetida ao corpo docente do programa de pós-graduação em Engenharia Industrial da Universidade Federal da Bahia como parte dos requisitos necessários para a obtenção do grau de mestre em Engenharia Industrial.

Examinada por:

gov.br Documento assinado digitalmente
RAONY MAIA FONTES
Data: 28/08/2025 13:48:40-0300
Verifique em https://validar.iti.gov.br

Prof. Dr. Raony Maia Fontes _____
Doutor em Engenharia Industrial, pela Universidade Federal da Bahia, Brasil, 2023

gov.br Documento assinado digitalmente
ARIOSTON ARAUJO DE MORAIS JUNIOR
Data: 28/08/2025 15:50:07-0300
Verifique em https://validar.iti.gov.br

Prof. Dr. Arioston Araújo de Morais Júnior _____
Doutor em Engenharia Química, pela Universidade Federal de Campina Grande, Brasil, 2015

gov.br Documento assinado digitalmente
HELENO BISPO DA SILVA JUNIOR
Data: 29/08/2025 07:46:27-0300
Verifique em https://validar.iti.gov.br

Prof. Dr. Heleno Bispo da Silva Júnior _____
Doutor em Engenharia Química, pela Universidade Federal de Campina Grande, Brasil, 2014

Salvador, BA - BRASIL
Agosto/2025

A minha mãe, minha avó, minha irmã, minha famlía e amigos.

Agradecimentos

A elaboração de um trabalho intelectual, como esta dissertação, não é fruto apenas do esforço individual, mas também do encontro de muitas presenças, palavras e gestos que sustentam o caminhar. Ela se ergue sobre ombros de gigantes, que permitem vislumbrar o pequeno feixe de contribuição que aqui se insere, e sobre os abraços, incentivos e silêncios atentos daqueles que nos acompanham, mesmo nas tempestades interiores que a vida acadêmica inevitavelmente impõe. A todos que, de alguma forma, fizeram parte desta jornada, registro minha mais profunda gratidão.

Primeiramente, agradeço Àquele que, mesmo quando caminho pelo vale da sombra da morte, me faz não temer mal algum, pois está comigo. Nos momentos em que duvidei de mim mesmo, Ele foi o meu refúgio, conduzindo-me à sombra do Onipotente e concedendo-me forças para enfrentar as batalhas que se instalaram no meu âmago.

À minha mãe, sempre ao meu lado, e de quem herdei a curiosidade insaciável pelo mundo, minha eterna gratidão. À minha avó, que, nos leitos eternos do Senhor, guiou-me até aqui e foi a primeira a despertar em mim o prazer de resolver problemas matemáticos, mesmo sem ter concluído a quarta série. À minha irmã, pelo apoio constante e pelo incentivo a nunca desistir; à minha tia, pelos risos nos momentos de tensão, mesmo sem perceber o quanto eram necessários; ao meu cunhado, pelas conversas e conselhos; ao meu primo Murilo, confidente nos momentos críticos; e a toda a minha família, por serem porto seguro.

A todos os professores que cruzaram meu caminho e deixaram contribuições inestimáveis, minha sincera gratidão. Em especial, à professora Daniele Lima, que, sendo minha professora de redação no ensino médio, tornou-se grande amiga e confidente durante a escrita deste trabalho; ao professor Raony Fontes, pelas discussões enriquecedoras sobre inteligência artificial e cálculo numérico; ao professor Daniel Diniz, pelas conversas, conselhos e aulas de otimização; e ao professor Adonias Magdiel, pelas aulas inspiradoras de estatística.

Aos meus orientadores, professores Márcio Martins e Rodrigo Meira, meu agradecimento especial. Ao professor Márcio, pela valiosa orientação, amizade e pelas ricas discussões sobre otimização e controle, conduzindo-me, como em um controle preditivo, ao "set-point" e garantindo otimalidade e convergência na minha formação como pesquisador. Ao professor Rodrigo, por ter despertado, desde a graduação, meu encantamento pela teoria de controle e suas aplicações, pela orientação generosa, pelos conselhos e pelo apoio nos momentos mais difíceis, incentivando-me a encontrar novos caminhos.

Agradeço ainda aos membros da banca examinadora — professores Raony Fontes, Heleno Bispo e Arioston Morais — pelas contribuições e ideias que tornaram esta dissertação mais sólida e consistente.

Aos amigos, em ordem alfabética – Allan, Fábio, Gabriel, Guilherme, Igor, Maria, Melissa, Odilon, Rafael, Sérgio, Silas e Vinícius –, meu muito obrigado pela amizade, apoio e companheirismo.

Reconheço e agradeço à CAPES pelo apoio financeiro da bolsa de mestrado; à FAPESB pela assistência à pesquisa no âmbito do INCITERE, termo de concessão/convênio – PIE 0008/2022; e à AVEVA pela disponibilização da licença de software que viabilizou parte deste trabalho.

"Porque eu sou do tamanho do que vejo
E não do tamanho da minha altura..."

Fernando Pessoa

"I don't believe in talent, I believe in hard work."

Ray Allen

Abstract of Dissertation presented to PEI/UFBA as a partial fulfillment of the requirements for the degree of Master of Science (M.Sc.)

Electricity generation still relies largely on fossil fuels; however, growing concerns about climate change, resource depletion, and increasing energy demand have accelerated the transition to cleaner alternatives. Renewable Energy Resources (RERs) offer advantages such as abundance, diversity, and low carbon dioxide emissions, but their intermittency and variability demand effective integration strategies. In this scenario, microgrids emerge as a promising solution by integrating generation, storage, and loads into modular systems capable of operating either grid-connected or in islanded mode. To ensure efficient and reliable performance, it is essential to adopt advanced control and optimization strategies, particularly in managing power exchange with economic objectives – an operational layer known as the Energy Management System (EMS). In this context, this work proposes Model Predictive Control (MPC) strategies for EMSs focused on economic operation, including: (i) the development of a two-layer MPC based on Quadratic Programming (QP), whose results demonstrated improvements in numerical robustness, reduced computational costs, and faster optimization problem resolution compared to traditional Nonlinear Programming (NLP)-based MPC approaches; (ii) the application of the QP-based MPC strategy to an industrial-scale microgrid, together with the introduction of Artificial Neural Networks (ANNs) for disturbance modeling, such as renewable generation and demand, incorporating these forecasts into the control framework, with results showing greater robustness in decision-making under the operational variability imposed by disturbances; and (iii) the proposal of a single-layer, zone-based MPC strategy designed to operate within economically viable control regions defined by the microgrid operator, with a closed-loop stability proof based on Lyapunov theory, whose simulation analysis demonstrated that the cost function behaves as a Lyapunov function, ensuring controller scalability, recursive feasibility, and nominal convergence.

Keywords. Microgrid, EMS, Economic MPC, Zone-MPC

Contents

List of Figures

List of Tables

Nomenclature & Greek Symbols

$\mathbf{A}$ – state matrix

$\mathbf{B}$ – input matrix

$\mathbf{C}$ – output matrix

δ – binary variable

$\Delta\mathbf{u}(k+j|k)$ – movement increment in the input variables at time step k

$\mathbf{D}_d$ – power balance disturbance matrix

$\mathbf{D}_u$ – power balance input matrix

$\mathbf{d}(k)$ – disturbance vector

$\mathbf{d}(k+1)$ – disturbance vector at time step $k+1$

$\mathbf{d}(k-n)$ – disturbance vector at time step $k-n$

ℓ_{eco} – economic function

L – number of hidden layers in LSTM

M – number of neurons in each hidden layer in LSTM

n_u – number of inputs of the centralized system

n_x – number of states of the centralized system

n_y – number of outputs of the centralized system

N – MPC control horizon

$\mathbf{Q}$ – weighting matrix of the output variables

$\mathbf{Q}_u$ – weighting matrix of the manipulated variables

$\mathbf{Q}_x$ – weighting matrix of the state variables

$\mathbf{R}$ – weighting matrix of the manipulated increments or suppression matrix

Θ – parameter containing the value of the corresponding synaptic weights and bias

$\tilde{\mathbf{u}}_{k+1}$ – inherited input sequence at $k+1$

$\tilde{\mathbf{x}}_{sp,k}$ – inherited reference state vector at $k+1$

$\tilde{\mathbf{y}}_{sp,k+1}$ – inherited output set-point at $k+1$

$\mathbf{u}(k+j|k)$ – input vector at time step $k+j$

$\mathbf{u}_{\max}$ – upper bounds of input variables

$\mathbf{u}_{\min}$ – lower bounds of input variables

$\mathbf{u}_t$ – input targets

$\mathbf{u}_k^*$ – optimal control sequence at time step k

V_k – cost function of controller at time step k

$\mathbf{x}(k)$ – state vector at time step k

$\mathbf{x}(k+N)$ – predicted state vector at the terminal step

$\mathbf{x}_{sp,k}^*$ – reference state vector at time step k

$\mathbf{x}(k+1)$ – measured process output

$\mathbf{y}(k)$ – output vector at time step k

$\mathbf{y}(k+N)$ – predicted output at the terminal step

$\mathbf{y}_{\max}$ – upper bounds of output variables

$\mathbf{y}_{\min}$ – lower bounds of output variables

$\mathbf{y}_{sp}$ – vector of output set-points

$\mathbf{y}_{sp,k}^*$ – optimal output set-point at time step k

Acronyms

EMS – Energy Management System

EMPC – Economic Model Predictive Control

ESS – Energy Storage Systems

LHMPC – Lyapunov Hybrid Model Predictive Control

LSTM – Long Short Term Memory

MLD – Mixed Logical Dynamical

MILP – Mixed-Integer Linear Programming

MIQP – Mixed-Integer Quadratic Programming

MPC – Model Predictive Control

NLP – Nonlinear Programming

QP – Quadratic Programming

RTO – Real-Time Optimization

RNN – Recurrent Neural Network

SHL – Storage Hydrogen Level

SOC – State of Charge

SOE – State of Energy

SSMPC – Stochastic Model Predictive Control

Chapter 1

Introduction and literature review

1.1 Electrical power system

Although often perceived as a readily available commodity, electric energy relies on a complex and highly integrated infrastructure composed of three main stages: generation, transmission, and distribution (Singh 2008). The process begins with the conversion of primary energy sources – such as hydro, thermal, wind, and solar – into electrical power. This power is then transmitted over long distances via high-voltage transmission lines designed to minimize energy losses. In the final stage, distribution systems reduce the voltage levels to medium and low ranges, delivering electricity to end users, including residential, commercial, and industrial consumers. This hierarchical structure ensures the reliable and continuous supply of electric energy throughout society.

Notwithstanding the robustness of the electricity infrastructure, the global electricity mix remains heavily reliant on fossil fuel-based sources, a dependency further exacerbated by population growth and the resulting increase in energy demand (York 2016). However, the progressive depletion of these resources, combined with the pressing need to reduce carbon dioxide (CO_2) emissions, has prompted numerous governmental initiatives to promote the adoption of Renewable Energy Resources (RERs) (Jordan-Korte 2011). These efforts are driving an energy transition that seeks not only to enhance efficiency but also to ensure accessibility and long-term sustainability.

To support the expansion of electricity generation from Renewable Energy Resources (RERs), the Paris Agreement was established under the United Nations Framework Convention on Climate Change (Agreement 2015). Since then, multiple

organizations have released annual reports tracking the evolution of the global electricity sector. A recent example is the Global Electricity Review, published in April 2025 based on 2024 data (Graham et al. 2025), which indicates that the growth of wind and solar generation has enabled renewables to account for nearly 30% of total global electricity production for the first time – driven primarily by countries such as China, Brazil, and the Netherlands. In Brazil, wind and solar sources contributed 21% of total generation, positioning the country as a global leader in these technologies and the second cleanest energy producer among G20 nations, as shown in Table 1.1. This context underscores both global and national progress in the integration of renewable energy into the electricity mix.

Table 1.1: Global and Brazilian Electricity Matrix.

Energy Source	Global Structure /(%)	Brazilian Structure /(%)
Oil and derivatives	35.00	1.00
Natural gas	23.00	6.00
Nuclear	9.10	2.00
Other non-renewables	2.70	3.00
Non-renewable	**69.80**	**12.00**
Solar	5.50	5.00
Wind	7.80	16.00
Hydroelectric	14.20	61.00
Biomass	2.40	5.00
Other renewables	0.30	1.00
Renewable	**30.20**	**88.00**

While renewable energy generation has experienced substantial global growth, fossil fuels – including coal, oil, and natural gas—still dominate the global energy landscape. Brazil represents a notable deviation from this pattern, with hydropower accounting for the majority of its electricity generation, followed by wind, natural gas, and solar power, while coal and oil play only marginal roles in the national power generation mix, as shown in Table 1.1.

The Net Zero by 2050 report from the International Energy Agency (IEA) ou-

tlines an ambitious roadmap for decarbonizing the power sector, emphasizing the need for a fundamental transformation of existing energy systems (Bouckaert et al. 2021). The current grid architecture – characterized by centralized generation from both fossil fuel-based plants (e.g., coal-fired and natural gas combined-cycle facilities) and large-scale renewable installations such as hydroelectric dams – combined with predominantly unidirectional transmission networks, reveals critical structural vulnerabilities. These systems face dual exposure: fossil-based plants are subject to fuel supply disruptions and operational failures, while hydroelectric generation is increasingly affected by climate-induced droughts. These weaknesses underscore the urgency of transitioning toward more resilient and adaptive power system architectures.

In this context, distributed generation has emerged as a key strategy to address these challenges, providing a means to reduce dependence on centralized fossil-based power plants while simultaneously enhancing system resilience (Ackermann et al. 2001). This paradigm shift redefines the role of consumers, transforming them into active prosumers who contribute to the grid through bidirectional energy flows, thereby reshaping operational dynamics and enabling new market structures (Gautier et al. 2018).

The integration of renewable energy sources – such as solar and wind – within this distributed framework presents both significant opportunities and technical challenges. While these resources offer abundant and sustainable energy potential on a global scale, their inherent intermittency and variability demand innovative solutions for effective grid integration. Unlike dispatchable fossil-based generation, which can be adjusted to meet real-time demand, renewable output is subject to environmental fluctuations, requiring advanced infrastructure and operational strategies (Erdiwansyah et al. 2021). Addressing this variability through smart grid technologies, demand response mechanisms, and energy storage systems is essential to maintaining grid stability while maximizing renewable energy penetration (Das et al. 2014).

This evolution has led to the emergence of the smart grid, a transformative advancement over the traditional electrical grid. Unlike the conventional unidirectional, centralized model – where large-scale generation dominates and the roles of

production and consumption are strictly separated—the smart grid operates as a decentralized, bidirectional system, enabling energy and information to flow dynamically between users, distributors, and system operators. This capability transforms consumers into "prosumers" (producers + consumers), fosters the integration of renewable energy, and allows for greater system optimization and flexibility. In this new framework, users transition from passive consumers to active participants in energy generation, particularly through renewable sources and small-scale distributed systems (Bayindir et al. 2016).

The smart grid comprises intelligent, interconnected nodes capable of autonomous operation, real-time communication, and dynamic energy exchange, thereby enhancing reliability, resilience, and distribution efficiency (Fang et al. 2011, Gungor et al. 2011). This paradigm shift moves beyond the traditional one-way power flow of conventional grids, integrating bidirectional energy flows and advanced monitoring systems (Akyildiz et al. 2005). Such capabilities enable improved integration of distributed energy resources (DERs), demand response programs, and predictive maintenance strategies (Liu et al. 2012).

However, the heterogeneous and decentralized architecture of the smart grid introduces significant technical challenges, including interoperability between diverse devices and protocols, cybersecurity threats, real-time control under variable operating conditions, and the need for scalable communication infrastructures (Yan et al. 2013, Mohsenian-Rad et al. 2010). Addressing these challenges requires advanced solutions in system design, control algorithms, and implementation frameworks—such as model predictive control (MPC) for optimal energy management (Ma et al. 2014), robust communication protocols for cyber-physical integration (Galli et al. 2011), and standardized architectures to ensure interoperability (IEEE Standards Association 2011).

A key element within this infrastructure is the microgrid, illustrated in Figure 1.1. Microgrids are self-contained, locally managed energy networks that integrate electrical loads, distributed generation sources – often renewable – and energy storage systems. They can operate either in grid-connected mode or autonomously (islanded), depending on system conditions and operational objectives. Scalable to diverse environments – such as hospitals, university campuses, industrial facilities,

and residential neighborhoods – microgrids facilitate the integration of Renewable Energy Resources (RERs) by mitigating variability through localized storage and adaptive control strategies (Lasseter 2001).

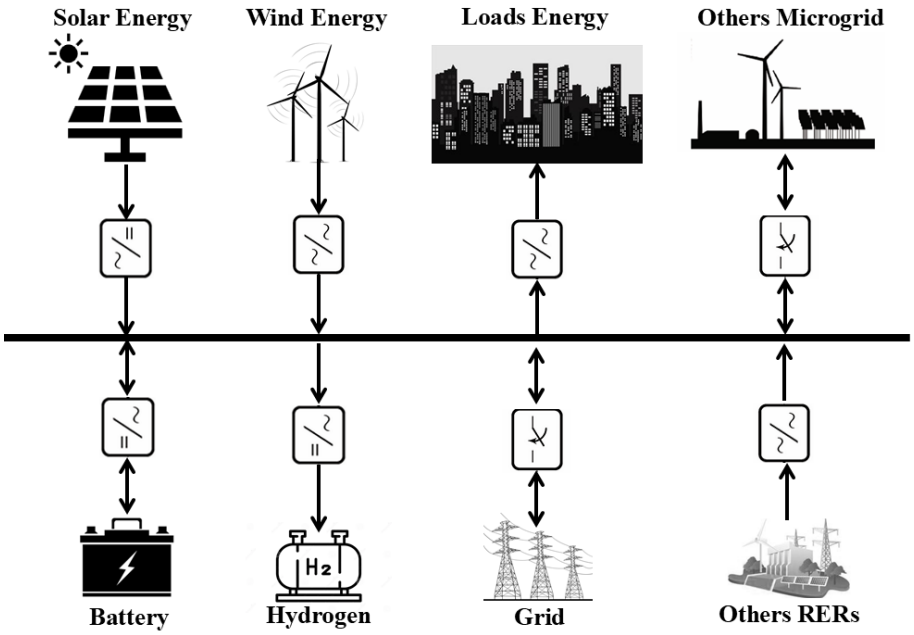

Figure 1.1: Microgrid: systems and control.

For proper microgrid operation, the control system can achieve multiple objectives categorized into three levels (Figure 1.2) (Bordons et al. 2020).

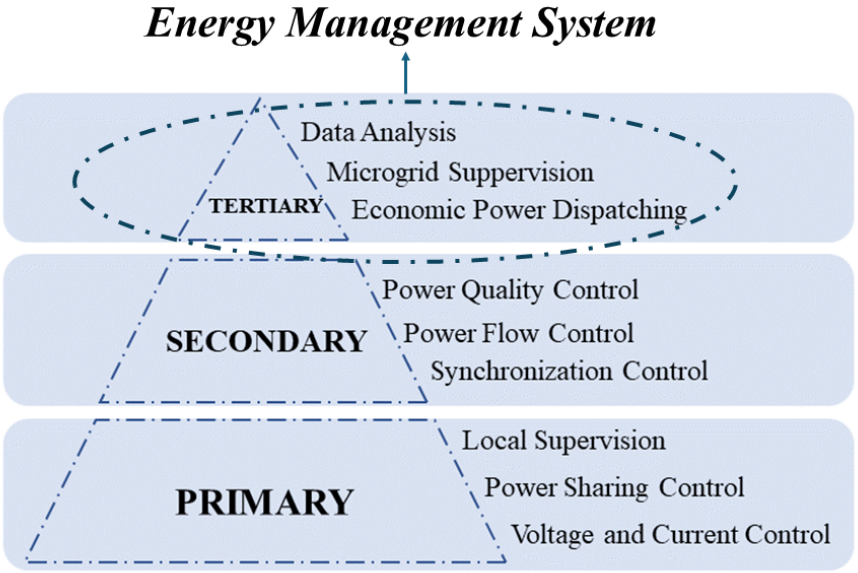

Figure 1.2: Hierarchical structure for microgrid control.

- The primary level is operated on a time scale of seconds and aims to maintain voltage and frequency stability during changes in generation and demand and after safety for islanding mode.

- The secondary level is operated on a time scale of minutes and is responsible for ensuring that voltage and frequency deviations are stabilized after a change in load or generation, and for eliminating any variations induced by the primary level.

- The tertiary level, also known as Energy Management System (EMS), is operated on a time scale of hours or months, as it is responsible for controlling the flow of energy between the microgrid and the main grid or between other microgrids based on the energy purchase and sale schedule for the grid in connected mode or autonomous mode in islanding mode.

Given the complexity and strategic importance of the tertiary control level – embodied by the Energy Management System (EMS) – in the efficient operation of microgrids, this dissertation aims to advance energy management at this level through the development of control strategies that incorporate economic, operational, and regulatory perspectives. The EMS plays a pivotal role in optimizing power flow under both grid-connected and islanded operating modes and is fundamental for managing energy purchase and sale schedules over extended time horizons, ranging from hours to months.

1.2 Model Predictive Control for Energy Management System

Given that this hierarchical control structure parallels those commonly found in the process industry, many advanced control techniques originally developed in that domain have been adapted to address the challenges of Energy Management Systems (EMS) in microgrids (Bordons et al. 2020), as illustrated in Figure 1.3. The primary objective of advanced control is to operate the system as close as possible to economically optimal conditions while ensuring stability and convergence (Mayne

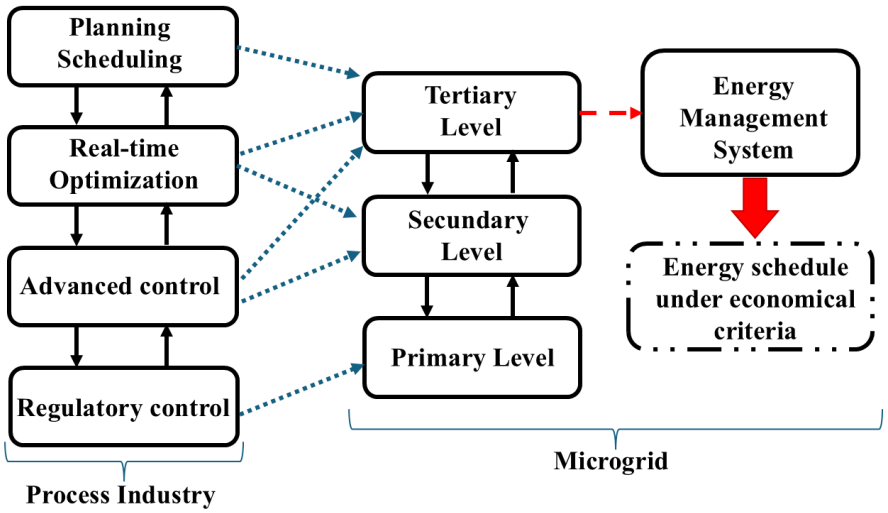

Figure 1.3: Comparison between the control hierarchy of a process industry and the hierarchy of a microgrid.

et al. 2000, Engell 2007). This is typically achieved through a hierarchical architecture: at the upper layer, a scheduler and economic planner defines what, when, and how much the system should produce, based on market signals and internal plant constraints (Tatjewski 2008). This layer is conventionally executed via Real-Time Optimization (RTO), which performs static optimization in real time, providing economically optimal setpoints to the control layer. The advanced control layer, typically implemented through Model Predictive Control (MPC), is responsible for computing the optimal control actions required to drive the system toward the desired operating points, while ensuring compliance with operational constraints and optimizing dynamic performance (Ying & Joseph 1999).

However, in many practical cases, the setpoints provided by the RTO layer may be infeasible due to system constraints. One proposed solution is to introduce an intermediate coordination layer between RTO and MPC, referred to as the Steady-State Target Optimizer (SSTO) (Muske 1997). The SSTO recalculates admissible steady-state targets that respect operational constraints, thereby enabling a smooth transition between the economic objectives of RTO and the dynamic regulation performed by MPC. This integrated architecture enhances both system stability and closed-loop performance, while preserving economic efficiency.

Nevertheless, in many operational scenarios, the most economically favorable operating conditions occur during transient behavior rather than at steady state,

particularly in systems subject to fast-changing economic parameters, where transient operation enables the exploitation of short-term market opportunities. In other cases, such as industrial processes with time-sensitive constraints, transient optimization can reduce startup or shutdown costs and leverage temporary efficiency gains that cannot be achieved through steady-state operation. To address these limitations, several alternative approaches have been proposed, including: (I) the Dynamic Real-Time Optimizer (D-RTO), which formulates and solves a dynamic optimization problem to generate optimal reference trajectories for the MPC, resulting in a D-RTO+MPC architecture (Kadam & Marquardt 2007*a*, Biegler 2009); (II) the Integrated RTO+MPC scheme, where the economic objective of the RTO is embedded directly into the MPC cost function, creating a unified optimization framework that accounts for both regulation and economic performance (Zanin et al. 2002, Adetola & Guay 2010); and (III) the Economic Model Predictive Control (EMPC) approach, which merges economic and control objectives into a single optimization problem, with control actions applied directly to the plant, eliminating the need for a separate RTO layer and enabling economic optimization in closed-loop operation (Rawlings et al. 2012).

Among the three advanced control strategies, RTO+MPC emerges as an intermediate solution that aims to reconcile computational tractability and economic performance by embedding part of the economic objective directly into the MPC cost function. This configuration enables a balanced trade-off between optimization and computational effort, although its decoupled nature may result in suboptimal performance when there is strong interdependence between economic objectives and dynamic constraints (De Souza et al. 2010). In contrast, D-RTO+MPC solves a complete dynamic optimization problem to generate reference trajectories for the MPC, offering high fidelity in economic optimization during transient regimes and proving particularly advantageous in scenarios with rapid operational variations. However, this approach requires greater computational capacity, demanding robust numerical solvers and high-performance processing infrastructure to enable its real-time application (Kadam & Marquardt 2007*b*). Finally, Economic Model Predictive Control (EMPC) integrates economic and control objectives within a single optimization layer, allowing the direct implementation of economically optimal control

actions. Although it represents the highest level of integration between economics and dynamics, EMPC poses greater challenges for obtaining formal stability guarantees and depends heavily on the accuracy of the economic model employed (Angeli et al. 2012).

In this context, the application of Model Predictive Control (MPC) in microgrids proves particularly advantageous, given its conceptual alignment with the hierarchical control architectures widely adopted in industrial systems, where this approach is already well established. Advanced strategies, such as Economic Model Predictive Control (EMPC), further extend these capabilities by directly incorporating economic metrics — including generation costs, energy market transactions, and asset degradation — into the control structure, thereby ensuring optimal financial performance even under transient conditions (Bordons et al. 2020, Hu et al. 2023, Zheng et al. 2017). This convergence of dynamic adaptability, operational robustness, and economic optimization establishes MPC as a central approach for microgrid energy management, enabling resilient and economically efficient operation in both grid-connected and islanded modes.

Some MPC-based strategies have been proposed for economic energy management in microgrids. Bordons Alba et al. (2015) developed an EMPC based on Mixed-Integer Quadratic Programming (MIQP), while Zhang et al. (2015) proposed a Mixed-Integer Linear Programming (MILP) formulation, both combining economic planning and control within a single optimization layer. However, they lack formal guarantees of recursive feasibility and closed-loop stability. The MIQP approach, although more accurate, exhibits high computational complexity and a risk of infeasibility under abrupt operational changes, whereas the MILP reduces complexity through linearizations but at the expense of fidelity, potentially compromising economic optimality. Both were validated only through simulations or in laboratory-scale microgrids, limiting their demonstration in larger real-world systems.

Other works adopt hierarchical control architectures. Pereira et al. (2015) applied a D-RTO+MPC framework to periodic systems (Limon et al. 2014), incorporating terminal constraints to ensure feasibility and closed-loop convergence. To avoid formulating a mixed-integer programming problem, the authors used smooth approximations of the sign function, converting it into a Nonlinear Programming (NLP)

problem, without, however, assessing whether this simplification affects feasibility and closed-loop stability. In turn, Petrollese et al. (2016) proposed a two-layer MPC structure based on Mixed-Integer Linear Programming (MILP), in which the upper layer performs energy planning and the lower layer executes real-time control, achieving good performance in resource coordination but without providing formal guarantees of stability or recursive feasibility.

Focusing on stability, Pereira et al. (2017) proposed a robust RTO+MPC architecture based on Quadratic Programming (QP), which avoids nonlinear constraints and provides formal proofs of recursive feasibility and closed-loop stability. Complementarily, Olama et al. (2018) introduced a Lyapunov-based hybrid MPC (LHMPC), ensuring stability through the use of ellipsoidal terminal sets and decay conditions embedded in the control formulation.

Regulatory constraints were addressed by Conte et al. (2020), who employed a Mixed Logical Dynamical (MLD) formulation within a two-layer MPC structure tailored to the Brazilian energy market. However, the study lacks formal proofs of convergence and stability.

More recently, Alarcón et al. (2022) implemented an EMPC with variable economic criteria under the RTO+MPC framework, incorporating constraints to promote convergence and stability, although relying on NLP due to complementarity conditions. Follow-up studies introduced stochastic formulations (Alarcón et al. 2023) and deep-learning-based forecasting (Alarcón et al. 2024), enhancing predictive capability but still facing computational challenges for large-scale deployment.

Although offering a more realistic representation of the system — accurately capturing equipment nonlinearities, complex operational constraints, and interdependencies among variables — Nonlinear Programming (NLP), which predominates in economic microgrid management approaches, poses significant challenges such as high computational cost, sensitivity to initial conditions, and difficulty in ensuring global optimality. These limitations become particularly critical in predictive control applications, where real-time operation demands algorithms that are both computationally efficient and robust.

Moreover, a notable gap exists regarding theoretical guarantees. Among the reviewed works, only Pereira et al. (2017) and Olama et al. (2018) provide formal

proofs of closed-loop stability. In addition, Alarcón et al. (2024) is the only study that explicitly integrates disturbance modeling into the control formulation, offering a more comprehensive predictive framework.

To overcome the limitations identified in the literature, this work proposes two control laws: a hierarchical two-layer architecture based on quadratic programming, designed to ensure computational efficiency for real-time operation; and an integrated single-layer formulation that unifies optimization and control, supported by formal mathematical proofs that guarantee closed-loop stability.

Both strategies aim primarily to mitigate the high computational cost commonly associated with model predictive control methods based on nonlinear programming, while also incorporating artificial neural networks for disturbance forecasting.

In the single-layer scheme, these networks are embedded directly into the controller, enabling data-driven disturbance handling while preserving computational feasibility for real-time microgrid operation. This unified formulation stands out for offering formal stability guarantees – an aspect often overlooked in the literature – and for integrating a robust, learning-based disturbance rejection mechanism.

1.3 Objective

1.3.1 Main objective

Propose Model Predictive Control (MPC) strategies based on Quadratic Programming (QP) for an Energy Management System (EMS) in microgrids, with the objective of reducing the high computational cost associated with MPC approaches based on Nonlinear Programming (NLP), by incorporating artificial intelligence for disturbance modeling.

1.3.2 Specific objective

I. Develop Quadratic Programming (QP)-based controllers using two-layer and single-layer architectures for microgrids, ensuring computational efficiency and real-time feasibility.

II. Compare the performance of the proposed two-layer controller with Nonlinear

Programming (NLP)-based approaches, highlighting improvements in stability, response time, and adaptability.

III. Formally prove the closed-loop stability of the single-layer controller through a Lyapunov-based analysis.

IV. Integrate artificial neural networks into the controller for disturbance and uncertainty modeling and prediction (e.g., renewable generation variability, operational failures).

V. Validate performance in scenarios including microgrids with multiple renewable sources, energy storage systems, and grid interconnections.

1.4 Structure of the work

This work is organized into six chapters, including this introductory one. Each chapter focuses on a specific contribution of the master's thesis. A summary of the content of each chapter is presented below.

Chapter 2 addresses the modeling of a microgrid, including the mathematical representation of its main components and equipment. This modeling serves as the foundation for the control strategies and simulations developed in the following chapters.

Chapter 3 presents the development of a two-layer model predictive control (MPC) strategy applied to the energy management system of a microgrid. Starting from a nonlinear programming (NLP)-based MPC formulation commonly found in the literature, the model is reformulated into a quadratic programming (QP)-based MPC structure. Additionally, a microgrid plant is implemented in the AVEVA Process Simulation environment, serving as a reference system to compare the performance of both approaches as model-plant mismatch increases over time.

Chapter 4 presents the application of the proposed QP-based MPC framework to an industrial microgrid case study. In this context, external disturbances are modeled using artificial neural networks, with the aim of enhancing the predictive capability and robustness of the controller under operational uncertainties.

Chapter 5 proposes a new economic model predictive control strategy based

on quadratic programming. The stabilizing properties of the proposed method are demonstrated through an approach that incorporates a terminal equality constraint, combining an artificial equilibrium point with slack variables in coupled constraints to ensure recursive feasibility and closed-loop stability.

Finally, Chapter 6 summarizes the main contributions of this thesis and provides suggestions for future research.

1.5 Publications

The following publications resulted from the development of this thesis, and are presented in chronological order:

- CALHAU, F. A. S.; MEIRA, R. L.; BISPO, H.; MARTINS, M. A. F. A two-layer MPC strategy for microgrid energy management within a software-in-the-loop scheme with AVEVA Process Simulation. *XVII Simpósio Brasileiro de Automação Inteligente*. São João del Rei: 2025.

- CALHAU, F. A. S.; SANTOS, P. R. J.; MEIRA, R. L.; MARTINS, M. A. F. An MPC-based energy management system embedding neral networks for forecasting renewable energy generation and demand: a study on green hydrogen production. *Congresso Brasileiro de Engenharia Química*. Belo Horizonte: 2025.

1.5.1 Works in the submission process

- CALHAU, F. A. S.; SANTOS, P. R. J; BISPO, H.; MEIRA, R. L.; MARTINS, M. A. F. Single-layer zone-based MPC for energy management systems embedding artificial neural network for forecasting renewable energy generation and demand.

Chapter 2

Model description

This chapter presents the formulation of a mathematical model for microgrid energy management, encompassing the representation of storage systems, renewable energy sources, and load demand. It also introduces the application of artificial intelligence techniques to model generation and consumption profiles based on data provided by monitoring agencies. Finally, a discrete-time linear state-space model is developed to serve as the foundation for predictive control design in microgrid operation

2.1 Introduction

A microgrid is defined as an autonomous electrical system that integrates multiple types of energy generation units – based on either renewable or non-renewable sources – along with energy storage systems and electrical loads associated with specific demand profiles. These systems are distinguished by their capability to operate independently in islanded mode or remain connected to the main power grid (Lasseter 2001).

Figure 2.1 illustrates the general architecture of a microgrid, composed of renewable energy sources (solar and wind), energy storage systems (battery), grid interconnections, consumer loads, and a hydrogen-based consumption plant. A microgrid may operate in isolation, remain connected to the main grid, or be interconnected with another microgrid through a Point of Common Coupling (PCC). The vertical bar in the diagram represents the busbar – the central node of the microgrid – where power exchange takes place. To ensure system stability, the power balance at this node must be maintained at all times (Alarcón 2024).

To develop a mathematical model that accurately represents the microgrid, it is

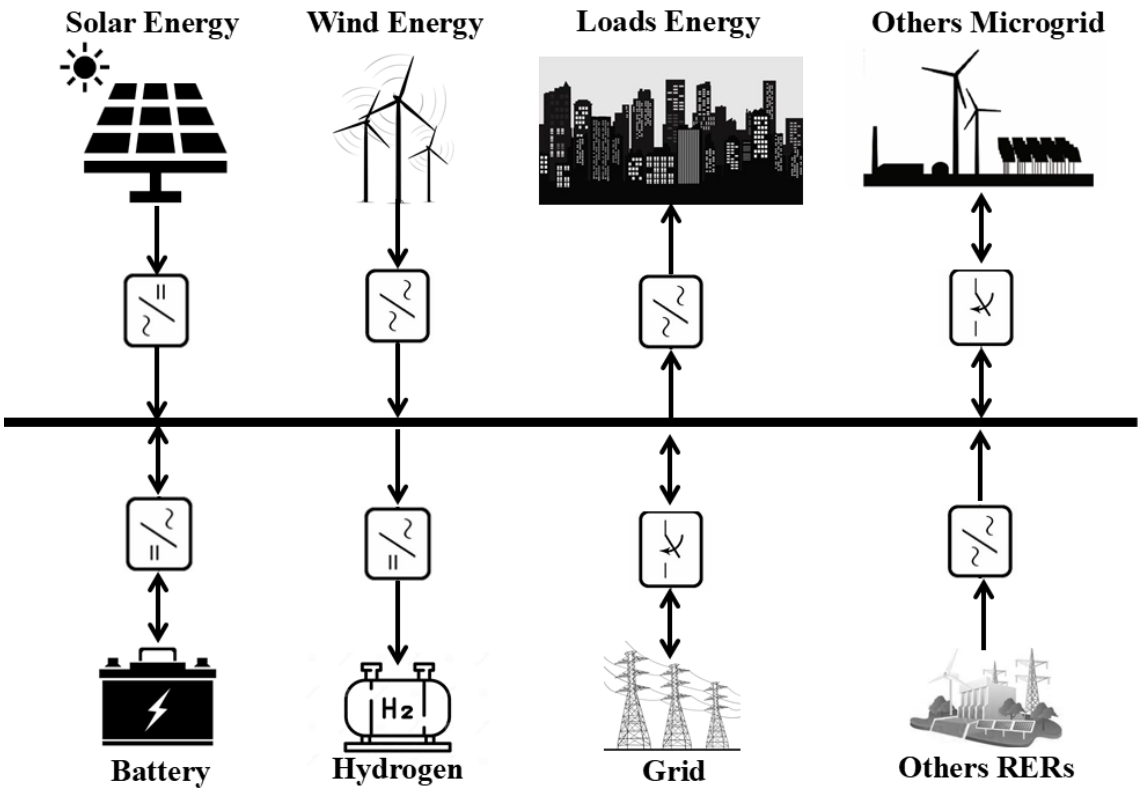

Figure 2.1: General Architecture of a Microgrid.

first necessary to define the consumption profile to which the system is connected, as well as the mathematical representations of the storage system and renewable energy sources. In this study, the storage system includes batteries, a supercapacitor, and an electrolyzer, while solar and wind generation are adopted as the renewable energy inputs. These components are integrated into a unified model designed to capture the dynamic interactions between generation, storage, and consumption, with the objective of optimizing performance and ensuring the operational stability of the microgrid.

2.2 Energy storage systems

Energy storage systems (ESS) are critical elements in microgrids, playing a key role in mitigating the intermittency and variability inherent to renewable energy sources (Bordons et al. 2020). Among the most widely adopted technologies, electrochemical batteries remain the most prevalent and mature solution, followed by ultracapacitors, hydrogen-based systems – including electrolyzers and fuel cells –, flywheels,

and other emerging alternatives. Each of these technologies presents distinct advantages in terms of energy density, response time, and lifecycle, making them suitable for specific roles within microgrid architectures.

2.2.1 Batteries

A battery is an electrochemical device composed of one or more voltaic cells that stores electrical energy through reversible chemical reactions (Bordons et al. 2020). During discharge, the stored chemical energy is converted back into electrical energy with a certain efficiency. This charge–discharge cycle can be repeated a finite number of times, which defines the battery's lifespan (Kularatna & Gunawardane 2021).

Among the materials used in battery construction, lithium-ion technology is the most commonly employed in microgrids due to its superior energy density, efficiency, and performance under dynamic operating conditions – making it particularly suitable for systems subject to frequent disturbances, such as microgrids.

For the energy management model of a microgrid, it is essential to know the system's state of charge SOC. In the case of batteries, this state can be estimated using the Coulomb Counting Method, expressed as:

$$SOC(t) = SOC(0) \pm \frac{1}{C_{Ah}} \int i_{bat} dt, \tag{2.1}$$

where C_{Ah} is the storage capacity in Ah, i_{bat} is the current in A, where the positive sign refers to the charging process, while the negative sign of its discharge and the punch refer to the initial state or level of charge before producing its charge or discharge during a certain period of time.

However, since this study focuses on power exchange between microgrid components, the battery current can be replaced by the battery power P_{bat} as follows:

$$SOC(t) = SOC(0) \pm \frac{1}{C_{Wh}} \int P_{bat} dt, \tag{2.2}$$

where C_{Wh} is the storage capacity in kWh.

By differentiating the equation and incorporating battery efficiency, followed by discretization, it can be expressed as:

$$SOC(k+1) = SOC(k) \pm \frac{\eta_{bat}}{C_{bat}} P_{bat}(k), \tag{2.3}$$

where C_{bat} is the storage capacity in kWh, η_{bat} is the battery efficiency.

In many applications, it is common to use battery efficiency to obtain a more accurate estimate of the state of charge (SOC) over time. This is because the charging and discharging processes are not completely efficient, meaning that part of the energy is dissipated as heat or lost through electrochemical processes. In such cases, it is common to adopt distinct modeling strategies for the state-of-charge (SOC) equation in order to accurately capture these asymmetries (Bordons et al. 2020, Alarcón 2024).

$$SOC(k+1) = SOC(k) \pm \frac{T_s \eta_{bat}}{C_{bat}} P_{bat}(k), \tag{2.4}$$

$$SOC(k+1) = SOC(k) + \frac{T_s}{C_{bat}} \left(\eta_{bat,c} P_{bat,c}(k) - \frac{P_{bat,d}(k)}{\eta_{bat,d}} \right), \tag{2.5}$$

$$SOC(k+1) = SOC(k) + \frac{T_s}{C_{bat}} \left(\eta_{bat,c} P_{bat,c}(k)\delta(t) - \frac{(1-\delta(t))P_{bat}(k)}{\eta_{bat}} \right), \tag{2.6}$$

where $\eta_{bat,c}$ and $\eta_{bat,d}$ are the charge and discharge efficiency, respectively, and $P_{bat,c}$ and $P_{bat,d}$ are the charge and discharge battery power, δ is a binary variable, which takes value 1 for charging and 0 for discharge, and T_s is the sampling time in hours.

The three expressions used to model the SOC of a battery differ mainly in how they handle efficiencies during the charging and discharging processes. The equation (2.4) employs a single efficiency for both processes, resulting in a simpler model suitable for cases where losses are close to 1 allowing the use of an average efficiency. This simplification enables the formulation of linear or quadratic optimization problems. Equation (2.5), in contrast, distinguishes between charging and discharging efficiencies, allowing for a more accurate representation of battery behavior. However, to prevent simultaneous charging and discharging, this modeling approach requires the introduction of complementarity constraints, leading to nonlinear formulations. Finally, Equation (2.6) equation incorporates a binary indicator function that explicitly defines the battery's operating mode (charging or discharging), which results in a mixed-integer optimization problem. Therefore, the choice of the most appropriate modeling approach depends directly on the optimization and control technique to be employed, as well as the trade-off between model fidelity and computational complexity.

2.2.2 Supercapacitor

The structural configuration of supercapacitors, also known as ultracapacitors, is based on the same principle as conventional electrostatic capacitors, consisting of two conductive electrodes separated by a dielectric, which prevents the direct conduction of current. The main distinction lies in the use of highly porous materials – such as activated carbon, carbon aerogels, or graphene – as electrode materials, resulting in a significantly increased electrochemically active surface area. This enhancement in specific surface area enables efficient formation of the electric double layer (EDL), leading to high capacitance and greater energy density compared to traditional capacitors (Conway 2013, Kularatna & Gunawardane 2021). This architecture, combining large surface area and electrochemical storage mechanisms, makes supercapacitors particularly suitable for applications requiring high power density and long cycle life.

Supercapacitors can be formally classified into three main categories based on their energy storage mechanisms and the materials used in the electrodes (Chatterjee & Nandi 2021): (i) electric double-layer capacitors (EDLCs), which store energy through the electrostatic separation of charges at the electrode – electrolyte interface; (ii) pseudocapacitors, where energy is stored primarily via fast Faradaic reactions at the electrode surface; and (iii) hybrid capacitors, which combine the mechanisms of both EDLCs and pseudocapacitors, offering a synergistic balance between high energy density and rapid charge – discharge capabilities. This classification, frequently adopted in recent reviews on advanced energy materials, provides a robust analytical framework for the development of optimized electrochemical energy storage devices (Bhojane 2022).

As with conventional capacitors, the capacitance of supercapacitors is expressed in farads F, which represents the amount of electric charge stored per unit of voltage. Therefore, the nominal capacity for energy storage is directly proportional to the square of the maximum operating voltage. This value is determined by the characteristics of the dielectric material and the electrochemical properties of the system, including electrolyte stability and the electrode potential window.

$$C_{sc} = \frac{1}{2} C V_{sc}^2 \tag{2.7}$$

where C_{sc} is the nominal capacity to storage energy in Watts-second, C_{sc} is the capacitance in Farads F and V_{sc} is its nominal voltage in Volts V.

The Coulomb Counting Method, commonly used to determine the state of charge SOC in batteries, can also be applied to supercapacitor. However, unlike batteries, energy storage in supercapacitor involves no chemical conversion – only physical processes – allowing nearly full energy recovery. Losses are minimal and mainly due to the Joule effect from internal resistance. Therefore, the energy state, typically referred to as SOE (State of Energy), is modeled in discrete time as:

$$SOE(k+1) = SOE(k) \pm \frac{T_s \eta_{sc}}{C_{sc}} P_{sc}(k) \tag{2.8}$$

where P_{sc} is the supercapacitor power in kW, T_s sampling time in hours, and η_{sc} is the supercapacitor efficiency.

When comparing the operational characteristics of ultracapacitors and batteries, it is observed that the former exhibit significantly less degradation over time, unlike batteries, which undergo chemical wear due to charge and discharge cycles (Bhojane 2022). Moreover, ultracapacitors can withstand abrupt energy fluctuations without compromising their integrity, and they can safely operate even near their maximum and minimum charge limits (Chatterjee & Nandi 2021).

2.2.3 Hydrogen storage

Another type of energy storage that has been gaining prominence is hydrogen-based storage, which can be produced through water electrolysis. Due to the high purity of the process and its economic potential, this form of storage has been widely studied and integrated into microgrids, establishing itself as a strategic vector for industrial defossilization (Garcia et al. 2021). Sectors such as the chemical, petrochemical, and steel industries already use hydrogen on a large scale, for example, in the production of ammonia, methanol, and iron ore reduction. Therefore, monitoring the storage hydrogen level (SHL) being stored is of critical importance in this context.

$$SHL(k+1) = SHL(k) + \frac{P_{H_2}(k)\eta_{H_2}}{C_{H_2}}, \tag{2.9}$$

P_{H_2} is the hydrogen power in kW, η_{H_2} is the hydrogen efficiency is the C_{H_2} is the hydrogen capacity in kWh.

This simplified linear dynamic assumes that the electrolysis reaction is significantly faster than the system's sampling interval. In the present model, a discretization time of 1 hour was adopted, while the electrolysis dynamics occur on the order of seconds. Therefore, it is reasonable to approximate the process as an instantaneous conversion at each time step, which justifies the use of Equation (2.9) without the inclusion of additional dynamic terms. This simplification omits the detailed modeling of electrochemical behavior, whose accurate representation would require a more detailed dynamic model. This assumption is widely accepted in the microgrid modeling literature, particularly in studies focused on higher-level energy management rather than short-term electrochemical behavior.

2.3 Renewable Resources

In microgrid systems, renewable energy resources are often treated as disturbances due to the intermittent and uncontrollable nature of their generation. The most common sources considered in this context are photovoltaic solar and wind energy. These systems can be modeled primarily through two distinct approaches: analytical equations or historical data. The following sections will detail each of these methods.

For modeling via analytical equations, the case study adapted from Alarcón et al. (2022) was adopted, using solar irradiation and temperature data from the city of Avellaneda, located in Santa Fe Province, Argentina. Conversely, for the historical data-based approach, the municipality of Guanambi, in Bahia, Brazil, was selected. In Brazil, historical data are provided by specialized energy monitoring and management agencies — particularly the Electric Energy Trading Chamber (CCEE 2024) — which offer detailed information on power generation from plants and consumption profiles of Brazilian cities.

2.3.1 Solar Photovoltaic

Through photovoltaic solar panels, electrical energy is generated from solar radiation. This is, without a doubt, the most abundant and easily accessible renewable resource. The power generated by a photovoltaic panel can be obtained through a mathematical model using an equivalent open-circuit model proposed by Xiao et al.

(2004).

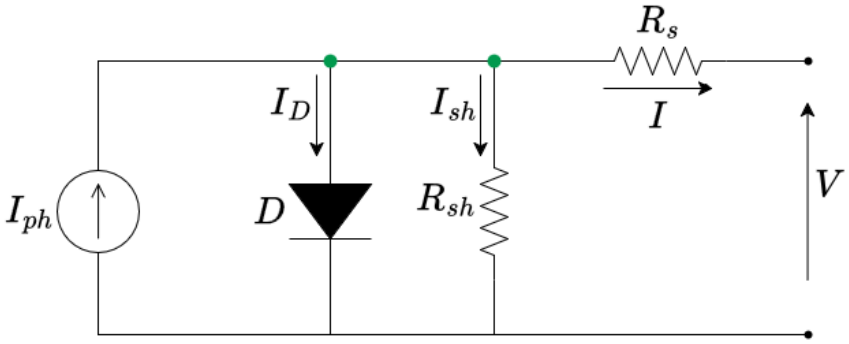

Figure 2.2: Equivalent electrical circuit to obtain a model of a solar cell.

The output electrical characteristics exhibit a nonlinear relationship between current and voltage, as well as between power and voltage. The equation describing the output current I as a function of the cell terminal voltage V is expressed as:

$$I = I_{ph} - I_s\left[e^{(\frac{q(V+iR_s)}{kT_cf})} - 1\right] - \frac{V + I_{rs}}{R_{sh}}, \tag{2.10}$$

where I_{ph} is the photovoltaic current, I_s is the diode saturation, q is the electron charge, k is the Boltzmann constant, T_c is the temperature of the cell, R_s is the series resistance, f is the ideality factor and R_{sh} is the parallel resistance.

The photovoltaic current I_{ph} depends on the solar irradiance G, expressed in W/m^2, and on the cell temperature T_c, indicated in °C, and is given by:

$$I_{ph} = \frac{G}{G_r}[I_r + \mu_{i_{sc}}(T_c - T_r)], \tag{2.11}$$

where G expressed in W/m^2 is the solar irradiance and on the cell temperature Tc indicated in C, $G_r = 1000$ W/m^2 is the value taken as a reference for irradiance, I_r is the current generated with reference values (generally it is considered equal to the I_{sc} short circuit current), $\mu_{i_{sc}}$ is the short circuit coefficient and $T_r = 25\ C$ is the reference temperature.

Finally, the saturation current I_s is determined by:

$$I_s = I_{sr}\left(\frac{T_c}{T_r}\right)^3 e\left(\frac{qE_g(\frac{1}{T_r} - \frac{1}{T_c})}{kf}\right), \tag{2.12}$$

where I_{sr} is the saturation current and E_g is the semiconductor energy in its band gap.

To obtain the generated power, the following expression is used:

$$P_{pv} = NV_{pv}I. \tag{2.13}$$

where N is the number of photovoltaic cells, V is the voltage in V.

Based on the presented equations, a photovoltaic panel simulation was conducted using data adapted from Alarcón et al. (2022), as well as solar radiation and temperature data from the city of Avellaneda, Santa Fe province, Argentina. The obtained results are shown in Figure 2.3.

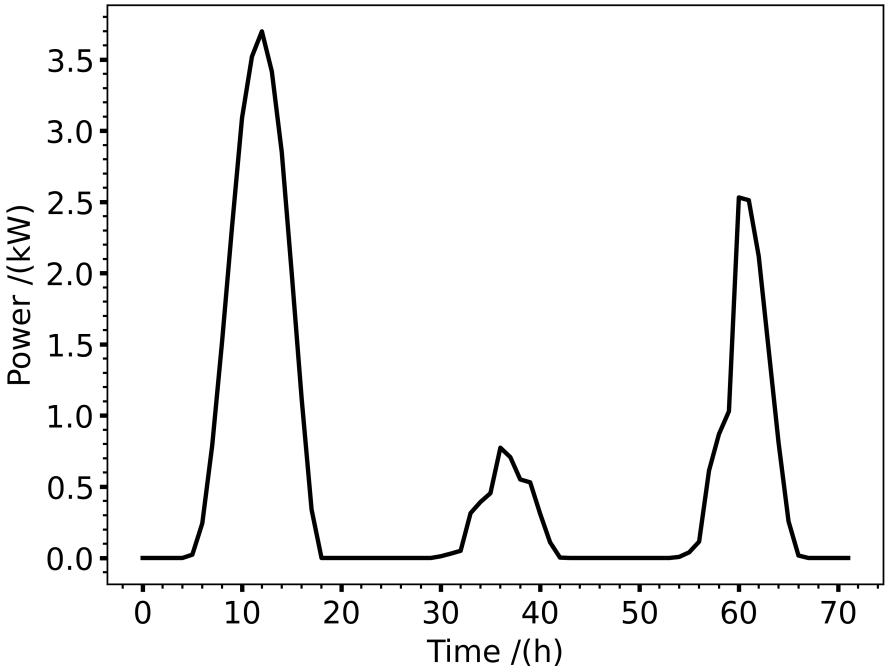

Figure 2.3: Power generated for 72 hours by photovoltaic solar panels of a residential microgrid. Adapted from Alarcón et al. (2022).

For the data-driven model, the solar generation profile of the city of Guanambi, located in the state of Bahia, Brazil, was used, as shown in Figure 2.4.

The analyzed time series reveals a typical seasonal pattern of photovoltaic systems, with generation peaks concentrated during midday hours, corresponding to the highest solar irradiance levels throughout the daily cycle.

This regularity in the generation pattern – although occasionally affected by weather variations – provides a robust foundation for applying artificial intelligence modeling techniques. The predictability of solar generation during daytime periods

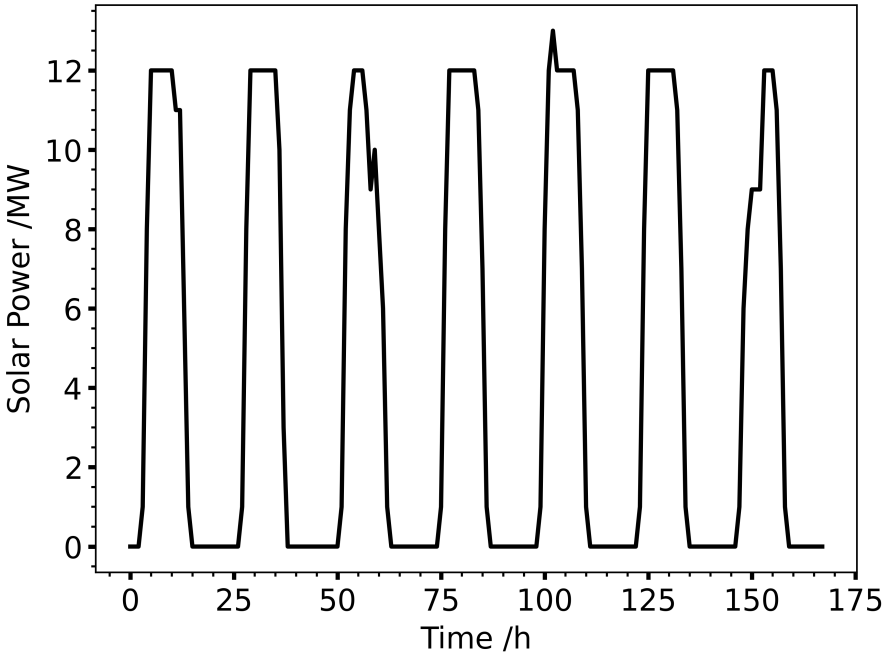

Figure 2.4: Historical data on solar power. Source: CCEE (2024).

is, therefore, a significant advantage in developing efficient forecasting models, which are essential for the economic and reliable operation of microgrids.

2.3.2 Wind energy

Another widely used renewable resource is wind energy, which employs wind turbines to harness the kinetic energy of the wind and convert it into electrical energy through a coupled generator. The electrical power generated by a wind turbine can be estimated using the following mathematical expression (Ackermann et al. 2001):

$$P_{\text{wind}} = \frac{1}{2}\rho A C_p(v) v^3 \tag{2.14}$$

where P_{wind} represents the power extracted from the wind (in watts), ρ is the air density (in kg/m^3), A is the swept area of the rotor blades (in m^2), $C_p(v)$ is the power coefficient, which depends on wind speed and turbine characteristics, and v is the wind speed (in m/s).

In the data-driven model, the historical wind energy generation profile for the city of Guanambi is depicted in Figure 2.5.

Unlike solar generation, which exhibits a well-defined daily pattern with peak output during daylight hours, wind power is inherently more irregular and influenced

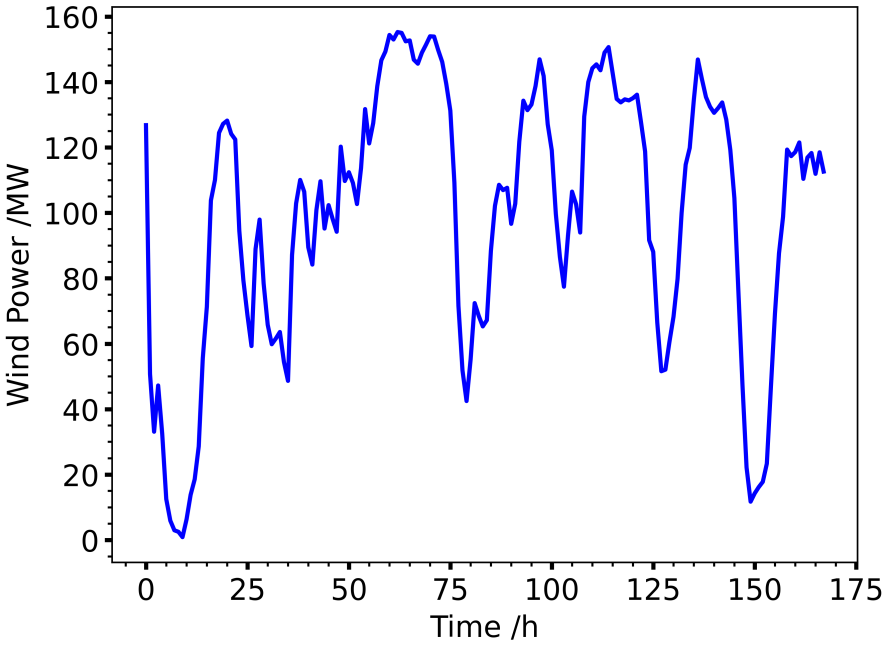

Figure 2.5: Historical data on wind power. Source: CCEE (2024).

by various atmospheric factors such as pressure, temperature, and local topography. The data reveals significant temporal variability, with fluctuations occurring on both hourly and seasonal timescales, reflecting the stochastic nature of wind behavior. In regions like Guanambi, wind speed tends to increase during nighttime and early morning hours, although this pattern may vary throughout the year. This inherent unpredictability poses challenges for modeling and forecasting, making it essential to employ machine learning-based prediction techniques to accurately capture wind dynamics and enhance integration with model predictive control strategies in microgrid applications.

2.4 Load Consumer

The development of a nominal demand profile can be carried out in two ways: (i) through estimates based on the installed nominal power and the usage hours of electrical equipment; or (ii) using actual energy consumption measurements obtained from instruments installed on the main distribution panel. Therefore, its modeling depends on the load estimate used at the site, expressed by:

$$P_{load} = V_{load} I_{load}, \tag{2.15}$$

where the P_{load} is the load power in W, V_{load} is the load voltage in V, and I_{load} is the load current and in A.

In the case of approach (i), for a residential-scale microgrid, the consumption profile was defined based on the average electricity usage of households in the province of Santa Fe, Argentina, providing a representative demand pattern for simulation and control purposes. Therefore, the obtained consumption profile is shown in Figure 2.6.

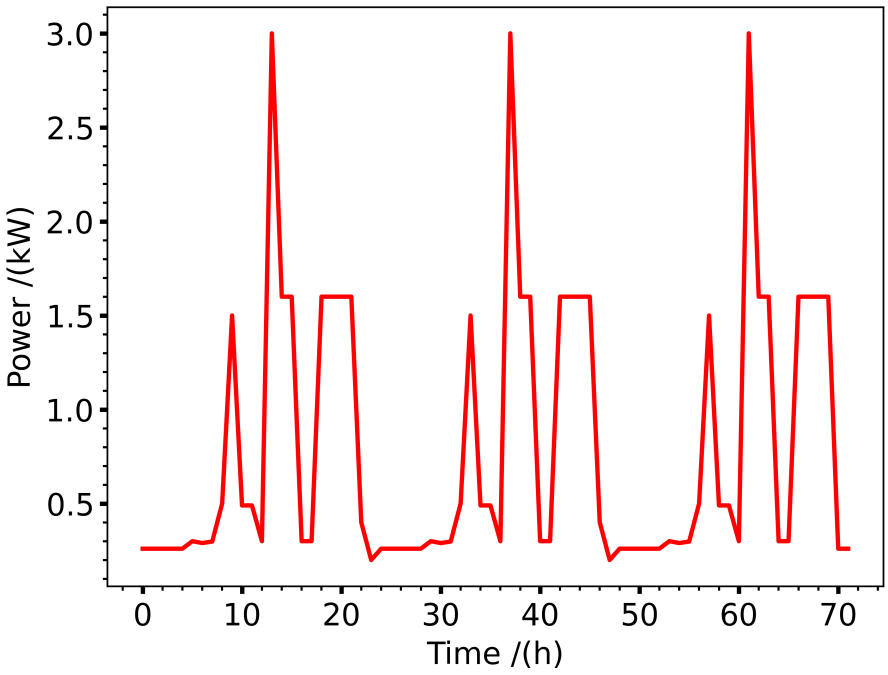

Figure 2.6: Daily energy consumption for a residential microgrid. Adapted from Alarcón et al. (2022).

This strategy assumes a fixed consumption pattern that repeats over time, without accounting for potential real-time variations that may occur. To overcome this limitation, model (ii) can be adopted, based on actual historical consumption data, as shown in Figure 2.7 for the city of Guanambi.

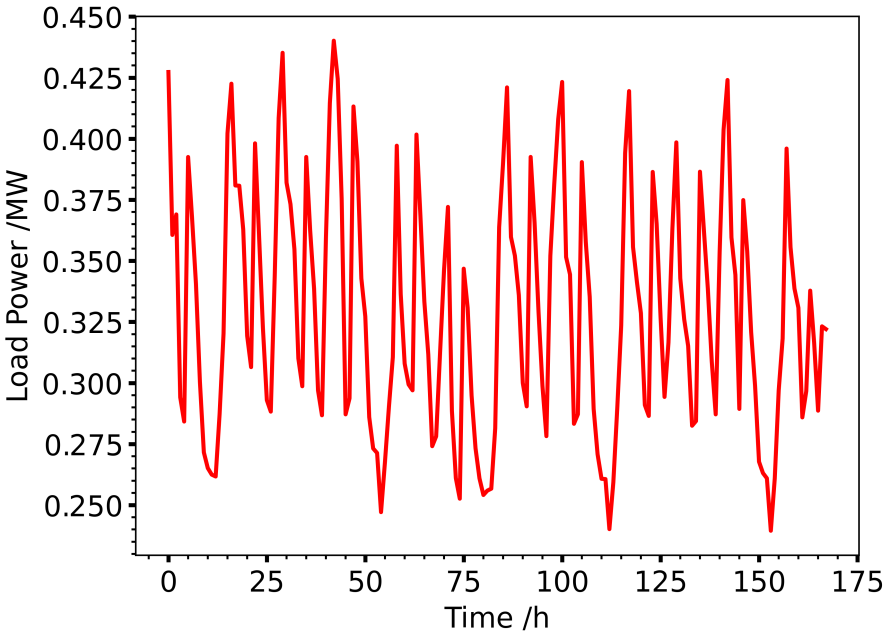

Figure 2.7: Historical data on consumer power. Source: CCEE (2024).

Unlike fixed and idealized profiles, real-world data incorporate hourly, seasonal, and behavioral fluctuations that directly impact electrical demand, allowing the energy management system (EMS) to operate in a more responsive and accurate manner. Moreover, electrical consumption exhibits high variability and stochastic behavior, reflecting unpredictable patterns associated with human activity, weather conditions, and the simultaneous use of various appliances. This variability underscores the importance of using historical data to capture realistic and probabilistic consumption trends.

In this context, deep learning techniques are particularly well-suited to model such complex dynamics. By automatically extracting temporal and nonlinear patterns from large volumes of historical data, deep neural networks can learn to forecast demand with high accuracy, even under volatile and nonstationary conditions. This enables the EMS to anticipate load variations more precisely, optimize the use of available energy resources, and enhance the stability and operational efficiency of the microgrid in real-time.

2.5 Modeling Disturbance using Artificial Intelligence

An effective strategy for modeling disturbances – such as solar and wind generation, as well as consumer demand – is the use of historical time series obtained from monitoring systems. These signals typically exhibit nonlinear dynamics, seasonal patterns, and long-term temporal dependencies, as demonstrated in the previous sections. Such characteristics pose challenges for traditional forecasting techniques, which often fail to capture the complex and nonstationary behavior inherent to these processes.

In this context, the Long Short-Term Memory (LSTM) architecture has emerged as a robust solution. As a type of recurrent neural network (RNN), LSTM is specifically designed to overcome common challenges in sequential data processing, such as vanishing or exploding gradients (Hochreiter & Schmidhuber 1997*a*, Greff et al. 2016). By incorporating memory cells and input, output, and forget control mechanisms, LSTM networks can retain relevant information over extended periods, capturing temporal dependencies and dynamic patterns with greater accuracy. These characteristics make LSTM particularly well-suited for forecasting energy generation and demand, where patterns evolve across multiple time scales.

In this context, the forecasting problem of time series representing wind and solar generation, as well as energy demand, can be formulated as a sequence-to-sequence regression task. The objective is to find a function $\boldsymbol{f} : d_{k-n:k} \rightarrow \hat{d}_{k+1}$ to forecast feedforward of past observations to a sequence of future values, effectively capturing the underlying temporal dynamics in the data, where the output $\hat{\mathbf{d}} \subseteq \mathbb{R}^{n_{\hat{d}}}$ and inputs $\mathbf{d} \subseteq \mathbb{R}^{n_d}$, and k is the current time step, n is the historical window size and m is the future forecast horizon. This formulation is particularly suitable for multi-step forecasting, where preserving the sequential dependencies between predicted values is essential for accurate and reliable predictions. Therefore, LSTM is defined as:

$$\hat{\mathbf{d}} = \boldsymbol{f}(\mathbf{d}; \boldsymbol{\Theta}, \boldsymbol{L}, \boldsymbol{M}) : \mathbb{R}^{n_d} \rightarrow \mathbb{R}^{n_{\hat{d}}} \tag{2.16}$$

where $\mathbf{d} \in \mathbb{R}^{n_d}$ is the input, $\hat{\mathbf{d}} \in \mathbb{R}^{n_{\hat{d}}}$ is the output, $\boldsymbol{\Theta}$ is a parameter containing the value of the corresponding synaptic weights and bias, $\boldsymbol{L}$ is the number of hidden layers and $\boldsymbol{M}$ is the number of neurons in each hidden layer. In this case, we propose

three LSTM networks, each with one input and one output.

$$d_1 : \{P_{solar}(k-n), \ldots, P_{solar}(k)\} \rightarrow \hat{d}_1 : \{P_{solar}(k+1)\} \tag{2.17}$$

$$d_2 : \{P_{wind}(k-n), \ldots, P_{wind}(k)\} \rightarrow \hat{d}_2 : \{P_{wind}(k+1)\} \tag{2.18}$$

$$d_3 : \{P_{load}(k-n), \ldots, P_{load}(k)\} \rightarrow \hat{d}_3 : \{P_{load}(k+1)\} \tag{2.19}$$

Training data were collected from the Brazilian Chamber of Electric Energy Commercialization (CCEE) (CCEE 2024) between 2020 and 2023 in the city of Guanambi, Bahia, Brazil, as shown in Figures 2.4, 2.5, and 2.7.

In deep learning-based models, the main goal is to train the model using previously observed data and then apply it to make predictions on new data. To prevent the model from simply memorizing the training data – instead of learning the underlying properties of the system – it is common practice to split the dataset into three subsets: (i) training, used to adjust the model's weights and enable it to learn the system dynamics; (ii) testing, used to monitor the model's performance during training and assist in hyperparameter tuning; and (iii) validation, used to evaluate the model's final performance after training. Table 2.1 summarizes the proportion allocated to each subset for the three LSTM-based models.

Table 2.1: Division of the dataset.

Disturbance	Train /(%)	Test /(%)	Validation /(%)
Solar	75	15	10
Wind	75	15	10
Load	75	15	10

The definition of the neural network hyperparameters was carried out experimentally, considering the specific characteristics of the problem and best practices reported in the literature. The adoption of a single LSTM layer proved sufficient to ensure satisfactory performance, in line with previous studies indicating the effectiveness of simplified structures in similar scenarios (Hochreiter & Schmidhuber 1997*b*, Greff et al. 2017). The learning rate was selected within a range commonly used in related works (0.001 to 0.01), ensuring stability in model convergence (Bengio 2012, Smith 2017). The number of neurons in each layer was initially defined based on values found in the literature and later adjusted according to the loss

Table 2.2: Hyperparameters adopted for the optimization.

Hyperparameter	Solar	Wind	Load
Hidden layers (L)	1	1	1
Neurons (M)	60	60	90
Epochs (E)	500	500	500
Learning rate	0.001	0.001	0.001
Batch size	32	32	32
Backward window	24	4	6

function evolution, following empirical optimization recommendations (Bergstra & Bengio 2012, Kelleher 2019). The batch size was chosen based on the hardware configuration Dell G15 laptop with 16GB RAM and an NVIDIA RTX 3050 GPU (NVIDIA Corporation 2023). The number of epochs was determined by observing the stabilization of the loss function, a widely adopted criterion to avoid overfitting (Prechelt 1998). The size of the backward window was defined according to the characteristics of each variable. For solar generation, a window of 24 time steps was used to allow the network to capture the daily seasonal cycle. For wind generation, a shorter window of 4 time steps was sufficient to represent the hourly dynamics. In the case of energy consumption, a 6-step window was adopted, reflecting the recurring cyclical behavior observed approximately every six hours.

The optimization problem was solved using the ADAM algorithm (Jais et al. 2019), implemented in Python through the TensorFlow library (Developers 2022). Thus, the optimization problem can be formulated as:

$$\min_{\Theta} \frac{1}{n_{train}} \sum_{i=1}^{n_{train}} \left| |\hat{\mathbf{d}} - \mathbf{d}_{train}| \right|_i^2 \tag{2.20}$$

Subject to (2.17), (2.18) or (2.19).

For model test, the Mean Squared Error (MSE) loss function was used.

$$\text{MSE}_{\text{test}} = \frac{1}{n_{test}} \sum_{i=1}^{n_{test}} \left(\hat{\mathbf{d}} - \mathbf{d}_{test} \right)_i^2 \tag{2.21}$$

The proposed LSTM model follows a Nonlinear AutoRegressive (NAR) structure, as it generates predictions based solely on past values of the system's output. Operating in discrete time steps, the network produces one-step-ahead forecasts

that are recursively fed back into the model to enable multi-step predictions. In this recursive forecasting scheme, each predicted output becomes part of the input for the subsequent step, requiring the internal states of the network to be updated iteratively to accurately capture the sequential dynamics of the system. This approach, which excludes exogenous inputs, aligns with the NAR paradigm as defined by Connor et al. (1994), and has been further developed in hybrid modeling contexts, such as in Zhang (2003).

2.6 Model of a microgrid

Another fundamental equation in the microgrid model is the power balance at the busbar, which ensures that the total power injected equals the total power consumed by loads, storage systems, and other connected components. This equation embodies the principle of energy conservation and is essential for maintaining the physical feasibility of the model. It is expressed as:

$$P_{solar} + P_{bat} + P_{grid} - P_{load} = 0 \tag{2.22}$$

Here, P_{solar} is the photovoltaic power, P_{solar} is the wind power, P_{bat} the battery charge/discharge power, and P_{grid} the power exchanged with the main grid.

Figure 2.8 shows a power converter shows a power converter where the actuation sides are indicated as Node Side (NS) and Component Side (CS).

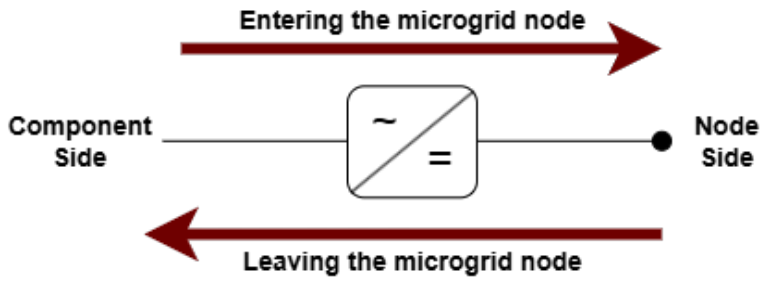

Figure 2.8: Efficiency consideration for power converters.

This mathematics is defined by:

$$P_i = \begin{cases} \text{Leaving the microgrid node} & if \;\; P_i > 0 \\ \text{Entering the microgrid node} & if \;\; P_i < 0 \end{cases} \tag{2.23}$$

P_i is power with the subscript i indicating one of the components of the microgrid.

With Equation (2.4), Equation (2.22), it is possible to obtain a linear algebraic state-space model in discrete time, as given by,

$$\underbrace{\begin{bmatrix} SOC(k+1) \end{bmatrix}}_{\mathbf{x}(k+1)} = \underbrace{\begin{bmatrix} 1 \end{bmatrix}}_{\mathbf{A}} \underbrace{\begin{bmatrix} SOC(k) \end{bmatrix}}_{\mathbf{x}(k)} + \underbrace{\begin{bmatrix} \frac{T_s \eta_{bat}}{C_{bat}} & 0 & 0 & 0 \end{bmatrix}}_{\mathbf{B}} \underbrace{\begin{bmatrix} P_{bat}(k) \\ P_{grid}(k) \end{bmatrix}}_{\mathbf{u}(k)} \tag{2.24}$$

$$\underbrace{\begin{bmatrix} 1 & 1 \end{bmatrix}}_{\mathbf{D}_u} \underbrace{\begin{bmatrix} P_{bat}(k) \\ P_{grid}(k) \end{bmatrix}}_{\mathbf{u}(k)} + \underbrace{\begin{bmatrix} 1 & -1 \end{bmatrix}}_{\mathbf{D}_d} + \underbrace{\begin{bmatrix} P_{solar}(k) \\ P_{load}(k) \end{bmatrix}}_{\mathbf{d}(k)} = 0 \tag{2.25}$$

storage levels $\mathbf{x}(k) \in \mathbb{R}^{nx}$ are influenced by the manipulated input $\mathbf{u}(k) \in \mathbb{R}^{nu}$, representing battery charging/discharging and grid power transactions. Disturbances $\mathbf{d}(k) \in \mathbb{R}^{nd}$ account for solar photovoltaic and load power variations. System dynamics are defined by matrices $\mathbf{A}$, $\mathbf{B}$, $\mathbf{C}$, $\mathbf{D}_u$, and $\mathbf{D}_d$ of appropriate dimensions.

2.7 Model in AVEVA process simulation

To represent a scenario closer to real operating conditions, the microgrid was modeled in AVEVA Process Simulation, which includes a dedicated library for renewable energy systems. The configuration proposed by Alarcón et al. (2022). was adapted and implemented in this environment, enabling detailed simulation of its components and evaluation of its performance under different operating conditions as shown in Figure 2.9.

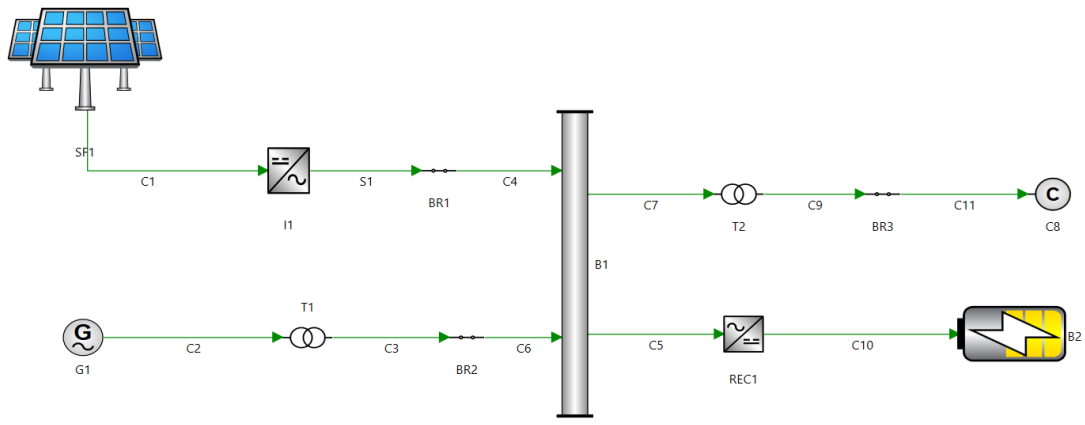

Figure 2.9: Residential microgrid modeled in AVEVA Process Simulation.

The microgrid consists of photovoltaic panels, a residential load, a battery bank, and access to the main power grid. The component details are summarized in Table 2.

Table 2.3: Symbols and descriptions of the components modeled in AVEVA Process Simulation.

Symbol	Description
SF1	Photovoltaic panel
S1,C1, C2, C4, C3, C5, C6, C7, C9, C10, C11	Conductor wire
C8	Load Consumer
G1	Main power grid
T1, T2	Transformer
I1	Inverter
REC1	Rectifier
BR1, BR2, BR3	Breaker
B1	Busbar
B2	Battery

2.8 Python-AVEVA Integration

The integration between Python and AVEVA was achieved through the SimCentralConnect class, which uses the pythonnet library to dynamically load the .NET assembly SimCentral.Client.Auto and establish an automation session (ScAutomation). To ensure portability across installations and versions, the routine employs a hierarchical client discovery: (i) paths already present in the Python environment; (ii) the directory defined by the environment variable (including the Scripting/DotNetFwk subfolders); and (iii) Windows Registry keys (HKCU/HKLM, including WOW6432Node). Once the assembly is located, the session is created via Connect or ConnectWithOptions, allowing optional execution logging (LogFile) for auditability. This Python–.NET bridge enables, in a programmatic and reproducible way, opening AVEVA Process Simulation models, reading and writing properties, triggering steady-state or dynamic runs, and collecting time-series data for variables of interest.

Chapter 3

A two-layer MPC strategy for energy management system

This chapter proposes a Quadratic Programming (QP)-based Model Predictive Control (MPC) formulation for energy management in microgrids. Traditionally, this type of problem is approached through an MPC law based on a Nonlinear Programming (NLP) formulation, due to the presence of a complementarity constraint that makes the problem nonlinear. In the proposed approach, this constraint is suitably removed, allowing the reformulation of the problem as a QP, thereby reducing the number of decision variables of the resulting optimization problem. To evaluate the benefits of the proposed QP-based approach, a case study was conducted using the AVEVA^{TM} Process Simulation integrated with Python. The results demonstrate that the QP formulation offers advantages such as greater numerical robustness, faster convergence of the optimization algorithm, and reduced computational time. These characteristics highlight the potential of the proposed methodology for real-time applications and confirm its feasibility for large-scale deployment and industrial implementation, where reliability and computational efficiency are critical requirements..

The text included here is partially published in the Simpósio Brasileiro de Automação Inteligente:
CALHAU, F. A. S.; MEIRA, R. L.; BISPO, H.; MARTINS, M. A. F. A two-layer MPC strategy for microgrid energy management within a software-in- the-loop scheme with AVEVA Process Simulation. XVII Simpósio Brasileiro de Automação Inteligente. São João del Rey: 2025.

3.1 Revisiting two-Layer MPC based on nonlinear programming

Alarcón et al. (2022) proposed a residential microgrid composed of photovoltaic panels, a lithium-ion battery system, consumer loads, and a connection to the main electrical grid. Figure 3.1 provides a schematic representation of the architecture, highlighting the interconnections among components and the overall system integration.

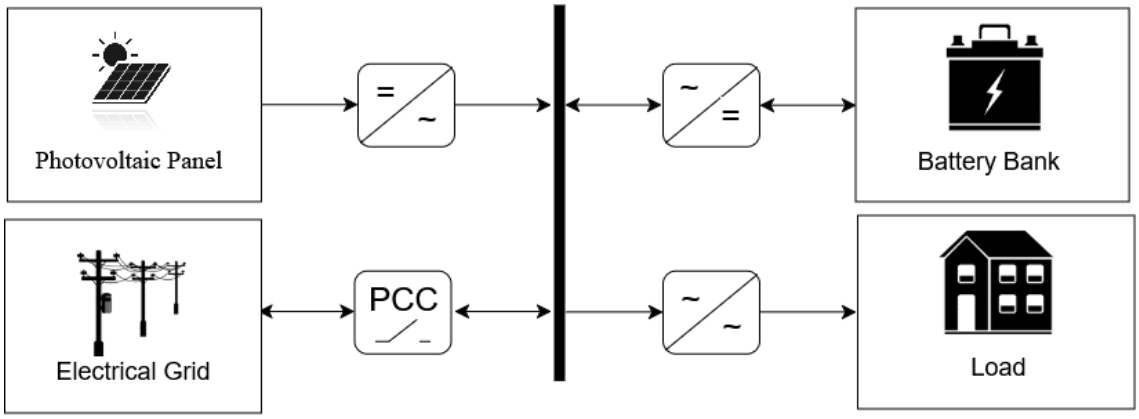

Figure 3.1: Architecture for residential microgrid. (Adapted from Alarcón et al. 2022.)

To derive a discrete-time linear state-space model for this microgrid, the concepts introduced in Chapter 2 are applied. The state-of-charge dynamics are modeled using Equation (2.5), while the power balance is represented by Equation(2.22). Accordingly, the model is formulated as follows:

$$\underbrace{\begin{bmatrix} SOC(k+1) \end{bmatrix}}_{\mathbf{x}(k+1)} = \underbrace{\begin{bmatrix} 1 \end{bmatrix}}_{\mathbf{A}} \underbrace{\begin{bmatrix} SOC(k) \end{bmatrix}}_{\mathbf{x}(k)} + \underbrace{\begin{bmatrix} \frac{T_s \eta_{bat}}{C_{bat}} & -\frac{T_s}{C_{bat}\eta_{bat}} & 0 & 0 \end{bmatrix}}_{\mathbf{B}} \underbrace{\begin{bmatrix} P_{bat,c}(k) \\ P_{bat,d}(k) \\ P_{grid,s}(k) \\ P_{grid,p}(k) \end{bmatrix}}_{\mathbf{u}(k)} \tag{3.1}$$

$$\underbrace{\begin{bmatrix}1 & -1 & -1 & 1\end{bmatrix}}_{\mathbf{D}_u}\underbrace{\begin{bmatrix}P_{bat,c}(k)\\ P_{bat,d}(k)\\ P_{grid,s}(k)\\ P_{grid,p}(k)\end{bmatrix}}_{\mathbf{u}(k)}+\underbrace{\begin{bmatrix}1 & -1\end{bmatrix}}_{\mathbf{D}_d}+\underbrace{\begin{bmatrix}P_{solar}(k)\\ P_{load}(k)\end{bmatrix}}_{\mathbf{d}(k)}=0 \tag{3.2}$$

The economic cost function optimizes microgrid performance by minimizing energy purchases to promote self-sufficiency and maximizing energy sales to ensure economic viability (ℓ_{grid}). Battery-related costs are also considered and include: cell replacement (ℓ_{bat1}), representing the cost of replacing each battery cell as it undergoes charge and discharge cycles; charge/discharge degradation (ℓ_{bat2}), included to minimize the impact of voltage and current on battery lifespan; and state-of-charge variation (ℓ_{bat3}), which mitigates abrupt charge/discharge cycles to preserve battery integrity.

The microgrid is assumed to operate in grid-connected mode, and the MPC strategy is designed to maximize energy export to the main grid. To support this objective, different electricity tariffs for buying and selling are considered. These tariffs vary throughout the day according to three predefined time periods: peak (6:00 p.m. to 11:59 p.m.), off-peak (11:00 p.m. to 5:59 a.m.), and intermediate (6:00 a.m. to 5:59 p.m.). The corresponding prices are presented in Table 3.1.

Table 3.1: Price of electricity.

Zone	Time /(h)	Price /($/kWh)
Peak	from 6:00 p.m. to 11:59 p.m.	0.015
Off-peak	from 11:00 p.m. to 5:59 a.m	0.1
Intermediate	from 6:00 a.m. to 5:59 p.m	0.05

The expression representing the cost associated with grid usage is given by:

$$\ell_{grid}(u(k),p_e) = p_e(k)T_s[\lambda_1 P_{grid,p}(k) - \lambda_2 P_{grid,s}(k)], \tag{3.3}$$

where p_e is the price of electricity, $P_{grid,p}$ is the power purchase to and $P_{grid,s}(k)$ the power sale to grid, λ_1 and λ_2, respectively, to adjust energy selling strategies.

With the knowledge of the replacement value C_{re} and the capacity for storing nominal energy C_{Wh} for the system's batteries, it can be deduced that:

$$\ell_{bat1} = \frac{C_{re}T_s}{C_{Wh}}[\lambda_3 P_{bat,c}(k) + \lambda_4 P_{bat,d}(k)], \tag{3.4}$$

This term quantifies a usage cost associated with the stored energy, where λ_3 and λ_4 are weighting coefficients that assign greater or lesser priority to this objective within the overall optimization framework.

One of the internal factors that affect battery life expectancy is the magnitude of the currents during operation. Therefore, by considering the charging and discharging power values along with the nominal voltage and current ratings of the battery bank, the following relationship can be established:

$$\ell_{bat2} = \lambda_5 \frac{P_{bat,c}(k) + P_{bat,d}(k)}{V_{bat} I_{bat}} \tag{3.5}$$

where λ_5 to minimize economic and operational impacts.

Another factor that affects the aging cycle is the average state of charge, as well as abrupt fluctuations that may occur over time. The degradation process becomes more pronounced when there are significant changes in the state of charge between consecutive time intervals. To mitigate this undesirable effect, the following weighted quadratic function is proposed:

$$\ell_{bat,3} = \|x(k+1) - x(k)\|^2_{Q_{bat}} \tag{3.6}$$

The function integrates these aspects to ensure system efficiency and viability.

$$\begin{aligned} &\ell_{eco}(x(k),u(k),p_e(k)) = \\ &\overbrace{p_e(k)T_s[\lambda_1 P_{grid,p}(k) - \lambda_2 P_{grid,s}(k)]}^{\ell_{grid}} \\ &+ \overbrace{\frac{C_{re}T_s}{C_{Wh}}[\lambda_3 P_{bat,c}(k) + \lambda_4 P_{bat,d}(k)]}^{\ell_{bat1}} \\ &+ \overbrace{\lambda_5 \frac{P_{bat,c}(k) + P_{bat,d}(k)}{V_{bat} I_{bat}}}^{\ell_{bat2}} + \overbrace{\|x(k+1) - x(k)\|^2_{Q_{bat}}}^{\ell_{bat3}} \end{aligned} \tag{3.7}$$

The microgrid operation is optimized by balancing power purchase $P_{grid,p}(k)$ and sale $P_{grid,s}(k)$ to the grid, weighted by λ_1 and λ_2, respectively, to adjust energy selling strategies. Battery charging $P_{bat,c}(k)$ and discharging $P_{bat,d}(k)$ are weighted by

λ_3 and λ_4, adjusted to balance their influence. The model includes the cell replacement cost C_{re} and coefficient λ_5 to minimize economic and operational impacts, considering battery voltage V_{bat}, current I_{bat} and $p_e(k)$ the electricity price. This ensures efficient and economically viable energy management.

Based on this formulation, the control law executed at time step k with $\mathbf{x}(k)$ known, given by:

$$\begin{aligned}\min_{\mathbf{u}_k,\mathbf{x}_s,\mathbf{u}_s} V_k = \sum_{j=0}^{N-1} &||\mathbf{x}(k+j|k) - \mathbf{x}_s||^2_{\mathbf{Q}} + ||\Delta\mathbf{u}(k+j|k)||^2_{\mathbf{R}} \\ &+ ||\mathbf{u}(k+j|k) - \mathbf{u}_s||^2_{\mathbf{Q}_u} + ||\mathbf{x}_s - \mathbf{x}_e||^2_{\mathbf{Q}_x} + ||\mathbf{u}_s - \mathbf{u}_e||^2_{\mathbf{Q}_s} \end{aligned} \tag{3.8}$$

Subject to (3.1), (3.2) and to:

$$\mathbf{x}_s = \mathbf{A}\mathbf{x}_s + \mathbf{B}\mathbf{u}_s, \tag{3.9}$$

$$\mathbf{B}_u\mathbf{u}_s(k) + \mathbf{B}_d\mathbf{d}(k) = 0, \tag{3.10}$$

$$\mathbf{x}(k+N|k) = \mathbf{x}_s, \tag{3.11}$$

$$\mathbf{x} \in \mathbb{X},\ \mathbf{x}_s \in \mathbb{X}, \tag{3.12}$$

$$\mathbf{u} \in \mathbb{U},\ \mathbf{u}_s \in \mathbb{U}, \tag{3.13}$$

where $\mathbf{u}_k$ is the entire sequence of calculated optimal inputs, $\mathbf{u}_s$ and $\mathbf{x}_s$is the artificial reference point, representing the best steady-state-input pair the con trolled system can reach in N steps, at the current time. $\mathbf{Q}$, $\mathbf{Q}_x$, $\mathbf{Q}_s$ and $\mathbf{Q}_u$ are assumed to be positive semi-definite tuning matrices, while $\mathbf{R}$ are positive definite tuning matrices, each of appropriate dimensions.

Regarding constraints, (3.9) and (3.10) ensures the artificial reference is a system equilibrium and (3.11) enforces a terminal equality constraint, requiring the predicted state to match the artificial reference at the end of the control horizon. Constraints (3.12) and (3.23) define bounds on states and inputs, with (3.24) and (3.15) as compact-convex sets for feasible regions.

$$\mathbb{X} = \left\{\mathbf{x} \in \mathbb{R}^{nx} \mid \mathbf{x}_{\min} \le \mathbf{x} \le \mathbf{x}_{\max}\right\}, \tag{3.14}$$

$$\mathbb{U} = \left\{ \mathbf{u} \in \mathbb{R}^{nu} \;\middle|\; \begin{array}{l} \mathbf{u}_{\min} \le \mathbf{u} \le \mathbf{u}_{\max}, \\ \\ \mathbf{u}_i(k)\mathbf{u}_{i+1}(k) = 0,\ i = 1 \text{ and } 3 \end{array} \right\}. \tag{3.15}$$

The constraint $\mathbf{u}_i(k)\,\mathbf{u}_{i+1}(k) = 0$ for $i = 1$ and $i = 3$ introduces nonlinearity into the optimization problem. Specifically, considering the control vector $\mathbf{u}(k)$ as defined in the table, where each element is indexed from 1 to 4, this constraint enforces that the product of certain consecutive control inputs must be zero. These elements are defined as: $u_1(k) = P_{bat,c}(k)$, $u_2(k) = P_{bat,d}(k)$, $u_3(k) = P_{grid,p}(k)$, and $u_4(k) = P_{grid,s}(k)$. Therefore, for $i = 1$ and $i = 3$, the constraint specifically targets mutually exclusive operating modes: charging and discharging of the battery, and importing and exporting power to/from the electrical grid, respectively.

The explicit modeling of charging and discharging power seeks to more accurately capture the dynamic behavior of the battery. However, this formulation introduces substantial challenges, as it splits a single physical variable into two artificial control inputs, thereby requiring the enforcement of a complementarity constraint ($P_{bat,c}(k) \cdot P_{bat,d}(k) = 0$) to prevent simultaneous charging and discharging. While this constraint is physically consistent, it introduces discontinuities into the solution space, making the optimization problem non-differentiable. As a result, gradient-based optimization methods – widely used for their computational efficiency – become unsuitable or ineffective. Furthermore, the presence of complementarity conditions may cause convergence issues, increase computational time, and hinder real-time implementation of the control strategy.

The controller formulation requires prior knowledge of the economically optimal equilibrium point $(\mathbf{x}_e, \mathbf{u_e})$, determined by solving a static optimization problem in an economic steady-state target layer.

$$\min_{\mathbf{x}_e, \mathbf{u_e}} \ell_{eco} \tag{3.16}$$

$$\text{s.t:} \quad \mathbf{x}_e = \mathbf{A}\mathbf{x}_e + \mathbf{B}\mathbf{u}_e, \tag{3.17}$$

$$\mathbf{x_e} \in \mathbb{X}, \ \mathbf{u_e} \in \mathbb{U}. \tag{3.18}$$

3.2 Propose two-Layer MPC based on quadratic programming

To reformulate the problem as a Quadratic Programming (QP) problem, the modeling framework introduced in Chapter 2 is adopted. Specifically, Equation (2.4)

is used to represent the state-of-charge dynamics, while Equation (2.22) defines the power balance. Accordingly, the resulting formulation is given as follows:

$$\underbrace{\begin{bmatrix} SOC(k+1) \end{bmatrix}}_{\mathbf{x}(k+1)} = \underbrace{\begin{bmatrix} 1 \end{bmatrix}}_{\mathbf{A}} \underbrace{\begin{bmatrix} SOC(k) \end{bmatrix}}_{\mathbf{x}(k)} + \underbrace{\begin{bmatrix} \frac{T_s \eta_{bat}}{C_{bat}} & 0 & 0 & 0 \end{bmatrix}}_{\mathbf{B}} \underbrace{\begin{bmatrix} P_{bat}(k) \\ P_{grid}(k) \end{bmatrix}}_{\mathbf{u}(k)} \tag{3.19}$$

$$\underbrace{\begin{bmatrix} 1 & 1 \end{bmatrix}}_{\mathbf{D}_u} \underbrace{\begin{bmatrix} P_{bat}(k) \\ P_{grid}(k) \end{bmatrix}}_{\mathbf{u}(k)} + \underbrace{\begin{bmatrix} 1 & -1 \end{bmatrix}}_{\mathbf{D}_d} + \underbrace{\begin{bmatrix} P_{solar}(k) \\ P_{load}(k) \end{bmatrix}}_{\mathbf{d}(k)} = 0 \tag{3.20}$$

This reformulation enables the problem to be modeled as a QP problem by considering battery power as a single variable, where the sign indicates the mode of operation: negative for discharging and positive for charging. Unlike the previous approach, which used two separate variables with distinct efficiencies for charging and discharging, this simplification eliminates the need for such a separation. As discussed in Chapter 2, this transformation is valid when the battery efficiency is close to 1 – a condition often observed in practice.

By rewriting the economic cost function to conform with a QP formulation, we obtain:

$$\begin{aligned} \ell_{eco}(x(k),u(k),p_e(k)) = &-\lambda_{grid} p_e(k) P_{grid}(k) T_s + \frac{C_{re}}{C_{Wh}} \lambda_{bat} P_{bat}(k) + \\ &+\lambda_{bat2} \frac{P_{bat}(k)}{V_{bat} I_{bat}} + ||x(k+1) - x(k)||^2_{Q_{bat}} \end{aligned} \tag{3.21}$$

where $P_{grid}(k)$ denotes the power exchanged with the main grid (positive for selling and negative for purchasing), and $P_{bat}(k)$ represents the battery's charging/discharging power. The constants λ_{grid} and λ_{bat} are weighting factors that prioritize energy selling and battery charging when set to lower values. Additionally, λ_{bat2} is a degradation-related weight; reducing its value increases the emphasis on battery aging during charging. This formulation allows for efficient and balanced system operation by aligning economic objectives with operational constraints.

The control law executed at time step k with $\mathbf{x}(k)$ known, given by:

$$\min_{\mathbf{u}_k, \mathbf{x}_s, \mathbf{u}_s} V_k = \sum_{j=0}^{N-1} ||\mathbf{x}(k+j+1) - \mathbf{x}_s||^2_{\mathbf{Q}} + ||\Delta \mathbf{u}(k+j)||^2_{\mathbf{R}}$$

$$+ ||\mathbf{u}(k+j) - \mathbf{u}_s||^2_{\mathbf{Q}_u} + ||\mathbf{x}_s - \mathbf{x}_e||^2_{\mathbf{Q}_x} + ||\mathbf{u}_s - \mathbf{u}_e||^2_{\mathbf{Q}_s} \tag{3.22}$$

Subject to (3.19), (3.20), (3.9), (**??**), (3.10), (3.11), (3.12) and to:

$$\mathbf{u} \in \mathbb{U},\, \mathbf{u}_s \in \mathbb{U}, \tag{3.23}$$

Therefore, by removing the complementarity constraint, a new set of input variables is defined as follows:

$$\mathbb{U} = \{\mathbf{u} \in \mathbb{R}^{nu} \mid \mathbf{u}_{\min} \leq \mathbf{u} \leq \mathbf{u}_{\max}\} \tag{3.24}$$

The controller formulation requires prior knowledge of the economically optimal equilibrium point $(\mathbf{x}_e, \mathbf{u}_e)$, which is obtained by solving a static optimization problem within the economic steady-state target layer, as defined in Equations (3.16), (3.17), and (3.18).

Table 3.2 summarizes the differences between the controllers NLP-based MPC and QP-based MPC.

Table 3.2: Differences between manipulated variables and bounds constraints.

NLP-based MPC	QP-based MPC
$\mathbf{u}(k) = \begin{pmatrix} P_{bat,c}(k) \\ P_{bat,d}(k) \\ P_{grid,p}(k) \\ P_{grid,s}(k) \end{pmatrix}$	$\mathbf{u}(k) = \begin{pmatrix} P_{bat}(k) \\ P_{grid}(k) \end{pmatrix}$
$\begin{pmatrix} 0\text{ kW} \\ 0\text{ kW} \\ 0\text{ kW} \\ 0\text{ kW} \end{pmatrix} \leq \mathbf{u}(k) \leq \begin{pmatrix} 2.4\text{ kW} \\ 2.4\text{ kW} \\ 3.0\text{ kW} \\ 2.1\text{ kW} \end{pmatrix}$	$\begin{pmatrix} -2.4\text{ kW} \\ -2.1\text{ kW} \end{pmatrix} \leq \mathbf{u}(k) \leq \begin{pmatrix} 2.4\text{ kW} \\ 3.0\text{ kW} \end{pmatrix}$
$\mathbf{Q} = 1\%$	$\mathbf{Q} = 1\%$
$\mathbf{Q}_x = 1\%$	$\mathbf{Q}_x = 1\%$
$\mathbf{R} = \text{diag}(1,\, 1,\, 1,\, 1)$ kW	$\mathbf{R} = \text{diag}(1,\, 1)$ kW
$\mathbf{Q}_u = \text{diag}(1,\, 1,\, 1,\, 1)$ kW	$\mathbf{Q}_u = \text{diag}(1,\, 1)$ kW
$\mathbf{Q}_s = \text{diag}(1,\, 1,\, 1,\, 1)$ kW	$\mathbf{Q}_s = \text{diag}(1,\, 1)$ kW

Remark 3.1 The weights $\mathbf{R}$, $\mathbf{Q}_u$, and $\mathbf{Q}_s$ for the NLP-based MPC and QP-based MPC are normalized by the maximum value of the corresponding variable to ensure compatibility with $\mathbf{Q}$.

3.3 Simulation and results

To assess the impact of transitioning from an NLP-based MPC to a QP-based MPC in a microgrid energy management system, simulations were conducted using Python 3.12 and AVEVA$^{\text{TM}}$ Process Simulation, modeled according to Section 2.7 of Chapter 2. For the NLP formulation, the `minimize` function from the SciPy library was employed – using the Sequential Quadratic Programming (SQP) algorithm (Gommers et al. 2022). For the QP formulation, the CVXOPT framework was used (Andersen et al. 2020).

In Figure 3.2, a block diagram of the proposed control loop for the residential microgrid is presented.

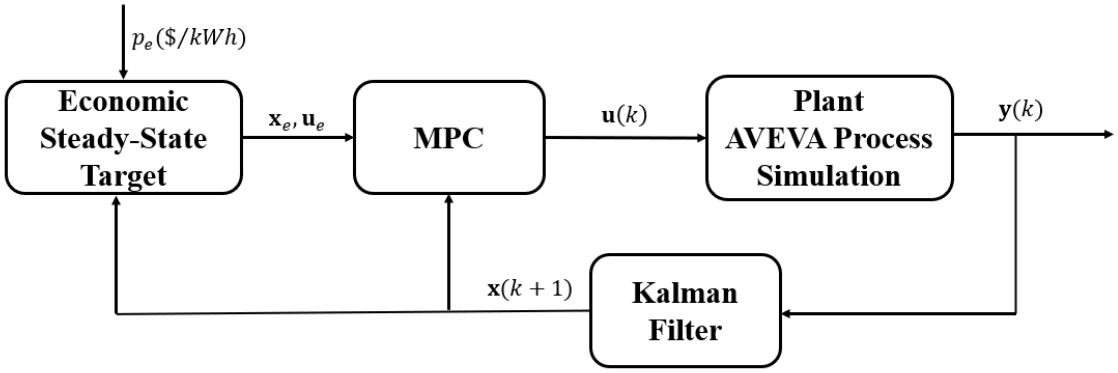

Figure 3.2: Block diagram of EMS. Where $P_e(\$/kWh)$ is electrical price, $\mathbf{x_e}$ and $\mathbf{u_e}$ are equilibrium point, $\mathbf{u}(k)$ is input, $\mathbf{y}(k)$ is output, and $\mathbf{x}(k+1)$ is measured process output.

Finally, it is important to highlight the use of the Kalman filter in Figure 3.2, which is employed to re-estimate the artificial states of the controller's linear model. Furthermore, as in the state-space model, the Kalman gain is updated successively.

The results of the MPC controller are presented in Figures 3.3. Figures 3.3(a) and 3.3(c) correspond to the QP-based MPC, while Figures 3.3(b) and 3.3(d) correspond to the NLP-based MPC. Subfigures (a) and (b) display the manipulated variables and external disturbances; in these plots, positive values represent battery

discharging and energy purchased from the grid, whereas negative values indicate battery charging and energy exported to the grid. Subfigures (c) and (d) illustrate the evolution of the battery state of charge over time.

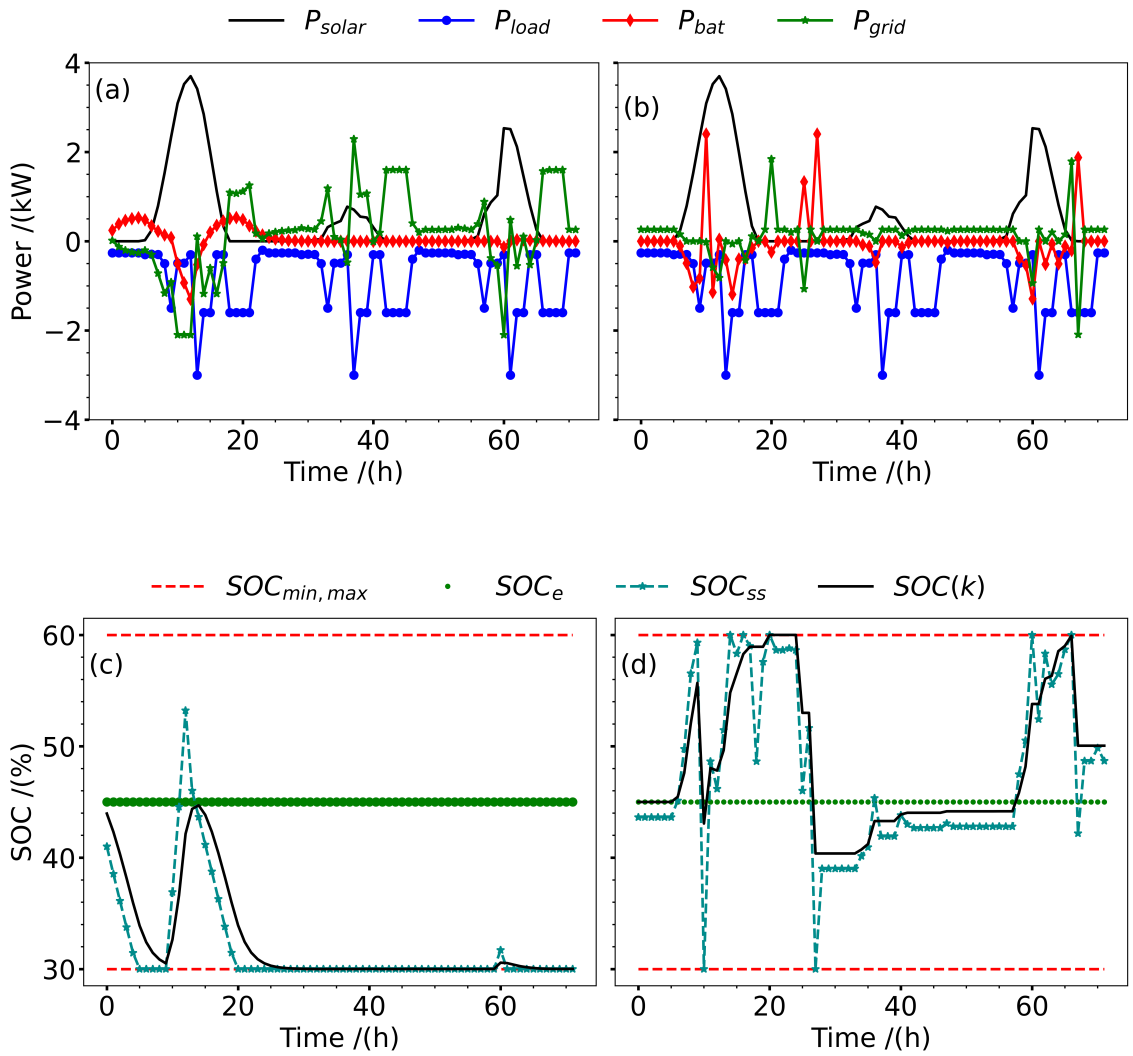

Figure 3.3: Comparison between QP-based and NLP-based MPC strategies. Subplots (a) and (c) correspond to the QP-based MPC, while (b) and (d) represent the NLP-based MPC. Subplots (a) and (b) show the manipulated variables and disturbances: P_{bat} denotes the power exchanged with the battery bank, P_{grid} the power purchased from or sold to the grid, P_{solar} the available solar generation, and P_{load} the power demand. Subplots (c) and (d) display the battery's state of charge $SOC(k)$, where SOC_e is the economic target, $SOC_{\text{min,max}}$ define the operational limits, and SOC_{ss} is the artificial steady-state reference.

In both simulations, the battery's initial state of charge was set to $SOC(0) = 45$. Figures 3.3(a) and 3.3(c) demonstrate that the controller operates optimally and in

real time, consistently satisfying constraints on manipulated variables and battery charge. During periods of high renewable generation, the system prioritizes selling surplus energy, maintaining this strategy throughout the simulation.

However, the NLP formulation splits a single physical variable into two, which can create challenges in controller tuning, especially in defining the $\mathbf{R}$ matrix. One example occurs when adjusting the battery charging parameters, which requires careful consideration of the corresponding discharge values and may lead to conflicts between the algorithm's objectives. This problem is illustrated in Figure 3.4(b), where the algorithm oscillates between feasible and infeasible solutions over time. The abrupt variation in the optimization status indicates that, although feasible solutions are often found, they quickly revert to infeasibility, revealing a lack of robustness in the optimization process. This instability arises from violations of the complementarity constraint at certain points, since the conflict between charging/discharging and buying/selling causes these actions to occur simultaneously, preventing the power balance — represented by the Equation (3.2) — from reaching zero, as shown in Figure 3.4(c). In contrast, throughout the entire simulation, the QP-based formulation fully satisfies the equality constraint.

The fundamental cause of this issue lies in the nature of the nonlinear constraint, as shown in Equation 3.15. This constraint imposes a complementarity condition, requiring at least one of the variables to be zero, which makes the problem non-differentiable and non-convex. These characteristics significantly hinder the application of gradient-based methods. Furthermore, the combinatorial nature of this constraint forces the algorithm to alternate between two mutually exclusive states – such as charging or discharging the battery, or buying and selling energy – behavior that resembles a discrete problem and is inherently incompatible with continuous, gradient-based approaches.

As a result, in transition regions where both variables may take positive values or are near the switching point, the gradient becomes ill-defined, impairing the algorithm's convergence. This typically occurs during abrupt changes in energy generation: for example, when there is a surplus of generated energy, the controller chooses to charge the battery or sell to the grid; in the following time step, with reduced availability, it must discharge the battery or draw energy from the grid. Such

abrupt shifts lead to oscillations between feasible and infeasible solutions, making it difficult for the numerical solver to consistently satisfy the constraints.

Even if a suitable tuning is found for the NLP formulation, allowing feasible solutions, an increasing discrepancy between the plant and the model can degrade the performance of the controller's weights, leading the system to infeasible solutions.

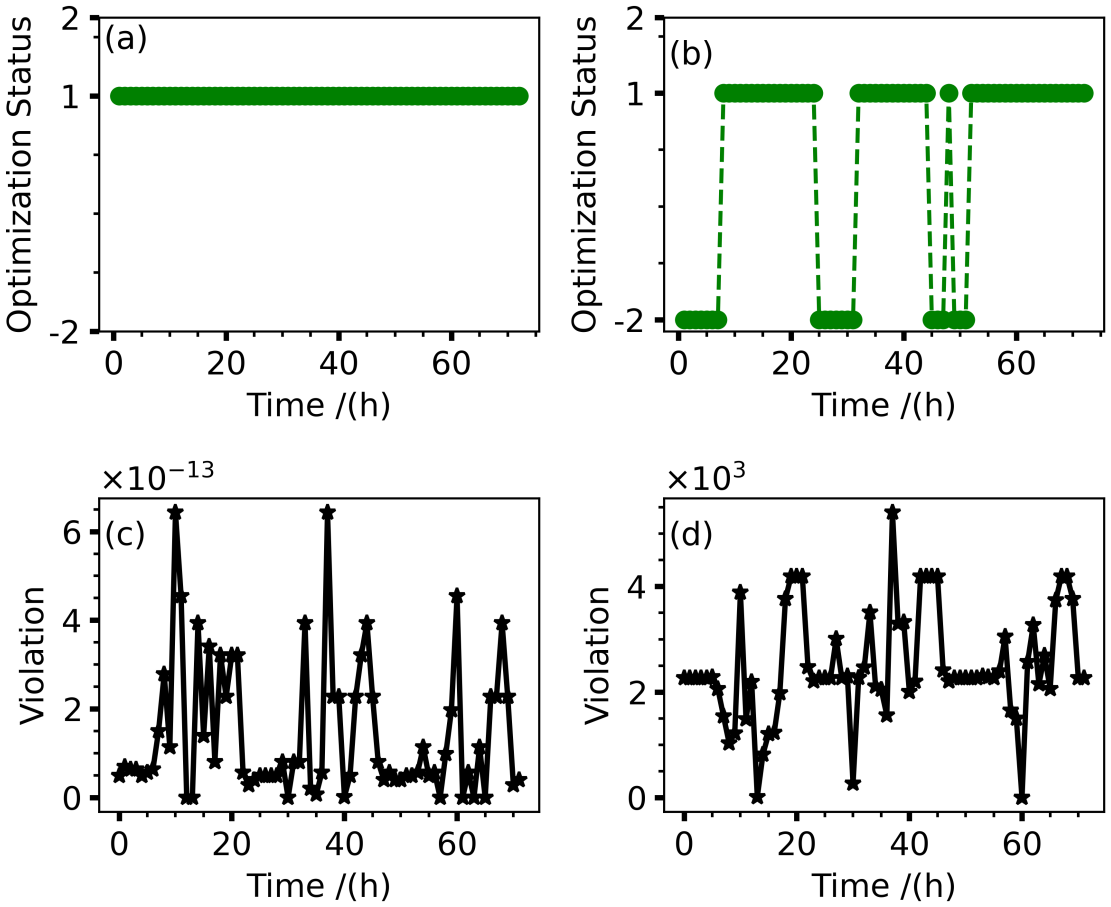

Figure 3.4: The optimization status and constraint violation of (a) and (c) QP-based MPC and (b) and (d) NLP-based MPC. The status indicate: 1 (converged) and -2 (did not converge). It is accompanied by a figure comparing the performance of the two methods.

In contrast, in the QP formulation, the use of a single variable to represent the battery simplifies the tuning process, facilitating the definition of the algorithm's objectives. Figure 3.4(a) shows that this approach enhances the optimizer's convergence, which remains stable throughout the entire simulation. This strategy exhibits greater robustness and efficiency in solving the optimization problem. Furthermore, in the absence of nonlinear constraints, all other constraints are strictly satisfied, as evidenced by the dimensionless violation shown in Figure 3.4(c), with values on the

order of 10^{-13}, which are residual and consistent with the solver's numerical error.

In Figure 3.5, it can be observed that the QP-based MPC approach achieves execution times up to 70% shorter compared to the NLP-based approach. Furthermore, Figure 3.5(a) stands out from Figure 3.5(b) by exhibiting significantly lower variability in execution times, indicating that the corresponding method is more consistent and predictable in its performance.

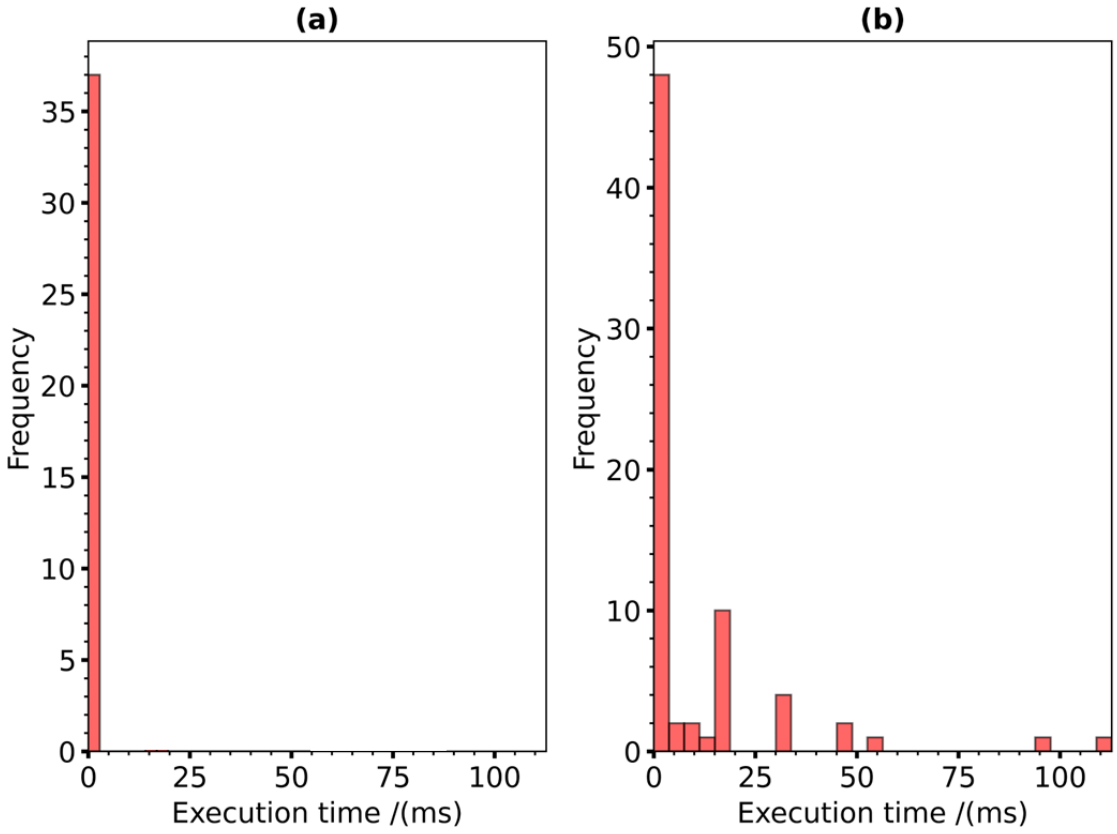

Figure 3.5: Comparison between the execution time of the two approaches: (a) execution time of the QP-based MPC; (b) execution time of the NLP-based MPC.

In contrast, NLP-based MPC can achieve results comparable to those of the QP-based approach, provided that proper tuning is performed—particularly in the $\mathbf{R}$ matrix, which suppresses excessive movements of the manipulated variables. However, this process is more laborious, as it requires finding parameters that prevent conflicts between charging/discharging and buying/selling actions. Moreover, this formulation is more challenging for real-time applications due to its reliance on computationally expensive iterative methods, which often fail to meet strict time constraints. On the other hand, QP-based MPC is better suited for industrial-scale

applications, offering greater computational efficiency and significantly shorter execution times. Its ease of integration with system dynamics and reduced sensitivity to numerical precision loss further reinforce its position as the preferred choice for real-time industrial applications, where speed, reliability, and extensibility are indispensable.

In terms of extensibility, QP-based MPC excels in handling increasingly complex systems, such as those involving multiple interconnected agents — like purchase-sell operations among numerous suppliers and buyers, management of multiple batteries, operation of green hydrogen plants, or coordination of large consumer networks. While NLP-based approaches struggle with exponential increases in execution time as binary variables and system complexity growth, QP-based MPC maintains efficiency even with larger problem sizes, ensuring optimal solutions within acceptable timeframes.

This efficient extensibility is crucial in modern industrial settings, in which managing multiple resources and dynamic interactions are essential. QP-based MPC not only meets current demands but also provides a robust foundation for scaling complex systems, making it the ideal approach for applications that require extensibility without sacrificing performance.

3.4 Conclusion

In this chapter, a two-layer Model Predictive Control (MPC) strategy based on Quadratic Programming (QP) was proposed for energy management in microgrids. The main modification consisted of reformulating the state equation related to battery storage: instead of treating charging and discharging power as separate variables, a single power variable was adopted, with its sign indicating the mode of operation — positive for charging and negative for discharging. This simplification enabled the replacement of the Nonlinear Programming (NLP) formulation with a QP-based approach, resulting in a convex control problem.

To validate the proposed method, a case study widely discussed in the literature was used, originally modeled with a nonlinear control law. Simulations were carried out using the AVEVA process simulation environment and Python, through

a software-in-the-loop strategy, allowing integration between the control model and the simulated plant. The results showed that the QP-based control law achieved significant improvements, including guaranteed optimal solutions, enhanced numerical stability, and algorithm convergence, while also reducing computational time and facilitating real-time implementation.

3.5 Appendix - Microgrid in AVEVA Process Simulation

The microgrid modeled in AVEVA Process Simulation consists of a photovoltaic panel, battery bank, consumer load and access to the main grid.

The SolarFarm model (Figure 3.6) calculates the output power of one or more solar/photovoltaic panels. To determine the panel's output power, the solar radiance, area, and module efficiency must be provided. The solar radiation data from the city of Avellaneda, Santa Fe province, Argentina.

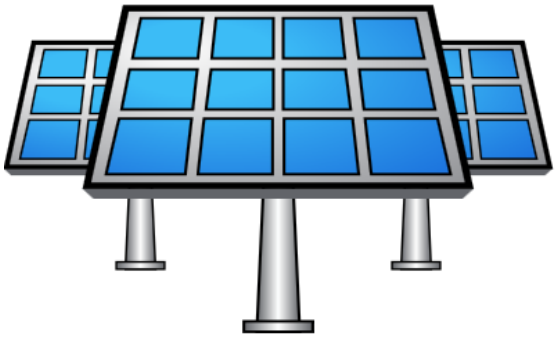

Figure 3.6: Renewables SolarFarm.

The configurations used for modeling the photovoltaic panel are summarized in Table 3.3.

Table 3.3: Photovoltaic Panel Specifications.

Symbol	Description	Value
Nseries	Number of panels in series	6
Nparallel	Number of panels in parallel	2
A	Area of single panel	1.635 m^2
eta	Efficiency from manufacturer	15%
alpha	Cell temperature coefficient of power	-0.47%/°C
V	Voltage of a single panel	0.024 kV
Lsoil	Losses from dirt and dust on panels	2%
Lshade	Losses from shading of panels	3%
Lsnow	Losses from snow covering panels	0%
Lmis	Losses from mismatched voltage and current	2%
Lwire	Losses from wiring	2%
Lconn	Losses from electrical panel connections	0.5%
Lrate	Losses from rated–actual output difference	1%
Lage	Losses resulting from aged panels	0%
Lavail	Losses from system shutdowns and maintenance	3%

The Battery model (Figure 3.7) allows the sizing of a lithium-ion battery bank, the dynamic simulation of renewable energy storage, and its integration with existing models in the Renewables library. In the context of renewable energy storage, lithium-ion batteries have recently become very popular due to their performance and lifespan.

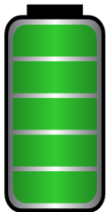

Figure 3.7: Battery Bank

The configurations used to model the battery bank are summarized in Table 3.4.

Table 3.4: Photovoltaic Panel Specifications.

Symbol	Description	Value
Nseries	Number of battery in series	4
Nparallel	Number of battery in parallel	1
tau	Runtime for supplying an output current	24 h
Ebank	Bank energy	21120 Wh
Vbank	Bank voltage	52.8 V
Qcell	Capacity of single battery	400 Ah
Icurve	Current from the discharge curve	715.085 A
Qexp	Capacity between exponential and nominal zones	22.5 Ah
Vexp	Voltage between exponential and nominal zones	52.8 V
Qnom	Capacity between nominal and nominal zones	30 Ah
Vnom	Capacity between nominal and nominal zones	52.8 Ah

The generator (Figure 3.8) is a simple electrical power source, either alternating current (AC) or direct current (DC), that allows specifying the power contribution from non-renewable sources to the grid by either directly defining the output power or providing a supply curve. It can also operate as a consumer of mechanical power or convert mechanical power into electrical power.

Figure 3.8: Generator

The configurations used to model the generator are summarized in Table 3.5.

Table 3.5: Photovoltaic Panel Specifications.

Symbol	Description	Value
Npoles	Number of poles	2
P	Generator output power	308 W
V	Voltage	240 V

The inverter model converts direct current (DC) into alternating current (AC)

within an electrical flow. In renewable energy systems, inverters are widely used to transform the DC power generated by solar plants into AC power, enabling connection to the electrical grid.

In AVEVA Process Simulation, the inverter's overall efficiency is calculated, by default, using a quadratic loss model (Driesse et al. 2008). The default parameters of this model were defined based on data obtained by the National Renewable Energy Laboratory (NREL) from measurements conducted by the California Energy Commission (Dobos 2013). The model is adjusted to match the inverter's nominal efficiency, allowing the overall efficiency to be determined as a function of the load fraction. The default values ($\eta_{nom} = 96\%$ and $\eta_{ref} = 96.37\%$) are suitable for most applications but can be adapted to meet specific requirements. Alternatively, a custom efficiency curve can be provided to calculate inverter performance at different load fractions.

The rectifier (Figure 3.9) model converts alternating current (AC) to direct current (DC) for use in equipment such as electrolyzers for clean hydrogen production. AVEVA Process Simulation offers three configurations: Half Wave, Full Wave Bridge, and Ideal. The half wave rectifier, using a single diode, captures only half of the AC waveform, reaching a maximum efficiency of 40.5%. The full wave bridge, with four diodes, uses both halves of the waveform, achieving 81.1% efficiency for single-phase AC (Vattanapuripakorn et al. 2022). In Ideal mode, efficiency is assumed to be 100%. The software automatically accounts for these efficiencies and allows specifying a secondary efficiency to include additional losses.

Figure 3.9: Rectifier in AVEVA.

The transformer (Figure 3.10) model steps up or steps down voltage in electrical systems, for example, to increase voltage before transmission and reduce losses. In AVEVA Process Simulation, efficiency is calculated using a standard curve (Roy-

choudhury et al. 2014), which can be adjusted or replaced with a custom curve for each load fraction.

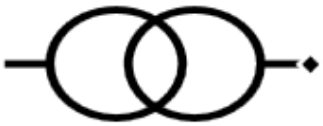

Figure 3.10: Transformer in AVEVA Process Simulation.

The busbar (Figure 3.11) model is used to split and combine currents in a simulation and supports simple voltage drop calculations. When multiple inputs are connected to the busbar, it is possible to choose either to balance the input voltages or to use the lowest input voltage. In this case, the voltages were balanced so that they operate at the same nominal voltage.

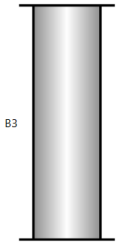

Figure 3.11: Busbar in AVEVA.

The consumer (Figure 3.12) model in AVEVA is used to represent additional electrical loads not directly modeled in the simulation, such as disturbances. However, in this case, the model was modified to represent a consumer load profile, not to export excess power, but to create a demand profile that must be supplied as a priority.

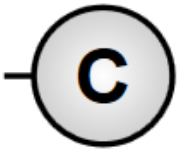

Figure 3.12: Consumer in AVEVA.

With this modification, the consumption profile shown in Figure 2.6 was added to the AVEVA model.

The Breaker (Figure 3.13) model is used to isolate sections of a grid by selectively connecting or disconnecting power flows. When the Breaker is connected, the total inlet power is passed to the outlet with no losses. When disconnected, no power flows through the Breaker.

Figure 3.13: Breaker in AVEVA.

Chapter 4

Two-layers MPC for energy management systems embedding neural network for forecasting renewable energy generation and demand

This chapter proposes a Model Predictive Control (MPC) framework for microgrid management, using Artificial Neural Networks (ANNs) to forecast renewable energy generation and load demand. These forecasts are integrated into a two-layer MPC strategy based on quadratic programming to optimize real-time control and address renewable source variability and demand uncertainty. A case study in Guanambi, Bahia (Brazil) demonstrates the method's effectiveness in improving energy efficiency and enabling green hydrogen production through electrolysis. The results highlight the potential of the MPC-ANN framework to drive sustainable energy transitions and industrial decarbonization in distributed energy systems.

The text included here is partially published in the Congresso Brasileiro de Engenharia Química:
CALHAU, F. A. S.; SANTOS, P. R. J.; MEIRA, R. L.; MARTINS, M. A. F. An MPC-based energy management system embedding neral networks for forecasting renewable energy generation and demand: a study on green hydrogen production. *Congresso Brasileiro de Engenharia Química*. Belo Horizonte: 2025.

4.1 Model Description

The proposed microgrid for analyzing the performance of the MPC-ANN is shown in Figure 4.1. This microgrid consists of a wind power plant, a solar power plant, a battery bank, access to the main grid, an electrolyzer, and hydrogen storage.

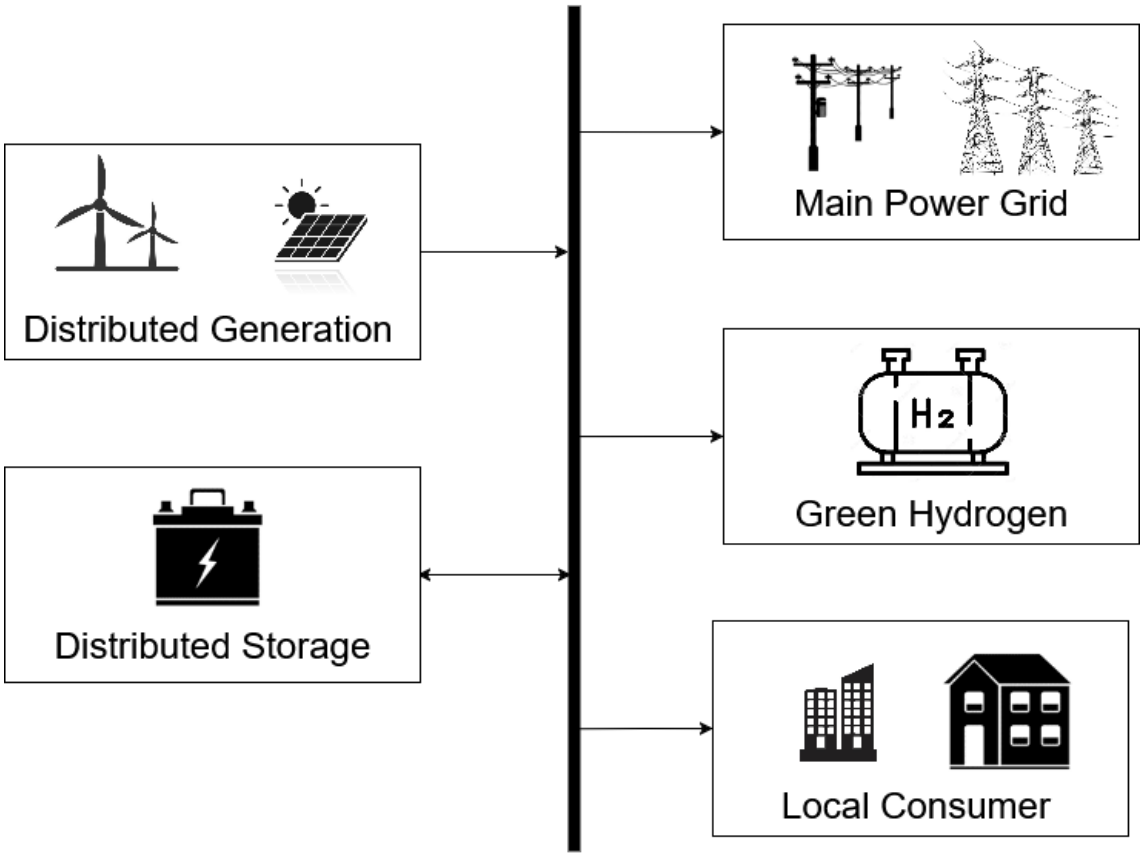

Figure 4.1: Architecture of a proposed microgrid.

To model the microgrid effectively, the concepts presented in Chapter 2 were applied, including Equation (2.4), Equation (2.9), and Equation (2.22). Accordingly,

$$\underbrace{\begin{bmatrix} SOC(k+1) \\ SHL(k+1) \end{bmatrix}}_{\mathbf{x}(k+1)} = \underbrace{\begin{bmatrix} 1 & 0 \\ 0 & 1 \end{bmatrix}}_{\mathbf{A}} \underbrace{\begin{bmatrix} SOC(k) \\ SHL(k) \end{bmatrix}}_{\mathbf{x}(k)} + \underbrace{\begin{bmatrix} \frac{T_s \eta_{bat}}{C_{bat}} & 0 & 0 \\ 0 & \frac{T_s \eta_{H_2}}{C_{H_2}} & 0 \end{bmatrix}}_{\mathbf{B}} \underbrace{\begin{bmatrix} P_{bat}(k) \\ P_{H_2}(k) \\ P_{grid}(k) \end{bmatrix}}_{\mathbf{u}(k)} \tag{4.1}$$

$$\underbrace{\begin{bmatrix}1 & 1 & 1\end{bmatrix}}_{\mathbf{D}_u}\underbrace{\begin{bmatrix}P_{bat}(k)\\P_{H_2}(k)\\P_{grid}(k)\end{bmatrix}}_{\mathbf{u}(k)}+\underbrace{\begin{bmatrix}1 & 1 & -1\end{bmatrix}}_{\mathbf{D}_d}+\underbrace{\begin{bmatrix}P_{solar}(k)\\P_{wind}(k)\\P_{load}(k)\end{bmatrix}}_{\mathbf{d}(k)}=0 \tag{4.2}$$

The state vector $\mathbf{x}(k) \in \mathbb{R}^{n_x}$ represents the energy levels of the storage components, which are influenced by the manipulated input $\mathbf{u}(k) \in \mathbb{R}^{n_u}$, comprising battery charging/discharging power (P_{bat}), hydrogen power exchange (P_{H_2}), and grid power transactions (P_{grid}). The disturbance vector $\mathbf{d}(k) \in \mathbb{R}^{n_d}$ accounts for exogenous inputs such as photovoltaic generation (P_{solar}), wind generation (P_{wind}), and consumer load demand (P_{load}). System dynamics are governed by matrices $\mathbf{A}$, $\mathbf{B}$, $\mathbf{C}$, $\mathbf{D}_u$, and $\mathbf{D}_d$ with appropriate dimensions. The model incorporates key parameters such as battery and hydrogen storage capacities (C_{bat} and C_{H_2}), charging/discharging efficiencies (η_{bat} and η_{H_2}), and the sampling period T_s.

4.2 Disturbance Modeling

As discussed in Chapter 2, the proposed LSTM model follows a Nonlinear Auto-Regressive (NAR) structure, as it generates predictions based solely on past values of the system's output. Operating in discrete time steps, the network produces one-step-ahead forecasts that are recursively fed back into the model to enable multi-step predictions. In this recursive forecasting scheme, each predicted output becomes part of the input for the subsequent step, requiring the internal states of the network to be updated iteratively to accurately capture the sequential dynamics of the system. This approach, which excludes exogenous inputs, aligns with the NAR paradigm as defined by Connor et al. (1994), and has been further developed in hybrid modeling contexts, such as in Zhang (2003).

Figures 5.5a, 5.5b and 5.6 shows 168 hours of prediction from the trained models. The performance of the ANN was assessed using the Root Mean Squared Error (RMSE), Mean Absolute Error (MAE), which measures the average magnitude of prediction errors.

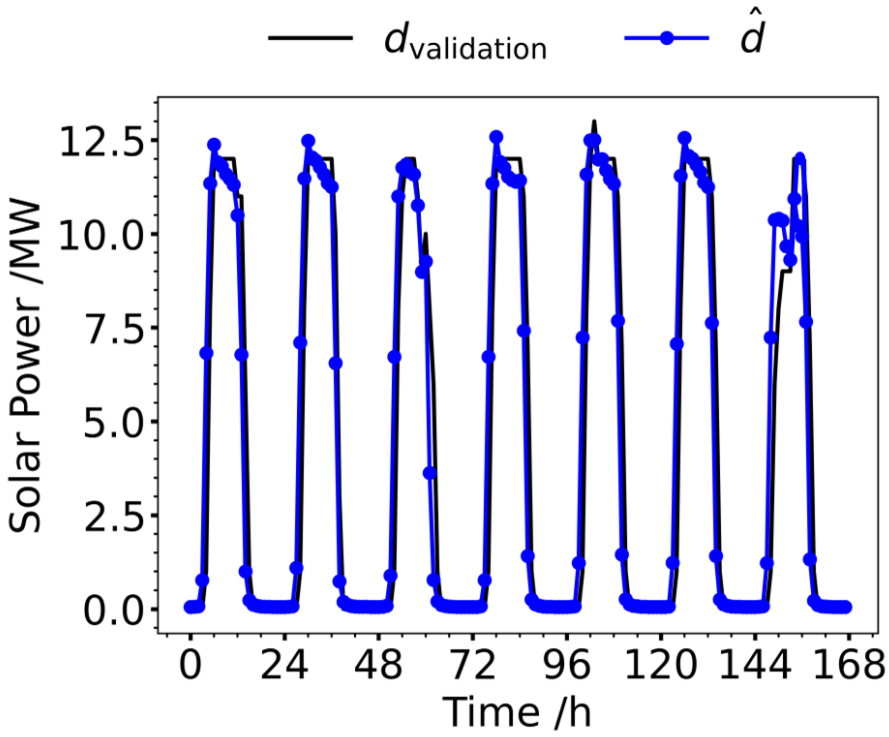

Figure 4.2: One week of solar power prediction over 168 h. $d_{validation}$ denotes the actual observed values in the test set, and $\hat{d}$ represents the predictions made by the artificial neural network.

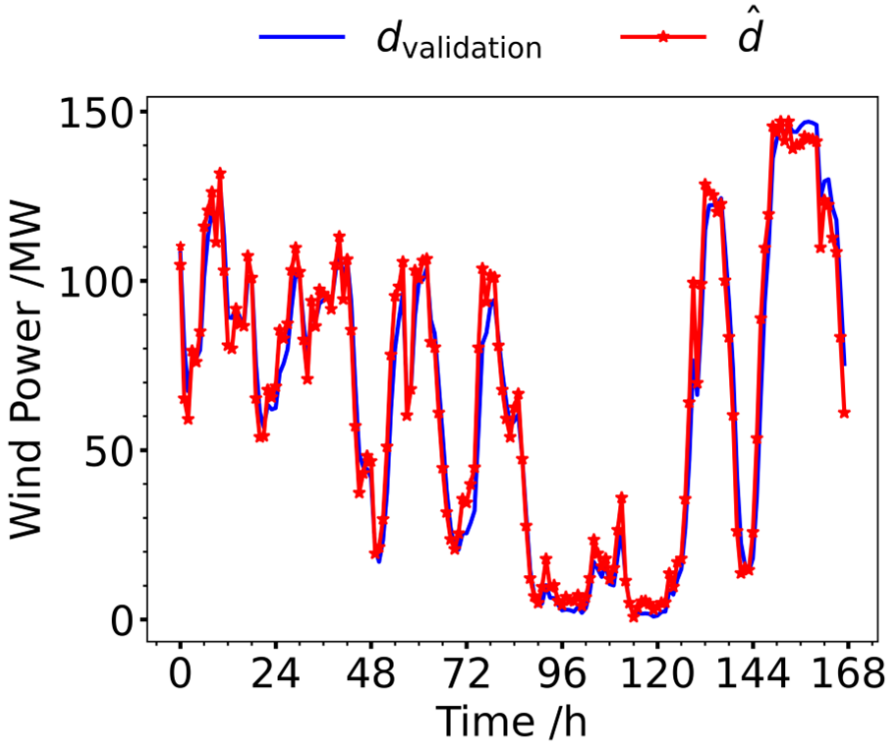

Figure 4.3: One week of wind power prediction over 168 h. $d_{validation}$ denotes the actual observed values in the test set, and $\hat{d}$ represents the predictions made by the artificial neural network.

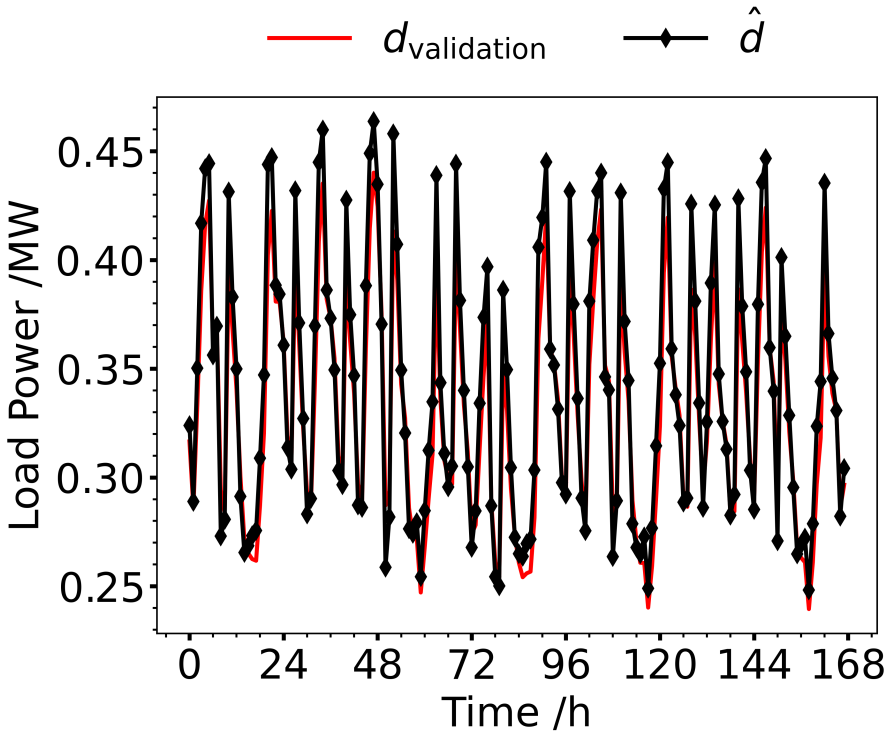

Figure 4.4: One week of load power prediction over 168 h. $d_{validation}$ denotes the actual observed values in the test set, and $\hat{d}$ represents the predictions made by the artificial neural network.

The forecasting performance for solar generation, wind generation, and load demand is summarized in Table 4.1.

Table 4.1: Prediction performance metrics for solar, wind, and load.

Variable	RMSE	MAE
Solar Generation	0.11	0.06
Wind Generation	0.13	0.09
Load Demand	0.11	0.09

For solar generation, the model achieved an RMSE of 0.11, and an MAE of 0.06 indicating strong accuracy and reliable variability representation. For wind, the RMSE of 0.13 and a MAE of 0.09 demonstrates excellent predictive performance with high correlation. For load, a low RMSE of 0.11 and an MAE of 0.09 reflects minimal absolute error, confirming the model's precision.

4.3 Controller Formulation

The economic cost function improves microgrid efficiency by minimizing energy purchases ℓ_{grid}, maximizing hydrogen production ℓ_{H_2}, and accounting for battery-related costs: cell replacement ℓ_{bat_1}, charge/discharge degradation ℓ_{bat_2}, state-of-charge variations ℓ_{bat_3}ensuring system performance and economic viability.

$$\begin{aligned}\ell_{eco}(x(k),u(k),p_e(k),p_{H_2}(k)) = &-\overbrace{p_e(k)T_s\lambda_1 P_{grid}(k)}^{\ell_{grid}} - \overbrace{p_{H_2}(k)T_s\lambda_2 P_{H_2}(k)}^{\ell_{H_2}} \\ &+ \overbrace{\frac{C_{re}T_s}{C_{Wh}}\lambda_3 P_{bat}(k)}^{\ell_{bat1}} + \overbrace{\lambda_4\frac{P_{bat}(k)}{V_{bat}I_{bat}}}^{\ell_{bat2}} \\ &+ \overbrace{\|x(k+1)-x(k)\|^2_{Q_{bat}}}^{\ell_{bat3}} \end{aligned} \tag{4.3}$$

The microgrid operation is optimized by balancing power sale (P_{grid}), hydrogen production (P_{H_2}), and battery charging/discharging (P_{bat}), with respective weights λ_1, λ_2, and λ_3. The model also includes the battery cell replacement cost (C_{re}) and the coefficient λ_4, considering battery voltage (V_{bat}), current (I_{bat}), hydrogen price (p_{H_2}), and electricity price (p_e) to minimize economic and operational impacts, ensuring efficient and cost-effective energy management.

The control law executed at time step k, with $\mathbf{x}(k)$ known, is given by:

$$\begin{aligned}\min_{\mathbf{u}_k,\mathbf{x}_s,\mathbf{u}_s} V_k = &\sum_{j=0}^{N-1} \|\mathbf{x}(k+j|k)-\mathbf{x}_s\|^2_{\mathbf{Q}} + \|\Delta\mathbf{u}(k+j|k)\|^2_{\mathbf{R}} \\ &+ \|\mathbf{u}(k+j|k)-\mathbf{u}_s\|^2_{\mathbf{Q}_s} + \|\mathbf{x}_s-\mathbf{x}_e\|^2_{\mathbf{Q}_x} + \|\mathbf{u}_s-\mathbf{u}_e\|^2_{\mathbf{Q}_u} \end{aligned} \tag{4.4}$$

Subject to:

$$\mathbf{x}(k+1|k) = \mathbf{A}\mathbf{x}(k) + \mathbf{B}\mathbf{u}(k) \tag{4.5}$$

$$\mathbf{x}_s = \mathbf{A}\mathbf{x}_s + \mathbf{B}\mathbf{u}_s \tag{4.6}$$

$$\mathbf{B}_u\mathbf{u}_s + \mathbf{B}_d\mathbf{d}(k) = 0 \tag{4.7}$$

$$\mathbf{B}_u\mathbf{u}(k) + \mathbf{B}_d\mathbf{d}(k) = 0 \tag{4.8}$$

$$\mathbf{d}(k+1|k) = \boldsymbol{f}(\mathbf{d}(k-n),\ldots,\mathbf{d}(k)) \tag{4.9}$$

$$\mathbf{x}(k+N|k) = \mathbf{x}_s \tag{4.10}$$

$$\mathbf{x} \in \mathbb{X}, \quad \mathbf{x}_s \in \mathbb{X} \tag{4.11}$$

$$\mathbf{u} \in \mathbb{U}, \quad \mathbf{u}_s \in \mathbb{U} \tag{4.12}$$

where $\mathbf{u}_k$ is the entire sequence of calculated optimal inputs, $\mathbf{u}_s$ and $\mathbf{x}_s$is the artificial reference point, representing the best steady-state-input pair the con trolled system can reach in N steps, at the current time. $\mathbf{Q}$, $\mathbf{Q}_x$ and $\mathbf{Q}_u$ are assumed to be positive semi-defined tuning matrices, while $\mathbf{R}$ are positive definite tuning matrices, each of appropriate dimensions.

Regarding constraints, (4.5) is the state of the process, (4.6) and (4.7) ensure that the artificial reference represents a system equilibrium point, (4.8) represents the power balance and (4.9) represent the prediction of future disturbance in at time $k+1$, $\boldsymbol{f}(\cdot)$ represents a trained artificial neural network that incorporates past values and current values of the disturbances, and (4.10) enforces a terminal equality constraint, requiring the predicted state to match the artificial reference at the end of the control horizon. Constraints (4.11) and (4.12) define bounds on states and inputs, with $\mathbb{X}$ and $\mathbb{U}$ as compact-convex sets for feasible regions.

$$\mathbb{X} = \{\mathbf{x} \in \mathbb{R}^{n_x} \mid \mathbf{x}_{\min} \leq \mathbf{x} \leq \mathbf{x}_{\max}\} \tag{4.13}$$

$$\mathbb{U} = \{\mathbf{u} \in \mathbb{R}^{n_u} \mid \mathbf{u}_{\min} \leq \mathbf{u} \leq \mathbf{u}_{\max}\} \tag{4.14}$$

The controller formulation requires prior knowledge of the economically optimal equilibrium point $(\mathbf{x}_e, \mathbf{u_e})$, determined by solving a static optimization problem in an economic steady-state target layer.

$$\min_{\mathbf{x}_e, \mathbf{u_e}} \ell_{eco} \tag{4.15}$$

$$\text{s.t:} \quad \mathbf{x}_e = \mathbf{A}\mathbf{x}_e + \mathbf{B}\mathbf{u}_e, \tag{4.16}$$

$$\mathbf{x_e} \in \mathbb{X}, \ \mathbf{u_e} \in \mathbb{U}. \tag{4.17}$$

4.4 Simulation and results

The simulation of the MPC-ANN proposed for the EMS of the industrial microgrid were solved using the CVXOPT framework (Andersen et al. 2020), implemented in Python 3.12. Table 4.2 summarizes the weighting matrices and the initial condition.

Table 4.2: Weighting matrices and the initial condition.

Parameters	Description	Value
$\mathbf{x}(0)$	Initial condition	$[50\ 35\ 20]^{\mathrm{T}}$ (%)
$\mathbf{u}(0)$	Initial condition	$[0\ -122\ 0]^{\mathrm{T}}$ (MW)
$\mathbf{u}_{\min}$	Minimum input	$[-100\ 0\ 0]^{\mathrm{T}}$(MW)
$\mathbf{u}_{\max}$	Maximum Input	$[100\ 50\ 30]^{\mathrm{T}}$(MW)
$\Delta\mathbf{u}$	Inputs increments	$[100\ 50\ 30]^{\mathrm{T}}$(MW)
η_{bat}	Battery efficiency	97%
η_{H_2}	Electrolyzer efficiency	74%
C_{bat}	Nominal power capacity of battery bank	800 MWh
C_{H2}	Maximum Volume	1200 Nm^3
T_s	Sampling period	1h
N	Horizon control	3
C_{re}	Replacement cost of the battery bank	\$325
C_{H_2}	Electrolyzer maintenance cost	\$500
C_{H_2}	Electrolyzer maintenance cost	\$400
$\mathbf{Q}$	Weighting matrix of the state,	diag(0.8, 0.05) MW
$\mathbf{R}$	Weighting matrix of the iputs increments	diag(0.1 1, 0.1) MW
$\mathbf{Q}_s$	Weighting matrix of the manipulated	diag(0.8, 0.05) MW
$\mathbf{Q}_x$	Weighting matrix of the artificial state	diag(0.8, 0.05) MW
$\mathbf{Q}_u$	Weighting matrix of the artificial output	diag(0.9, 0.01) MW

Remark 4.1 The weights $\mathbf{R}$, $\mathbf{Q}_u$, and $\mathbf{Q}_s$ for the NLP-based MPC and QP-based MPC are normalized by the maximum value of the corresponding variable to ensure compatibility with $\mathbf{Q}$.

In Figure 4.5, a block diagram of the proposed control loop for the residential microgrid is presented.

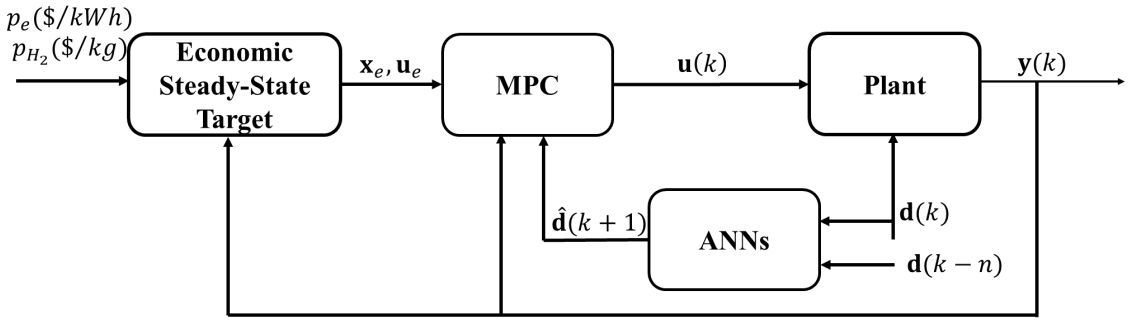

Figure 4.5: Block diagram of the EMS. p_e (\$/kWh) is the electricity price, p_{H_2} (\$/kg) is the hydrogen price, $\mathbf{x}_e$ and $\mathbf{u}_e$ are the economic steady-state vectors, $\mathbf{u}(k)$ is the control input, $\mathbf{y}(k)$ is the system output, $\mathbf{d}(k)$ is the disturbance, $\mathbf{d}(k-n)$ is the past information of the disturbances and $\hat{\mathbf{d}}(k+1)$ is the measured process disturbance.

As discussed in Chapter 2, wind and solar power generation, along with electrical demand, are considered external disturbances due to their stochastic and uncontrollable nature. Consequently, the artificial intelligence-based modeling techniques introduced in Chapter 2 are employed in this work. The disturbance profiles used in the simulations are shown in Figures 5.5a, 5.5b and 5.6.

Figure 4.6 represents the power exchange at the microgrid node and Figure 4.7 shows the battery storage of charge and storage hydrogen level.

Guanambi, located in the state of Bahia, Brazil, stands out as a key hub for renewable energy due to its favorable geographical and climatic conditions. The region benefits from strong wind currents predominantly during the early morning hours, while its semi-arid climate enables high solar irradiance throughout the day. Given that the installed wind power capacity exceeds that of solar, wind generation dominates the renewable energy mix. This complementary behavior between solar and wind resources enables the support of local demand, hydrogen production via electrolysis, energy storage in batteries, and surplus energy export to the Brazilian National System Operator (NSO). As such, Guanambi positions itself as a self-sufficient energy city and a potential hub for green hydrogen production.

Figures 4.7a and 4.7b illustrate the battery state of charge (SOC) and the hydrogen storage level (SHL), respectively. With initial values set to 50% for SOC and 35% for SHL, the integration of artificial neural networks (ANNs) enhances the microgrid's capability to plan hydrogen storage and energy trading. When hy-

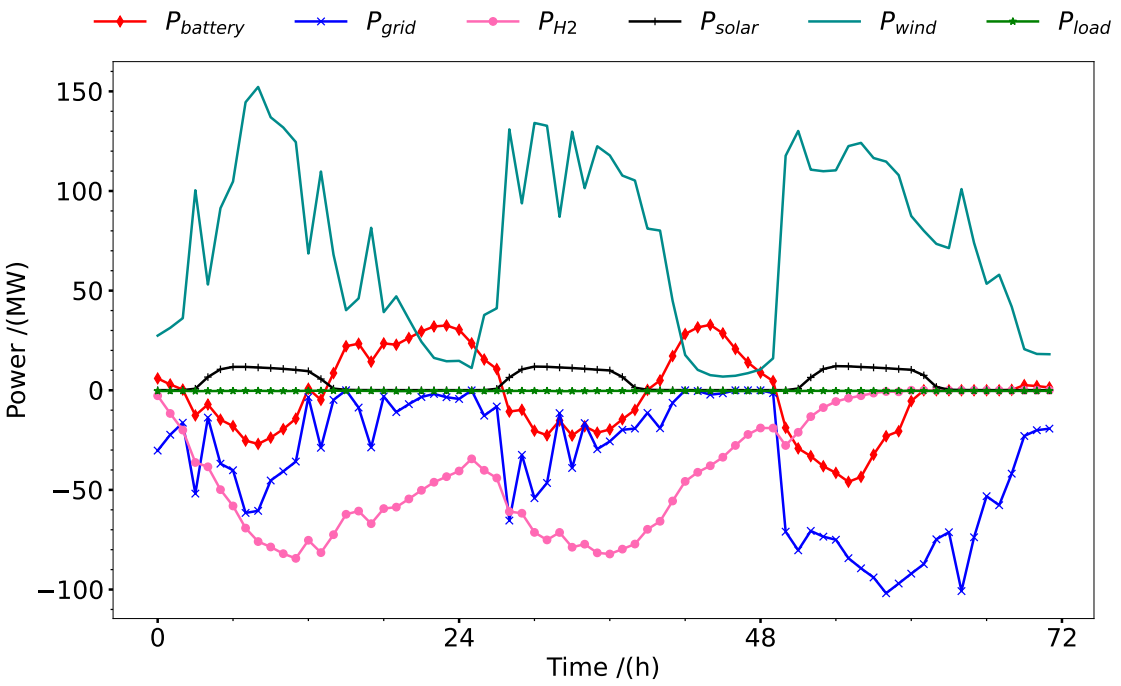

Figure 4.6: Manipulated variables and disturbances: $P_{battery}$ and $P_{H_2}$is battery and hydrogen power, respectively, P_{grid} is power sold to the grid, P_{solar} and P_{wind} is solar and wind generation, respectively, and P_{load} is demand power

drogen storage reaches full capacity and energy dispatch is maximized, the system autonomously redirects excess generation to the battery, ensuring optimal resource utilization and improving overall microgrid performance.

To manage such a dynamic energy environment, ANNs were embedded as a feed-forward mechanism within the predictive control architecture. In complex scenarios characterized by high variability in both generation and consumption, accurate disturbance forecasting is critical to achieving optimal control performance. ANNs are particularly suitable for this task, as they can learn complex nonlinear relationships from historical data, reducing the need for explicit physical modeling while enhancing system adaptability. Their ability to update in real time allows the controller to dynamically adjust to changing operating conditions, which is particularly advantageous in microgrids influenced by weather variability and user behavior. Figures 4.8, 4.9 and 4.10 present a comparative analysis of MPC performance with and without ANN integration.

In Figure 4.8, the proactive behavior of the controller in response to variations in energy generation is clearly observed. When facing either a surplus or deficit in

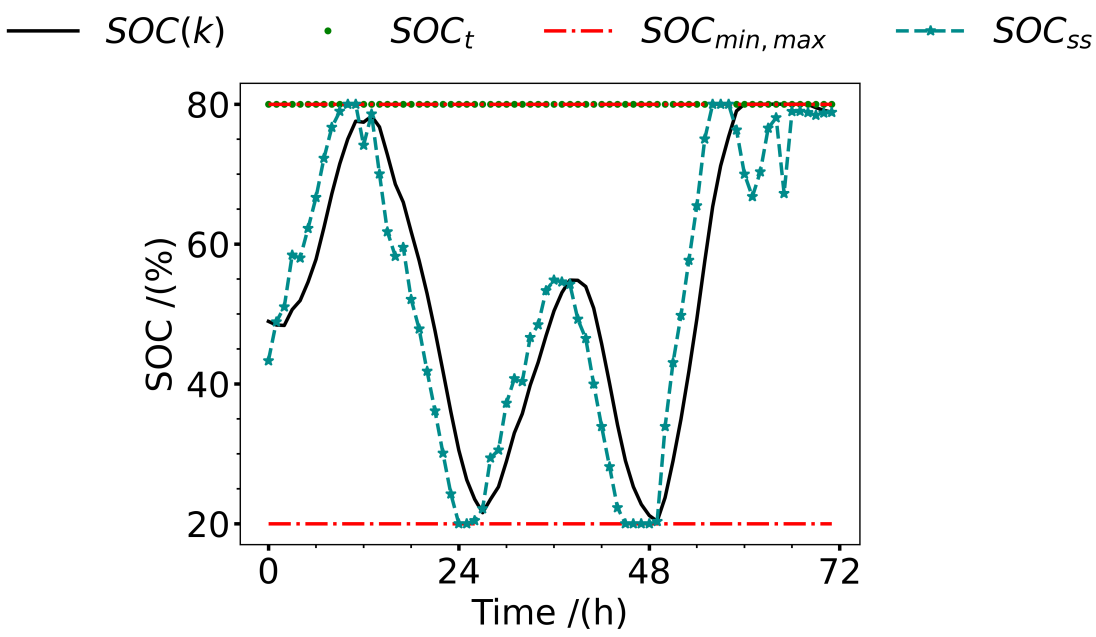

(a) Battery state of charge (SOC)

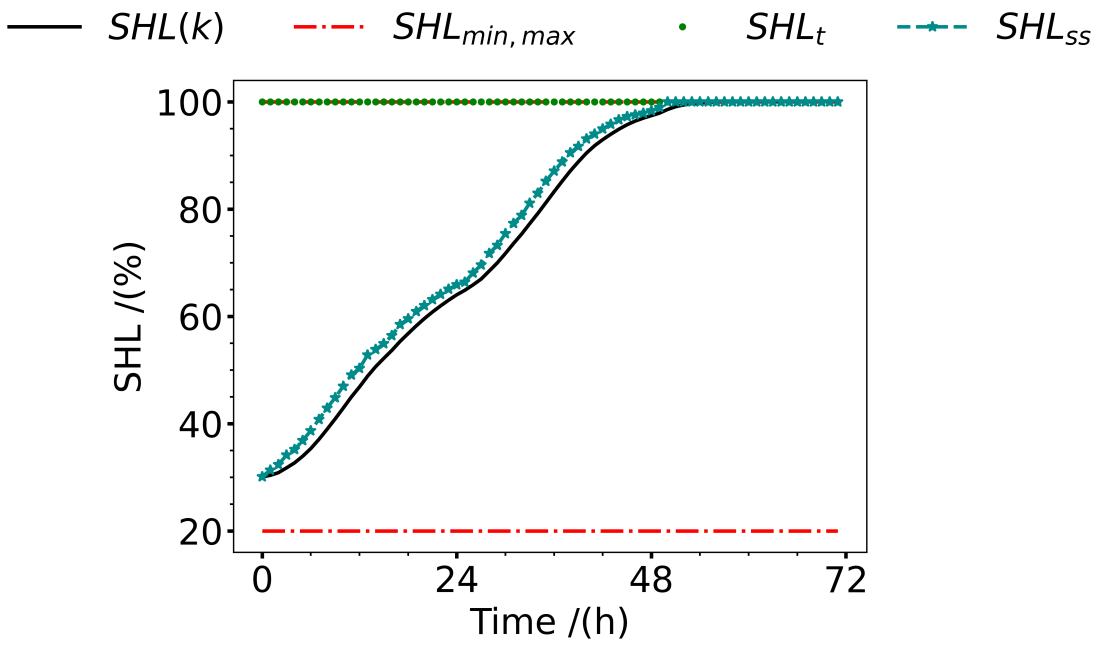

(b) Storage hydrogen level (SHL)

Figure 4.7: Battery state of charge (SOC) and storage hydrogen level (SHL). $SOC(k)$ and $SHL(k)$ denote the current levels; SOC_e and SHL_e, the economic operating points; $SOC_{\min/\max}$ and $SHL_{\min/\max}$, the operational constraints; and SOC_{ss} and SHL_{ss}, the artificial steady states

generation, the MPC, informed by forecasts from the neural network, anticipates its actions by strategically charging or discharging the battery. In certain scenarios, it chooses to maintain the current storage level, thereby minimizing control effort and

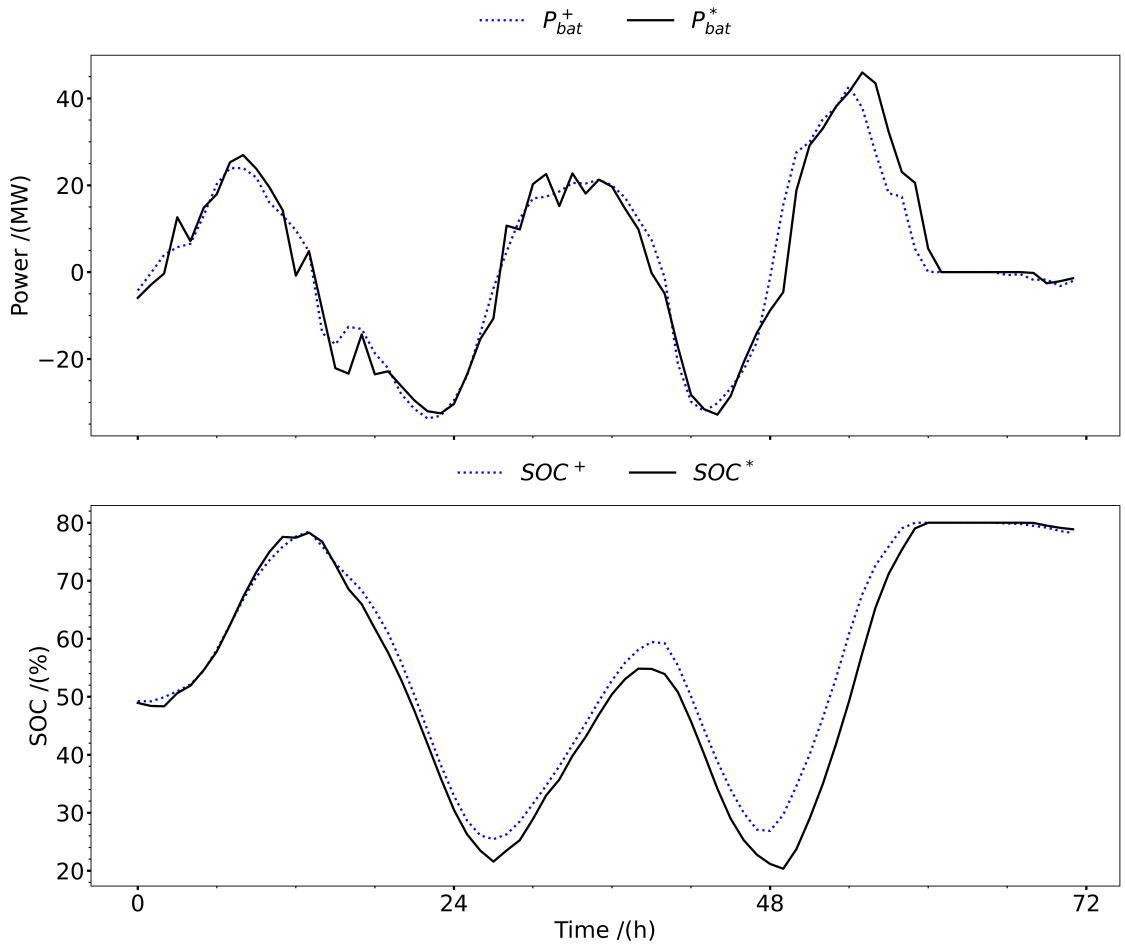

Figure 4.8: Comparison between using ANNs as a disturbance prediction model and without a prediction model for battery. The superscript (+) indicates the result obtained without the feedforward action and the superscript (*) indicates the result obtained with the ANN feedforward action.

avoiding unnecessary fluctuations. This behavior not only improves the system's energy efficiency but also reduces wear on storage devices.

Figure 4.9 presents a similar case, in which the controller anticipates decisions regarding hydrogen production. Based on forecasted operating conditions, the system is able to plan hydrogen generation in advance, optimizing resource utilization and minimizing the required control effort. This anticipatory capability highlights the importance of real-time planning and supports intelligent asset management, enhancing system reliability and extending equipment lifespan.

Finally, Figure 4.10 illustrates the controller's ability to identify, ahead of time, opportunities for exporting surplus energy to the electrical grid. Whenever energy is available and market conditions are favorable, the MPC enables efficient energy

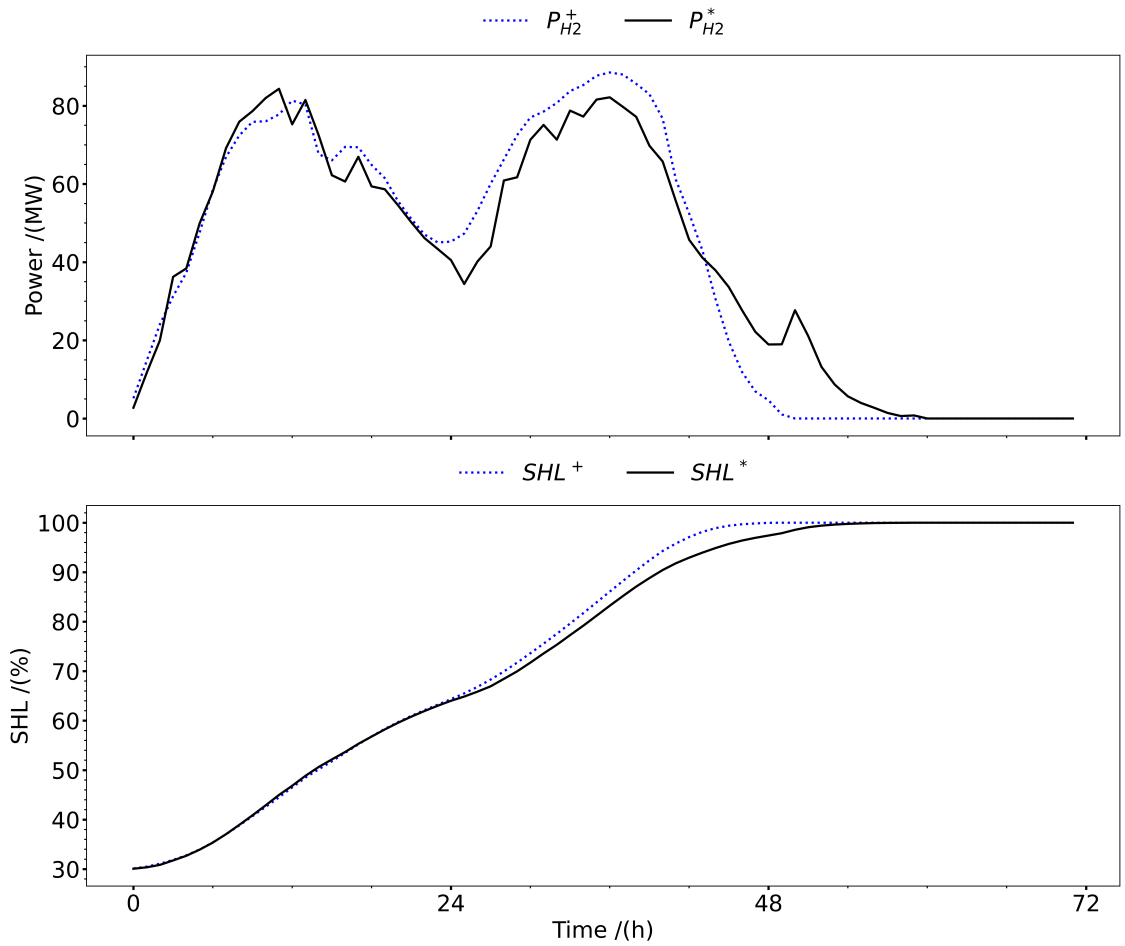

Figure 4.9: Comparison between using ANNs as a disturbance prediction model and without a prediction model for hydrogen. The superscript (+) indicates the result obtained without the feedforward action and the superscript (*) indicates the result obtained with the ANN feedforward action.

export, thereby maximizing revenues from energy sales. This behavior demonstrates not only the adaptive capacity of the control system but also its alignment with economic optimization objectives.

Overall, the integration of artificial neural networks with model predictive control significantly enhances the system's ability to operate predictively, robustly, and economically. By anticipating critical decisions based on reliable forecasts, the controller contributes to a more sustainable and resilient performance, aligned with the principles of energy efficiency and optimal resource management in modern microgrids.

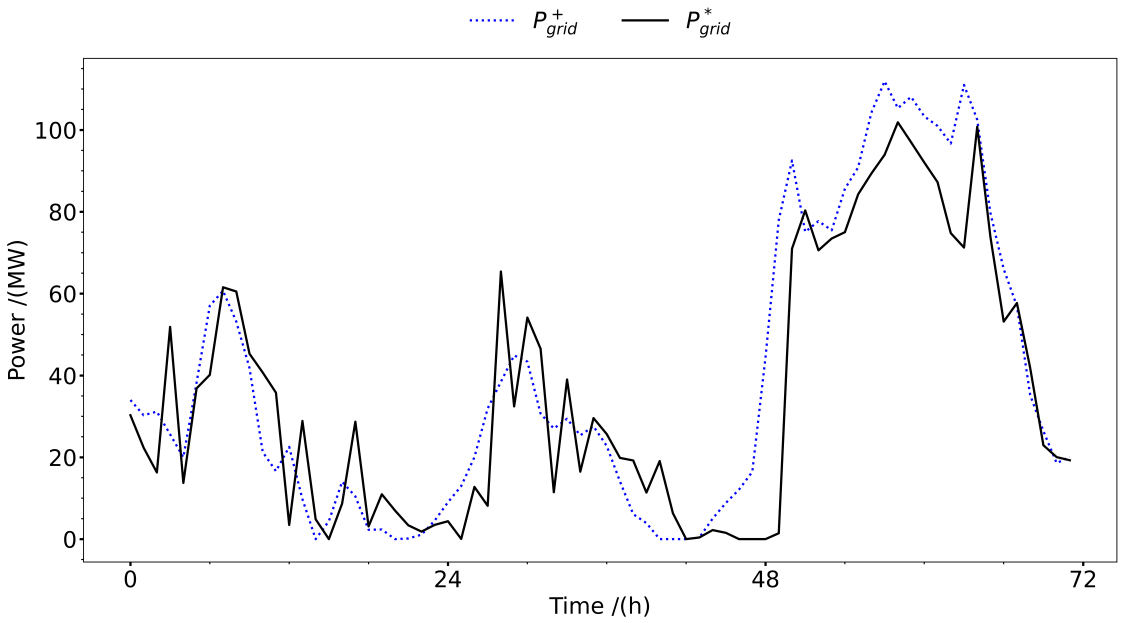

Figure 4.10: Comparison between using ANNs as a disturbance prediction model and without a prediction model for grid.The superscript (+) indicates the result obtained without the feedforward action and the superscript (*) indicates the result obtained with the ANN feedforward action.

4.5 Conclusion

In this chapter, a novel integration of Model Predictive Control (MPC) with disturbance modeling using Artificial Neural Networks (ANNs) is proposed, resulting in a unified MPC-ANN framework. This approach aims to enhance the predictive performance of Energy Management Systems (EMS) in microgrids, particularly under the operational challenges imposed by the intermittency of renewable energy sources and the pursuit of sustainable green hydrogen production. By embedding ANN-based forecasting models for exogenous variables – such as photovoltaic and wind generation, as well as electrical load demand – the control strategy becomes more anticipative and precise, enabling real-time adaptation to system dynamics and optimal energy resource allocation.

The adoption of a Quadratic Programming (QP) formulation, as introduced in Chapter 3, endows the proposed MPC scheme with computational efficiency and numerical robustness, ensuring the capability to handle multivariable interactions and complex operational constraints within real-time execution requirements. This feature significantly enhances the applicability of the control strategy to industrial-scale microgrid systems.

The synergistic integration of ANN-based forecasting with QP-based MPC constitutes an advanced and robust methodology for hierarchical microgrid control. It fosters more efficient, secure, and sustainable energy management practices, supporting the broader goals of energy transition, decarbonization, and intelligent grid operation.

Chapter 5

Single-layer zone-based MPC for energy management systems embedding artificial neural network for forecasting renewable energy generation and demand

This chapter develops a single-layer, zone-based Model Predictive Control (MPC) framework that leverages Quadratic Programming and AI-driven disturbance forecasts to streamline microgrid operation. By employing a unified state-space representation, the controller solves a single quadratic optimization problem across the entire prediction horizon, thereby reducing computational overhead and simplifying implementation. Crucially, a formal stability proof – based on treating the MPC's optimal cost as a Lyapunov candidate – demonstrates that, under mild assumptions and via recursive feasibility, the closed-loop cost is nonincreasing, which guarantees convergence to the economic equilibrium. Simulation results show that the approach reliably achieves economic optimality under varying setpoints, while neural network forecasts enhance both robustness and prediction accuracy. Furthermore, sensitivity analyses confirm the method's ability to maintain performance in the face of load spikes and renewable generation fluctuations. Overall, this integration of predictive control, stability guarantees, and machine learning establishes a cohesive and scalable solution for efficient, cost-effective, and resilient microgrid energy management.

This manuscript is in the submission process.

CALHAU, F. A. S.; SANTOS, P. R. J; BISPO, H.; MEIRA, R. L.; MARTINS, M. A. F. Single-layer zone-based MPC for energy management systems embedding artificial neural network for forecasting renewable energy generation and demand.

5.1 Controller Formulation

Figure 5.1 presents a architecture of a microgrid consists of a solar power plant, a battery bank, access to the main grid.

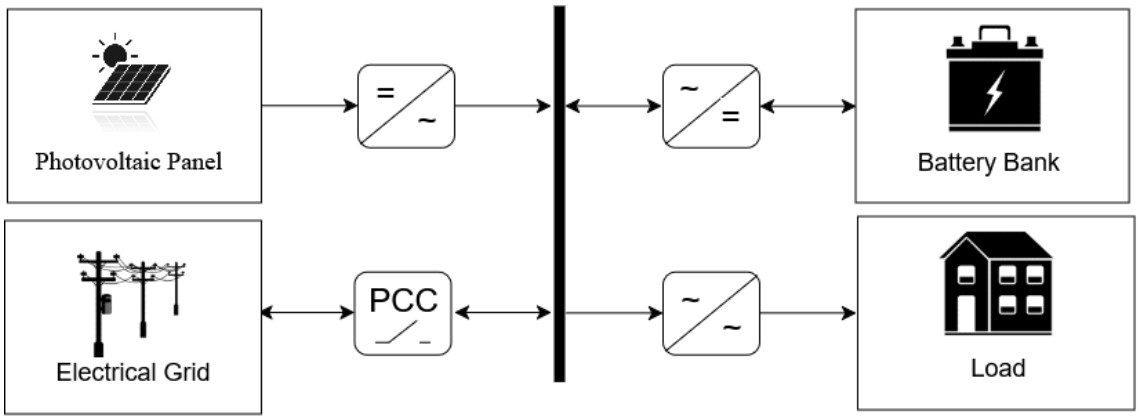

Figure 5.1: Microgrid architecture.

To construct an accurate microgrid model, the concepts introduced in Chapter 2 – specifically Equations (2.4), and (2.22) – are employed. Accordingly, the standard discrete-time state-space representation is given by:

$$\underbrace{\begin{bmatrix} SOC(k+1) \end{bmatrix}}_{\mathbf{x}(k+1)} = \underbrace{\begin{bmatrix} 1 \end{bmatrix}}_{\mathbf{A}} \underbrace{\begin{bmatrix} SOC(k) \end{bmatrix}}_{\mathbf{x}(k)} + \underbrace{\begin{bmatrix} \frac{T_s \eta_{bat}}{C_{bat}} & 0 \end{bmatrix}}_{\mathbf{B}} \underbrace{\begin{bmatrix} P_{bat}(k) \\ P_{grid}(k) \end{bmatrix}}_{\mathbf{u}(k)} \tag{5.1}$$

$$\underbrace{\begin{bmatrix} 1 & 1 \end{bmatrix}}_{\mathbf{D}_u} \underbrace{\begin{bmatrix} P_{bat}(k) \\ P_{grid}(k) \end{bmatrix}}_{\mathbf{u}(k)} + \underbrace{\begin{bmatrix} 1 & -1 \end{bmatrix}}_{\mathbf{D}_d} + \underbrace{\begin{bmatrix} P_{solar}(k) \\ P_{load}(k) \end{bmatrix}}_{\mathbf{d}(k)} = 0 \tag{5.2}$$

where SOC denotes the battery state of charge. The terms P_{bat} represent the power exchanged by the battery, and P_{grid} is the power exchanged with the main grid, P_{solar} the photovoltaic generation and P_{load} the load demand.

Although Equation (5.2) is typically imposed as a constraint in the optimization problem, in this work it is incorporated directly into the objective to maximize the microgrid's operational benefit. Consequently, Equation (5.2) can be rewritten as follows:

$$P_{grid} = P_{solar} + P_{bat} - P_{load} \tag{5.3}$$

With this modification, the power exchanged with the main grid is no longer treated as a manipulated variable but rather as a controlled variable. Accordingly, the state-space representation is updated as follows:

$$\underbrace{\Big[SOC(k+1)\Big]}_{\mathbf{x}(k+1)} = \underbrace{\Big[1\Big]}_{\mathbf{A}} \underbrace{\Big[SOC(k)\Big]}_{\mathbf{x}(k)} + \underbrace{\left[\frac{T_s \eta_{bat}}{C_{bat}}\right]}_{\mathbf{B}} \underbrace{\Big[P_{bat}(k)\Big]}_{\mathbf{u}(k)} \tag{5.4}$$

$$\underbrace{\begin{bmatrix} SOC(k) \\ P_{grid}(k) \end{bmatrix}}_{\mathbf{y}(k)} = \underbrace{\begin{bmatrix} 1 \\ 0 \end{bmatrix}}_{\mathbf{C}} \underbrace{\Big[SOC(k)\Big]}_{\mathbf{x}(k)} + \underbrace{\begin{bmatrix} 0 \\ 1 \end{bmatrix}}_{\mathbf{D}_u} \underbrace{\Big[P_{bat}(k)\Big]}_{\mathbf{u}(k)} + \underbrace{\begin{bmatrix} 0 & 0 \\ 1 & -1 \end{bmatrix}}_{\mathbf{D}_d} \underbrace{\begin{bmatrix} P_{solar}(k) \\ P_{load}(k) \end{bmatrix}}_{\mathbf{d}(k)} \tag{5.5}$$

Therefore, Equation (5.4) captures the storage system's state dynamics, while Equation (5.5) defines the controlled outputs. In this formulation, the state vector $\mathbf{x}(k) \in \mathbb{R}^{n_x}$ represents storage levels, and the input vector $\mathbf{u}(k) \in \mathbb{R}^{n_u}$ corresponds to storage power as the manipulated variable. The output vector $\mathbf{y}(k) \in \mathbb{R}^{n_y}$ comprises grid power and storage dynamics, whereas the disturbance vector $\mathbf{d}(k) \in \mathbb{R}^{n_d}$ includes photovoltaic generation, wind power, and load demand. System evolution is governed by the matrices $\mathbf{A}$, $\mathbf{B}$, $\mathbf{C}$, $\mathbf{D}_u$, and $\mathbf{D}_d$.

With the model defined, the proposed zone-based MPC is formulated using the following quadratic cost function:

$$\begin{aligned} V_{\mathrm{k}} =& (P_{grid} - P_{grid,sp})^{\mathrm{T}} \rho_e (P_{grid} - P_{grid,sp}) \\ &+ (SOC - SOC_{sp})^{\mathrm{T}} \frac{C_{re}}{C_{bat,cel}} (SOC - SOC_{sp}) \qquad (5.6) \\ &+ \Delta P_{bat}^{\mathrm{T}} \frac{\rho_e}{\eta_{bat}} \Delta P_{bat}, \qquad (5.7) \end{aligned}$$

where the subscript sp is the set-point, ρ_e is the electrical priceη_{bat} is the battery efficiency, C_{re} is the cost of replacement the storage system, $C_{bat,cel}$ is the nominal power capacity.

Finally, the control law of the QP-based zone-MPC proposed here can be generalized and formulated as the solution to the following optimization problem:

Problem 0

$$\min_{\mathbf{u}_k, \mathbf{y}_{sp,k}} V_{\mathrm{k}},$$

$$V_{\mathrm{k}} = \sum_{j=0}^{N-1} \|\mathbf{y}(k+j|k) - \mathbf{y}_{sp,k}\|_{\mathbf{Q}}^2 + \|\Delta\mathbf{u}(k+j|k)\|_{\mathbf{R}}^2 \,, \tag{5.8}$$

subject to (5.4), (5.5) and:

$$\mathbf{y}(k+N|k) = \mathbf{y}_{\mathrm{sp},k} \tag{5.9}$$

$$\mathbf{y}_{\min} \leq \mathbf{y}_{\mathrm{sp},k} \leq \mathbf{y}_{\max} \tag{5.10}$$

$$\Delta\mathbf{u}_{\min} \leq \Delta\mathbf{u}(k+j|k) \leq \Delta\mathbf{u}_{\max} \tag{5.11}$$

$$\mathbf{u}_{\min} \leq \mathbf{u}(k+j|k) + \sum_{i=0}^{j} \Delta\mathbf{u}(k+i|k) \leq \mathbf{u}_{\max} \tag{5.12}$$

where $\mathbf{u}_k = [\mathbf{u}(k|k), \ldots, \mathbf{u}(k+N-1|k)]^{\mathrm{T}}$ is the entire sequence of calculated optimal inputs, (5.9) imposes a terminal equality constraint that enforces the predicted state to coincide with the reference output vector at the end of the control horizon – this terminal constraint is crucial for the Lyapunov-based stability proof, as it ensures recursive feasibility and nonincreasing cost, thereby guaranteeing closed-loop convergence, (5.10) is the zone of operation of the optimal outputs, (5.11) defines the maximum and minimum input limits, (5.12) defines hard limits on each control variable over the prediction horizon. $\mathbf{Q} \in \mathbb{R}^{ny \times ny}$ is a positive definite weighting matrix of the controlled outputs, $\mathbf{R} \in \mathbb{R}^{nu \times nu}$ are positive semi-definite weighting matrices of the input moves, $\mathbf{y}(k+j|k)$ is the output prediction vector at time step $k+j$ computed at time step k; $\mathbf{y}_{sp,k}$ is the output reference vector; $\Delta\mathbf{u}(k+j|k)$ is the trend vector of the input moves, where $\Delta\mathbf{u}(k+j|k) = \mathbf{u}(k|k) - \mathbf{u}(k-1|k)$ and $\Delta\mathbf{u}(k+j|k) = 0$, for $j \geq N$, where N is the control horizon.

Here, $\mathbf{Q}$ penalizes deviations of grid power and battery SOC from their setpoints, using the electricity price ρ_e for the grid power term and a replacement cost weight $C_{\mathrm{re}}/C_{\mathrm{bat,cel}}$ for SOC. The input-weight $\mathbf{R}$ penalizes changes in the battery power command, scaled by the energy price and the battery efficiency, discouraging aggressive control moves and costly cycling.

5.1.1 Stabilizing proof

To demonstrate the stabilizing behavior of the proposed controller in Problem 0, an undisturbed scenario is considered along with two conditions that must be satisfied: (i) recursive feasibility and (ii) optimality.

Condition I (Recursive Feasibility): Assume that Problem 0 provides an optimal solution at time step k, namely $\mathbf{y}^*_{sp,k}$ and $\mathbf{u}^*_k$,

$$\mathbf{u}^*_k = \begin{bmatrix}\mathbf{u}^*(k|k)^{\mathrm{T}} & \mathbf{u}^*(k+1|k)^{\mathrm{T}} \dots \mathbf{u}^*(k+N-1|k)^{\mathrm{T}}\end{bmatrix}. \tag{5.13}$$

As we know that $\mathbf{u}(k+N+j|k) = \mathbf{u}^*(k+N-1|k), \forall j \geq 0$, and since the first action control $\mathbf{u}^*(k|k)$ is implemented into the plant, the recursive feasibility is proved if the warm start solution at time step $k+1$ (solution inherited from time step k, described in (5.14)) meets all constraints.

$$\tilde{\mathbf{u}}_{k+1} = \begin{bmatrix}\mathbf{u}^*(k+1|k)^{\mathrm{T}} & \mathbf{u}^*(k+2|k)^{\mathrm{T}} \dots & \mathbf{u}^*(k+N-1|k)^{\mathrm{T}} & \mathbf{u}^*(k+N-1|k)^{\mathrm{T}}\end{bmatrix}^{\mathrm{T}}. \tag{5.14}$$

It is trivial to verify that (5.14) meets the constraints (5.11) and (5.12).

Based on model (5.5), the output prediction at the end of the control horizon at instant k is given by:

$$\mathbf{y}(k+N|k) = \mathbf{C}\mathbf{x}(k+N|k) + \mathbf{D_u}\mathbf{u}(k+N|k) + \mathbf{D_d}\mathbf{d}(k+N|k) \tag{5.15}$$

As mentioned above, since MPC optimizes the control sequence up to $\mathbf{u}(k+N-1|k)$, the control action is held constant beyond the control horizon. Consequently, the prediction at time step $k+N$ can be rewritten as

$$\mathbf{y}(k+N|k) = \mathbf{C}\mathbf{x}(k+N|k) + \mathbf{D_u}\mathbf{u}^*(k+N-1|k) + \mathbf{D_d}\mathbf{d}(k+N|k) \tag{5.16}$$

In order to meet constraint (5.9), it follows that:

$$\mathbf{y}(k+N|k) = \mathbf{y}^*_{sp,k} \tag{5.17}$$

$$\begin{aligned}&\mathbf{C}\mathbf{x}(k+N|k) + \mathbf{D_u}\mathbf{u}^*(k+N-1|k) + \mathbf{D_d}\mathbf{d}(k+N|k) = \mathbf{C}\mathbf{x}^*_{sp,k} \\ &+ \mathbf{D_u}\mathbf{u}^*(k+N-1|k) + \mathbf{D_d}\mathbf{d}(k+N|k)\end{aligned} \tag{5.18}$$

This implies that $\mathbf{x}(k+N|k) = \mathbf{x}^*_{sp,k}$.

It is worth mentioning that at time step k:

$$\begin{aligned}\mathbf{x}(k+N|k) =&\mathbf{A}^N\mathbf{x}(k|k) + \mathbf{A}^{N-1}\mathbf{B}\mathbf{u}^*(k|k) + \cdots + \mathbf{A}\mathbf{B}\mathbf{u}^*(k+N-2|k)\\ &+\mathbf{B}\mathbf{u}^*(k+N-1|k),\end{aligned} \tag{5.19}$$

and, for notational convenience, let us consider the matrix form where $\Theta_N = [\mathbf{A}^{N-1}\mathbf{B}\cdots\mathbf{A}\mathbf{B}\ \ \mathbf{B}]$. We obtain,

$$\mathbf{x}(k+N|k) = \mathbf{A}^N\mathbf{x}(k|k) + \Theta_N\mathbf{u}_k^* \tag{5.20}$$

At time instant $k+1$, considering the solution inherited from k, it follows that:

$$\tilde{\mathbf{x}}(k+N+1|k+1) = \mathbf{A}^N\mathbf{x}(k+1|k+1) + \Theta_N\tilde{\mathbf{u}}_{k+1} \tag{5.21}$$

For a nominal system, the actual states coincide with the model prediction, that is, $\mathbf{x}(k+1|k+1) = \mathbf{x}(k+1|k)$, leading to $\mathbf{x}(k+1|k+1) = \mathbf{A}\mathbf{x}(k) + \mathbf{B}\mathbf{u}^*(k|k)$. Consequently,

$$\begin{aligned}\tilde{\mathbf{x}}(k+N+1|k+1) &= \mathbf{A}^N(\mathbf{A}\mathbf{x}(k) + \mathbf{B}\mathbf{u}^*(k|k)) + \Theta_N\tilde{\mathbf{u}}_{k+1},\\ \tilde{\mathbf{x}}(k+N+1|k+1) &= \mathbf{A}^{N+1}\mathbf{x}(k) + \mathbf{A}^N\mathbf{B}\mathbf{u}^*(k|k) + \Theta_N\tilde{\mathbf{u}}_{k+1}.\end{aligned} \tag{5.22}$$

Rearranging the terms yields:

$$\begin{aligned}\tilde{\mathbf{x}}(k+N+1|k+1) &= \mathbf{A}(\mathbf{A}^N\mathbf{x}(k) + \mathbf{A}^{N-1}\mathbf{B}\mathbf{u}^*(k|k) + \Theta_N\tilde{\mathbf{u}}_{k+1})\\ \tilde{\mathbf{x}}(k+N+1|k+1) &= \mathbf{A}(\mathbf{A}^N\mathbf{x}(k) + \mathbf{A}^{N-1}\mathbf{B}\mathbf{u}^*(k|k) + \Theta_N\tilde{\mathbf{u}}_{k+1})\\ \tilde{\mathbf{x}}(k+N+1|k+1) &= \mathbf{A}(\underbrace{\mathbf{A}^N\mathbf{x}(k) + \Theta_N\mathbf{u}_k^*}_{\mathbf{x}(k+N|k)}) + \mathbf{B}\mathbf{u}^*(k+N-1|k)\\ \tilde{\mathbf{x}}(k+N+1|k+1) &= \mathbf{A}\mathbf{x}(k+N|k) + \mathbf{B}\mathbf{u}^*(k+N-1|k)\end{aligned} \tag{5.23}$$

In light of this, we can proceed to evaluate the outputs at the end of the control horizon, in symbols:

$$\begin{aligned}\tilde{\mathbf{y}}(k+N+1|k+1) &= \mathbf{C}\mathbf{x}(k+N+1|k+1) + \mathbf{D}_u\mathbf{u}^*(k+N-1|k) + \mathbf{D}_d\mathbf{d}(k+N|k)\\ &= \mathbf{C}\Big(\mathbf{A}\mathbf{x}(k+N|k) + \mathbf{B}\mathbf{u}^*(k+N-1|k)\Big)\\ &\quad + \mathbf{D}_u\mathbf{u}^*(k+N-1|k) + \mathbf{D}_d\mathbf{d}(k+N|k)\end{aligned} \tag{5.24}$$

Moreover, evaluating $\tilde{\mathbf{y}}_{sp,k+1}$, one obtains that

$$\tilde{\mathbf{y}}_{sp,k+1} = \mathbf{C}\tilde{\mathbf{x}}_{sp,k+1} + \mathbf{D}_u\mathbf{u}^*(k+N-1|k) + \mathbf{D}_d\mathbf{d}(k+N|k)$$

$$= \mathbf{CAx}^*_{sp,k} + \mathbf{CBu}^*(k+N-1|k) + \mathbf{D}_u\mathbf{u}^*(k+N-1|k) + \mathbf{D}_d\mathbf{d}(k+N|k) \tag{5.25}$$

Subtracting (5.24) and (5.25), it turns out to be:

$$\mathbf{CA}(\mathbf{x}(k+N|k) - \mathbf{x}^*_{sp,k}) = 0, \tag{5.26}$$

which implies that the solution inherited, given by (5.14), satisfies the terminal constraint (5.9) at time k+1, with $\tilde{\mathbf{y}}_{sp,k+1} = \mathbf{y}^*_{sp,k}$, thereby ensuring that all constraints in Problem 0 remain satisfied. Therefore, the solution inherited from time step k fulfills all the requirements of Problem 0, which establishes recursive feasibility.

Condition II (Optimality): The second part of the stability proof is related to the asymptotic convergence of the objective function. Therefore, it is necessary to show that the objective function is asymptotically decreasing. To do this, consider the optimal solution in the function V_k, as being

$$V_k = \sum_{j=0}^{N-1} \left\|\mathbf{y}(k+j|k) - \mathbf{y}^*_{sp,k}\right\|^2_{\mathbf{Q}} + \|\Delta\mathbf{u}^*(k+j|k)\|^2_{\mathbf{R}}\,, \tag{5.27}$$

whereas the objective function at k+1 for the solution inherited from instant k, becomes:

$$\tilde{V}_{k+1} = \sum_{j=0}^{N-1} \|\mathbf{y}(k+1+j|k+1) - \tilde{\mathbf{y}}_{sp,k+1}\|^2_{\mathbf{Q}} + \|\Delta\tilde{\mathbf{u}}(k+1+j|k+1)\|^2_{\mathbf{R}}\,, \tag{5.28}$$

The difference between these two cost, (5.27) and (5.28), values can be expressed as:

$$V^*_k - \tilde{V}_{k+1} = \|\mathbf{y}(k|k) - \mathbf{y}^*_{sp,k}\|^2_{\mathbf{Q}} + \|\Delta\mathbf{u}^*(k|k)\|^2_{\mathbf{R}}. \tag{5.29}$$

Since the weighting matrices $\mathbf{Q}$ and $\mathbf{R}$ are positive definite, respectively, both quadratic terms on the right-hand side of (5.29) are nonnegative, by optimally, $\tilde{V}_{k+1} \leq V^*_{k+1}$, which implies in $\tilde{V}_{k+1} \leq V^*_k$. Therefore, the optimal cost function V^*_k is monotonically non-increasing along the closed-loop trajectories of the system. □

5.1.2 Numerical example

To analyze and illustrate the results of the stability proof presented in Stabilizing proof, a scenario was defined in which the disturbances, namely solar generation and

Table 5.1: Numerical example zone definitions.

Time /(h)	$\mathbf{d}(k)/(\text{kW})$	$\mathbf{y}_{\min}^{\mathrm{T}}$	$\mathbf{y}_{\max}^{\mathrm{T}}$
0 to 23	[0.1 0.5]	[20% − 0.5 kW]	[60% − 0.5 kW]
24 to 47	[0.1 0.5]	[20% − 0.6 kW]	[60% − 0.6 kW]
48 to 71	[1.5 0.5]	[20% − 1 kW]	[60% − 1 kW]
72 to 95	[0.5 0.6]	[20% 0.2 kW]	[60% 0.2 kW]
96 to 119	[0.4 0.7]	[20% 0.3 kW]	[60% 0.3 kW]
120 to 144	[0.1 0.5]	[20% − 0.5 kW]	[60% − 0.5 kW]

consumption, are assumed to remain constant over the entire prediction horizon. Accordingly, the structure presented in Table 5.1 was defined.

As observed, the SOC operating range was assumed to be constant across the entire prediction horizon. Regarding P_{grid}, both the lower and upper bounds were collapsed to directly define the setpoint. This approach enables the specification of energy exchange targets with the main grid, based on the surplus or deficit of energy produced by the solar source.

Figure 5.2a illustrates the power exchange with the main grid, while Figure 5.2b depicts the power flow at the microgrid node. The battery state of charge (SOC) is shown in Figure 5.2c.

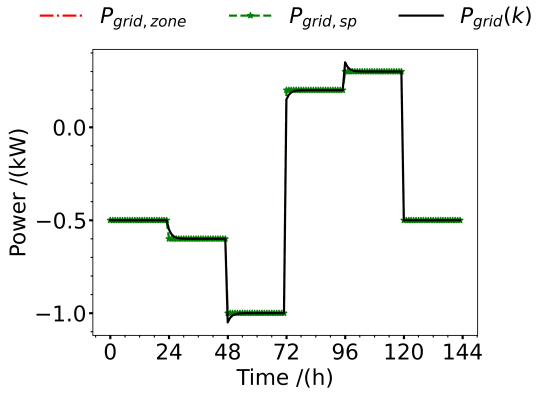

(a) Grid power tracking.

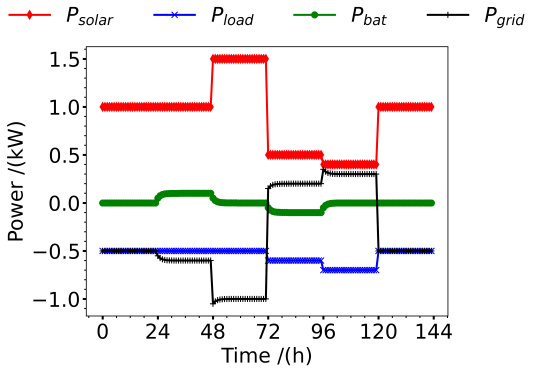

(b) Power exchange at the microgrid node.

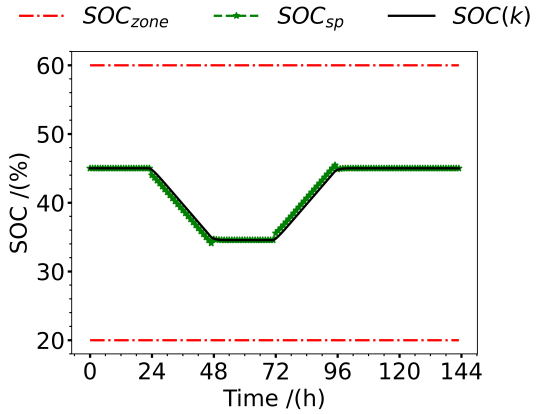

(c) Battery state of charge (SOC).

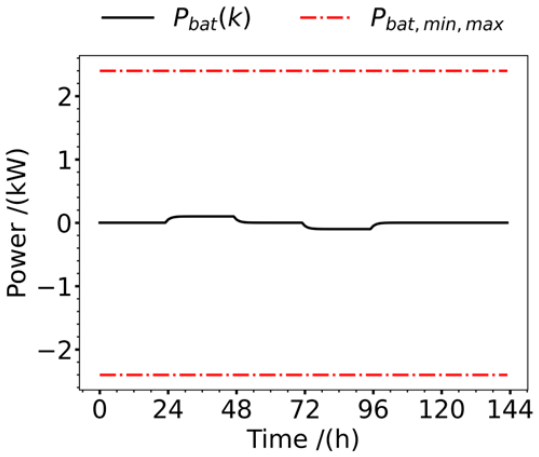

(d) Battery power and bounds.

Figure 5.2: Microgrid operation results. $P_{grid,zone}$ denotes the grid power in the zone, $P_{grid,sp}$ the grid power setpoint, and P_{grid} the actual grid power. P_{solar} is the solar power, P_{load} the load demand, P_{bat} the battery power, and SOC the battery state of charge.

Every 24 hours, both generation and consumption are assumed to remain constant, while the setpoint is adjusted to either purchase or sell energy. Within this strategy, each variation in generation and consumption leads to a redefinition of the P_{grid} setpoint, thereby characterizing a zone-based economic operation. During each zone, the optimization problem remains time-invariant, which facilitates the convergence of the control solution to a steady-state regime.

Finally, Figure 5.3 presents the evolution of the cost function V_k (top) and its discrete variation $\Delta V_k/\Delta t$ (bottom) throughout the simulation horizon. It can be observed that the cost function exhibits sharp peaks at the moments when transitions between operating zones occur, as defined in Table 5.1. These peaks reflect

the reformulation of the optimization problem in response to new operating targets imposed by the current zone, such as the desired power exchange with the main grid.

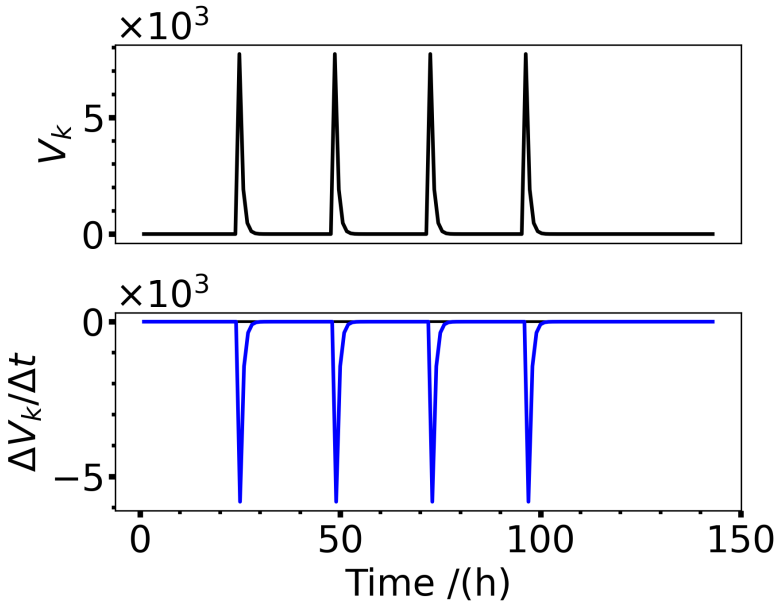

Figure 5.3: Cost function.

Immediately after each transition, the cost function decreases progressively until reaching minimal values, indicating that the system converges to the new optimal operating condition defined by the active zone. This behavior is confirmed by the $\Delta V_k/\Delta t$ curve, which remains strictly negative in the intervals where no zone change takes place. This confirms that, once the optimal control action is applied, the system cost does not increase over successive time steps.

This behavior directly relates to the stability proof developed in section Stabilizing proof, which demonstrates that, under nominal conditions and in the absence of abrupt disturbances, the optimal solution at time k can be inherited and applied at time $k+1$, while still satisfying all problem constraints. Furthermore, the proof guarantees that the cost function associated with the inherited solution is always greater than or equal to the cost obtained from the re-optimized solution, thereby characterizing the behavior of a discrete-time Lyapunov function.

Therefore, the results shown in Figure 5.3 not only illustrate the expected behavior of a stable system under predictive control but also provide empirical validation of the theoretical results established in the stability proof. It can thus be concluded

that the proposed MPC controller ensures practical stability and maintains recursive feasibility even under periodic reconfigurations of the operating zones, guaranteeing consistent system performance over time.

5.2 Case of study

Figure 5.4 presents a architecture of a microgrid consists of a solar power plant, wind power plant, a battery bank, supercapacitor bank, access to the main grid, load consumer and an electrolyzer with hydrogen storage.

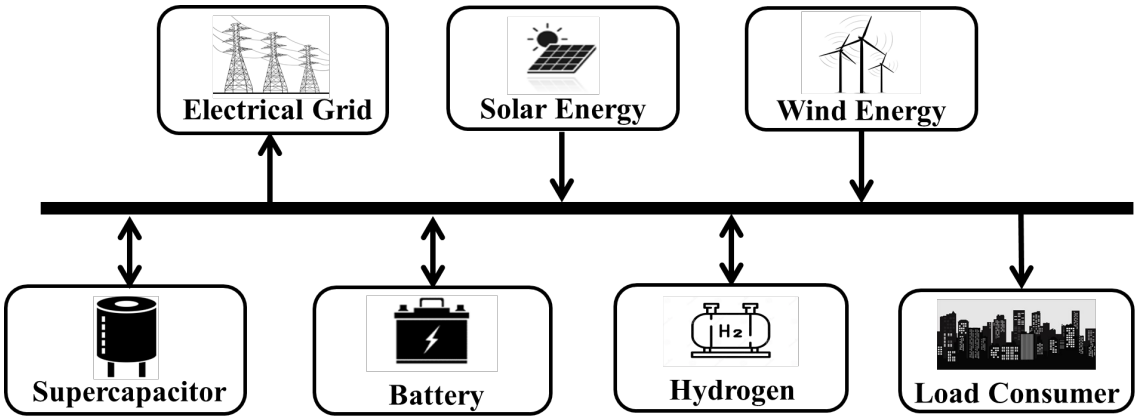

Figure 5.4: Microgrid architecture proposal.

Accordingly, the state-space representation is as follows:

$$\underbrace{\begin{bmatrix} SOC(k+1) \\ SHL(k+1) \\ SOE(k+1) \end{bmatrix}}_{\mathbf{x}(k+1)} = \underbrace{\begin{bmatrix} 1 & 0 & 0 \\ 0 & 1 & 0 \\ 0 & 0 & 1 \end{bmatrix}}_{\mathbf{A}} \underbrace{\begin{bmatrix} SOC(k) \\ SHL(k) \\ SOE(k) \end{bmatrix}}_{\mathbf{x}(k)} + \underbrace{\begin{bmatrix} \frac{T_s \eta_{bat}}{C_{bat}} & 0 & 0 \\ 0 & \frac{T_s \eta_{H_2}}{C_{H_2}} & 0 \\ 0 & 0 & \frac{T_s \eta_{sc}}{C_{sc}} \end{bmatrix}}_{\mathbf{B}} \underbrace{\begin{bmatrix} P_{bat}(k) \\ P_{H_2}(k) \\ P_{sc}(k) \end{bmatrix}}_{\mathbf{u}(k)} \tag{5.30}$$

$$\underbrace{\begin{bmatrix} SOC(k) \\ SHL(k) \\ SOE(k) \\ P_{grid}(k) \end{bmatrix}}_{\mathbf{y}(k)} = \underbrace{\begin{bmatrix} 1 & 0 & 0 \\ 0 & 1 & 0 \\ 0 & 0 & 1 \\ 0 & 0 & 0 \end{bmatrix}}_{\mathbf{C}} \underbrace{\begin{bmatrix} SOC(k) \\ SHL(k) \\ SOE(k) \end{bmatrix}}_{\mathbf{x}(k)} + \underbrace{\begin{bmatrix} 0 & 0 & 0 \\ 0 & 0 & 0 \\ 0 & 0 & 0 \\ 1 & 1 & 1 \end{bmatrix}}_{\mathbf{D}_u} \underbrace{\begin{bmatrix} P_{bat}(k) \\ P_{H_2}(k) \\ P_{sc}(k) \end{bmatrix}}_{\mathbf{u}(k)} + \underbrace{\begin{bmatrix} 0 & 0 & 0 \\ 0 & 0 & 0 \\ 0 & 0 & 0 \\ 1 & 1 & -1 \end{bmatrix}}_{\mathbf{D}_d} \underbrace{\begin{bmatrix} P_{solar}(k) \\ P_{wind}(k) \\ P_{load}(k) \end{bmatrix}}_{\mathbf{d}(k)} \tag{5.31}$$

Therefore, Equation (5.30) captures the storage system's state dynamics, while Equation (5.31) defines the controlled outputs. In this formulation, the state vector $\mathbf{x}(k) \in \mathbb{R}^{n_x}$ represents storage levels, and the input vector $\mathbf{u}(k) \in \mathbb{R}^{n_u}$ corresponds to storage power as the manipulated variable. The output vector $\mathbf{y}(k) \in \mathbb{R}^{n_y}$ comprises grid power and storage dynamics, whereas the disturbance vector $\mathbf{d}(k) \in \mathbb{R}^{n_d}$ includes photovoltaic generation, wind power, and load demand. System evolution is governed by the matrices $\mathbf{A}$, $\mathbf{B}$, $\mathbf{C}$, $\mathbf{D}_u$, and $\mathbf{D}_d$.

With the model defined, the proposed zone-based MPC is formulated using the following quadratic cost function:

$$\begin{aligned} V_{\mathrm{k}} =& (P_{grid} - P_{grid,sp})^{\mathrm{T}} \rho_e (P_{grid} - P_{grid,sp}) \\ &+ (SOC - SOC_{sp})^{\mathrm{T}} \frac{C_{re}}{C_{bat,cel}} (SOC - SOC_{sp}) \\ &+ (SOE - SOE_{sp})^{\mathrm{T}} \frac{C_{invest,sc}}{C_{sc,cel}} (SOE - SOE_{sp}) \\ &+ (SHL - SHL_{sp})^{\mathrm{T}} \frac{C_{invest}}{C_{H_2,sto}} (SLH - SHL_{sp}) \\ &+ \Delta P_{bat}^{\mathrm{T}} \frac{\rho_e}{\eta_{bat}} \Delta P_{bat} + \Delta P_{H_2}^{\mathrm{T}} \frac{\rho_{H_2}}{\eta_{H_2}} \Delta P_{H_2} + \Delta P_{sc}^{\mathrm{T}} \frac{\rho_e}{\eta_{sc}} \Delta P_{sc}, \end{aligned} \tag{5.32}$$

where the subscript sp is the set-point, ρ_e is the electrical price, ρ_{H_2} is the hydrogen price, η_{bat} is the battery efficiency, C_{re} is the cost of replacement the storage system, $C_{bat,cel}$ is the nominal power capacity, $C_{investi}$ is the is the investment in the electrolyzer and storage and $C_{H_2,sto}$ is the hydrogen storage capacity, and $C_{investi,sc}$ is the is the investment in the supercapacitor and storage and $C_{sc,cel}$ is the supercapacitor.

Finally, the control law of the QP-based zone-MPC proposed here can be generalized and formulated as the solution to the following optimization problem:

Problem 1

$$\min_{\mathbf{u}_k, \mathbf{y}_{sp,k}} V_{\mathrm{k}},$$

$$V_{\mathrm{k}} = \sum_{j=0}^{N-1} \|\mathbf{y}(k+j|k) - \mathbf{y}_{sp,k}\|_{\mathbf{Q}}^2 + \|\Delta\mathbf{u}(k+j|k)\|_{\mathbf{R}}^2, \tag{5.33}$$

subject to (5.30), (5.31), (5.9), (5.10), (5.11), (5.12), and:

$$\mathbf{d}(k+1|k) = \boldsymbol{f}(\mathbf{d}(k-n|k), \ldots, \mathbf{d}(k|k)) \tag{5.34}$$

where (5.34) represent the prediction of future disturbance in at time $k+1$, $\boldsymbol{f}(\cdot)$ represents a trained artificial neural network that incorporates past values and current values of the disturbances

The terms associated with $\mathbf{Q}$ represent the deviations of grid power, battery state of charge (SOC), supercapacitor state of energy (SOE), and stored hydrogen level (SHL) from their reference values, weighted by cost factors — such as equipment replacement cost ($C_{\text{re,cel}}$) or investment cost ($C_{\text{invest,sc}}$) ($C_{\text{invest,H2}}$), normalized by the nominal capacity of each component. The terms equivalent to $\mathbf{R}$ correspond to the direct costs related to power variations in the battery, electrolyzer/hydrogen system, and supercapacitor, expressed as the cost of electricity or hydrogen divided by the conversion efficiency of the respective device. Thus, higher weights in $\mathbf{Q}$ emphasize the importance of keeping the variables close to their setpoints, while higher weights in $\mathbf{R}$ encourage smoother control actions, avoiding abrupt changes, reducing operational costs, and penalizing excessive or inefficient use of resources.

5.3 Disturbance modeling

As detailed in Chapter 2, the proposed LSTM model employs a Nonlinear AutoRegressive (NAR) architecture, generating forecasts solely from past values of the system output. Operating in discrete time steps, the network produces one-step-ahead predictions that are recursively fed back as inputs to obtain multi-step forecasts. In this recursive framework, each predicted output forms part of the subsequent input, and the network's internal states are updated iteratively to capture the sequential dynamics accurately. Because no exogenous inputs are used, the approach conforms to the NAR paradigm defined by Connor et al. (1994), and it has been further extended in hybrid modeling studies such as Zhang (2003).

Figures 5.5a, 5.5b and 5.6 shows 336 hours of prediction from the trained models. The performance of the ANN was assessed using the Root Mean Squared Error (RMSE), Mean Absolute Error (MAE), which measures the average magnitude of prediction errors.

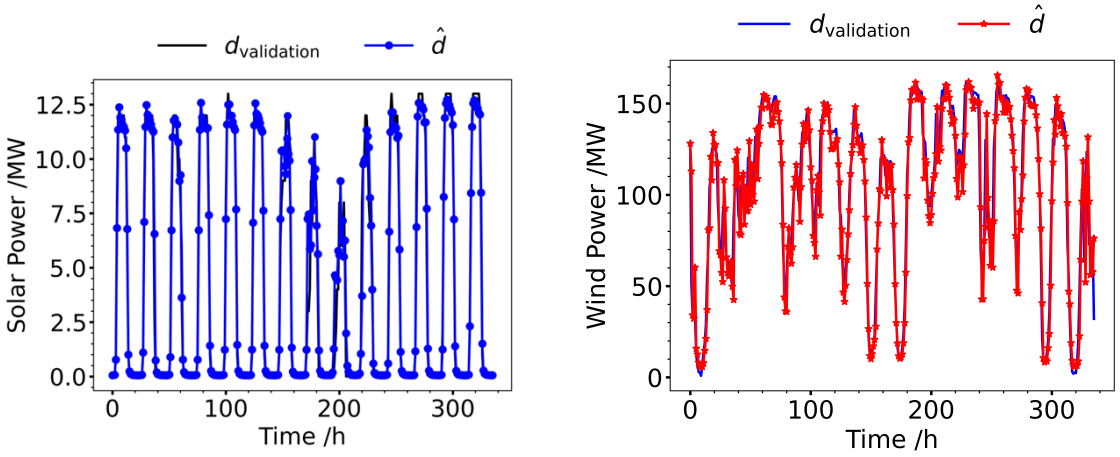

(a) Solar power prediction over 336 h.

(b) Wind power prediction over 336 h.

Figure 5.5: Two weeks of renewable power prediction over 336 h. $d_{validation}$ denotes the actual observed values in the test set, and $\hat{d}$ represents the predicted values by the artificial neural network.

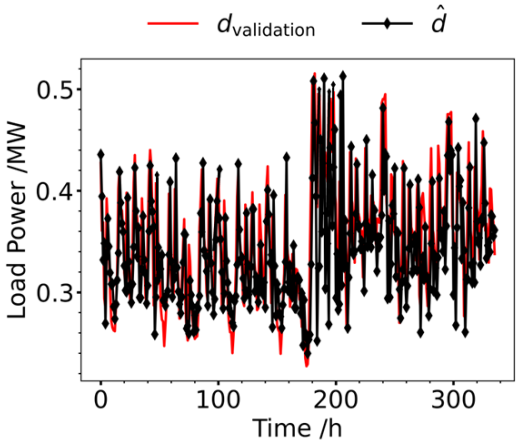

Figure 5.6: Two weeks of load consumption prediction over 336 h. $d_{validation}$denotes the actual observed values in the test set, and $\hat{d}$ represents the predicted values by the artificial neural network.

The forecasting performance for solar generation, wind generation, and load demand is summarized in Table 5.2.

Table 5.2: Prediction performance metrics for solar, wind, and load.

Variable	RMSE	MAE
Solar Generation	0.11	0.06
Wind Generation	0.13	0.09
Load Demand	0.10	0.07

For solar generation, the model achieved an RMSE of 0.11, and an MAE of 0.06 indicating strong accuracy and reliable variability representation. For wind, the RMSE of 0.13 and a MAE of 0.09 demonstrates excellent predictive performance with high correlation. For load, a low RMSE of 0.10 and an MAE of 0.07 reflects minimal absolute error, confirming the model's precision.

5.4 Simulation and results

The simulation of the zone-MPC proposed for the EMS of the industrial microgrid were solved using the CVXOPT framework (Andersen et al. 2020), implemented in Python 3.12.

The microgrid under study is situated in the municipality of Guanambi, located in the state of Bahia, Brazil. It comprises a photovoltaic power plant, a wind power plant, a battery storage system, a supercapacitor bank, a green hydrogen production unit, and an interconnection with the main power grid, as illustrated in Figure 5.7. Owing to the region's favorable solar and wind resource availability, the microgrid is capable of fully meeting the city's electrical demand. Furthermore, it is designed to dispatch surplus energy to the main power grid, which is managed by the Brazilian National System Operator (NSO).

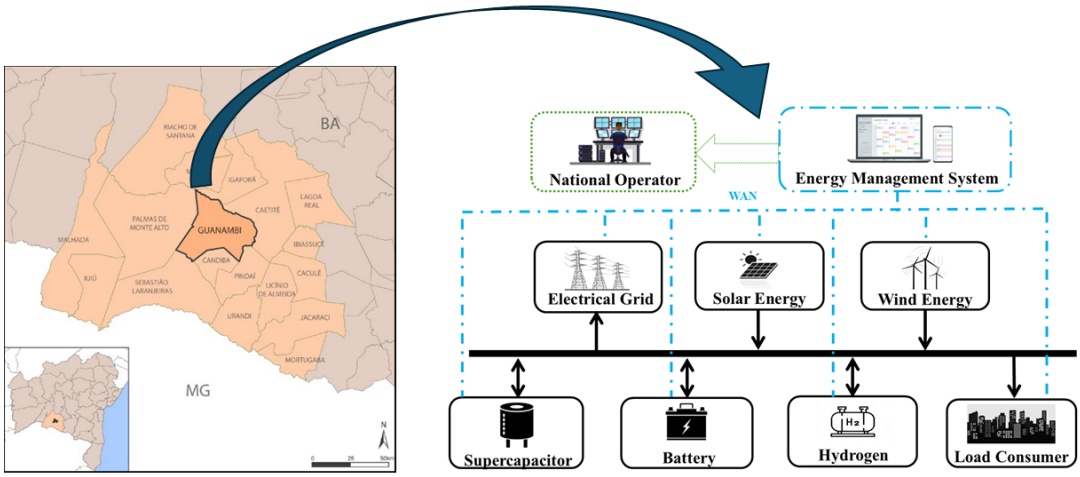

Figure 5.7: Case study of a microgrid in Guanambi. The map was adapted from Rodrigues (2021).

Figure 5.8 illustrates the block diagram of the proposed control loop for the industrial microgrid for Problem P1, and Table 5.3 summarizes the weighting matrices and the initial condition.

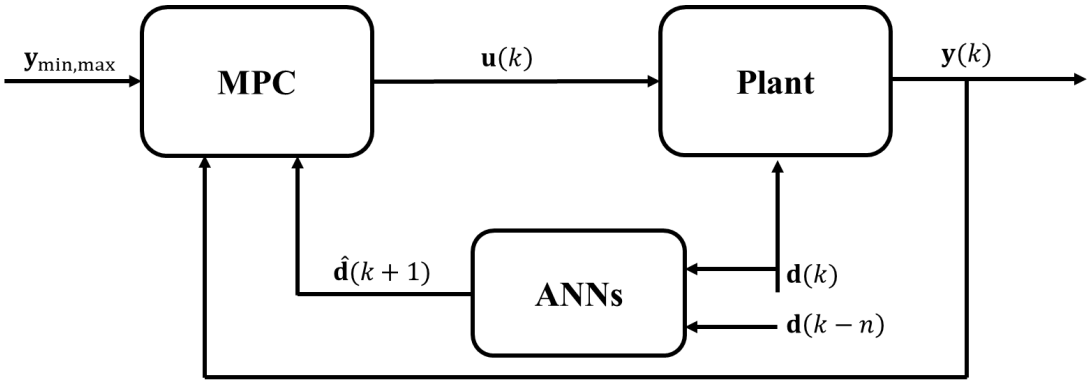

Figure 5.8: Block diagram of EMS. $\mathbf{y}_{\min,\max}$ is the output zone reference vector, $\mathbf{u}(k)$ is is input and $\mathbf{y}(k)$ is the output, $\mathbf{d}(k)$ is the disturbance, $\mathbf{d}(k-n)$ is the past information of the disturbances and $\hat{\mathbf{d}}(k+1)$ is the measured process disturbance.

Table 5.3: Weighting matrices and the initial condition.

Parameters	Description	Value
$\mathbf{x}(0)$	Initial condition	$[50\ 20\ 20]^{\mathrm{T}}$ (%)
$\mathbf{u}(0)$	Initial condition	$[0\ 0\ 0]^{\mathrm{T}}$ (MW)
$\mathbf{u}_{\min}$	Minimum input	$[-100\ -50\ -30]^{\mathrm{T}}$(MW)
$\mathbf{u}_{\max}$	Maximum input	$[100\ 50\ 30]^{\mathrm{T}}$(MW)
$\Delta\mathbf{u}$	Inputs increments	$[100\ 50\ 30]^{\mathrm{T}}$(MW)
η_{bat}	Battery efficiency	98%
η_{H_2}	Electrolyzer efficiency	74%
η_{sc}	Supercapacitor Efficiency	99%
C_{bat}	Power capacity of battery bank	800MWh
C_{H2}	Maximum Volume	1200Nm^3
C_{sc}	Power capacity of supercapacitor	800MWh
T_s	Sampling period	1h
N	Horizon control	3
C_{re}	Replacement cost of the battery	\$325
C_{H_2}	Electrolyzer maintenance cost	\$500
C_{H_2}	Electrolyzer maintenance cost	\$400
$\mathbf{R}$	Input weighting matrix	diag(\$0.67, \$3.82, \$0.65)
$\mathbf{Q}$	Output weighting matrix	diag(0.4\$/MW, 0.3\$/Nm^3, 0.62\$/MW, \$0.65)

Table 5.4 presents the definition of operating zones over a one-week horizon, segmented into 24-hour intervals. For each zone, the minimum and maximum bounds for the output vector $\mathbf{y}^{\mathrm{T}}$ are specified. This vector encapsulates four normalized system indicators relevant to the control problem, including renewable penetration, battery state of charge, power exchange status, and hydrogen tank level. These zones reflect distinct operating conditions and are used to enforce time-varying constraints in the predictive control formulation. The piecewise bounds enable the controller to adapt its strategy according to expected variations in resource availability and demand throughout the week.

Table 5.4: Zone definitions.

Time /(h)	$\mathbf{y}^{\mathrm{T}}_{\mathrm{min}}$	$\mathbf{y}^{\mathrm{T}}_{\mathrm{max}}$
0 to 23	[30% 20% 0% 40MW]	[40% 30% 1% 100MW]
24 to 47	[35% 30% 0% 40MW]	[60% 40% 1% 100MW]
48 to 71	[20% 40% 0% 80MW]	[40% 50% 1% 175MW]
72 to 95	[35% 50% 0% 20MW]	[60% 60% 1% 100MW]
96 to 119	[30% 60% 0% 80MW]	[60% 70% 1% 175MW]
120 to 143	[30% 70% 0% 40MW]	[60% 80% 1% 150MW]
144 to 168	[15% 80% 0% 55MW]	[35% 90% 1% 100MW]

Figure 5.10a shows the power exported to the utility grid; Figure 5.10b depicts the evolution of the battery state of charge (SOC); Figure 5.10c depicts the evolution of the supercapacitor state of energy (SOE); and Figure 5.10d describes the hydrogen storage level. Figure 5.9 represents the power exchange at the microgrid node.

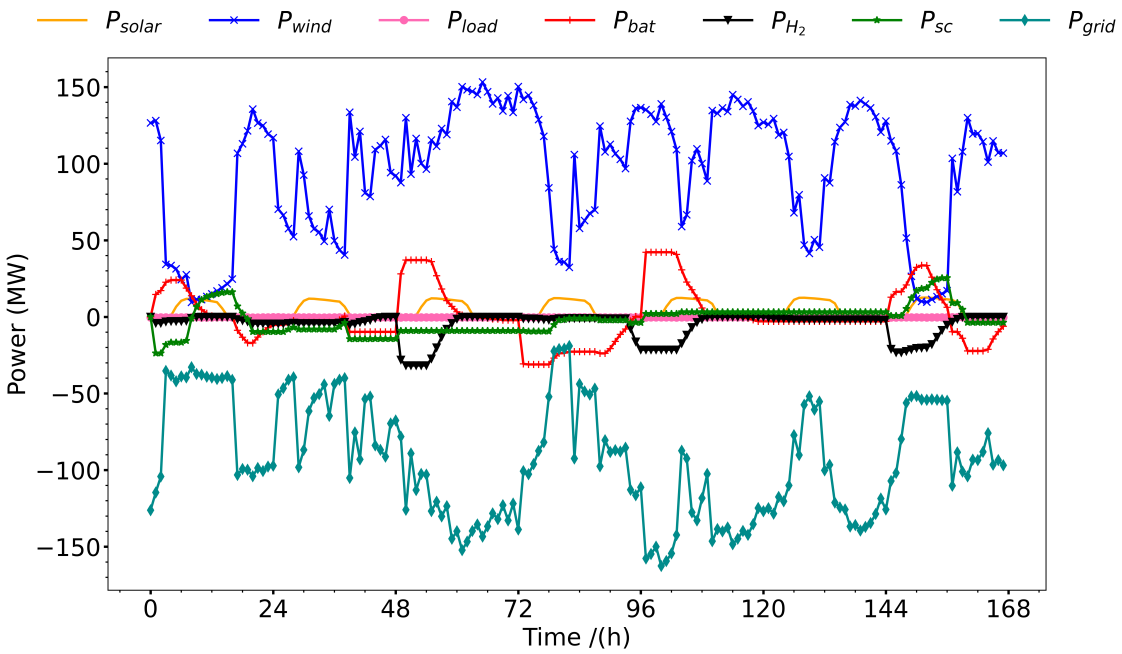

Figure 5.9: Power exchange at the microgrid node with manipulated variables and disturbances. P_{solar}: solar power. P_{wind}: wind power. P_{load}: load consumer power. P_{bat}: power exchanged with the battery bank. P_{H_2}: hydrogen power. P_{sc}: supercapacitor power. P_{grid}: power sold the grid.

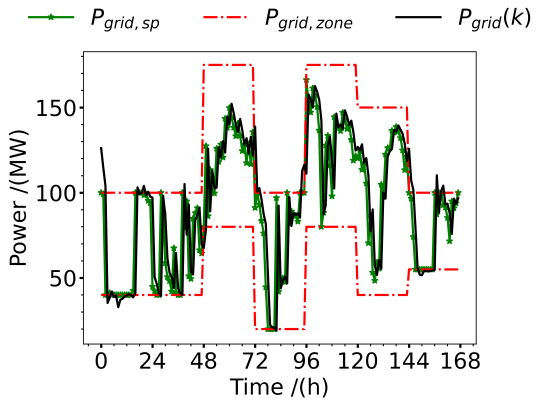

(a) Power sold to the energy concessionaire. $P_{grid,zone}$ denotes the grid power in the zone, $P_{grid,sp}$ is the grid power setpoint, and P_{grid} represents the actual grid power at time step k.

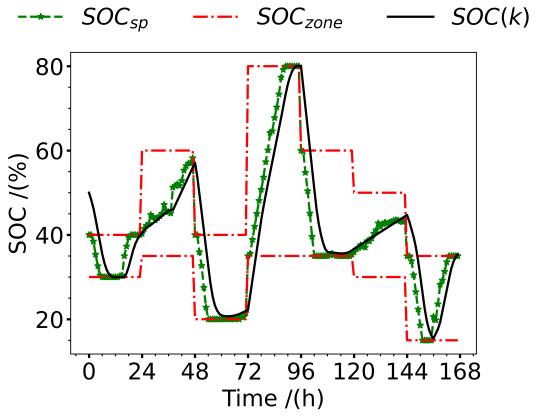

(b) Battery State of Charge (SOC). SOC_{zone} refers to the battery's state of charge within the zone, SOC_{sp} indicates the desired setpoint, and SOC corresponds to the actual value at time step k.

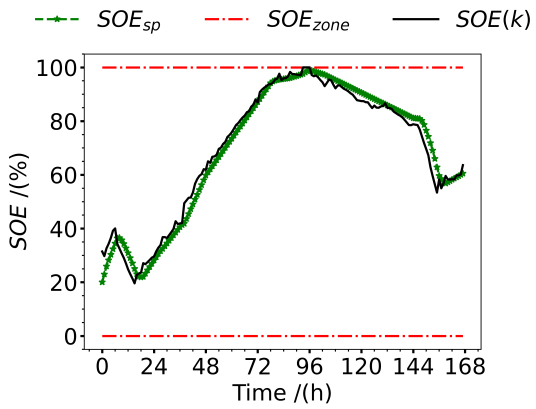

(c) Supercapacitor State of Energy (SOE). SOE_{zone} refers to the supercapacitor's energy level within the zone, SOE_{sp} indicates the target setpoint, and SOE corresponds to the actual state at time step k.

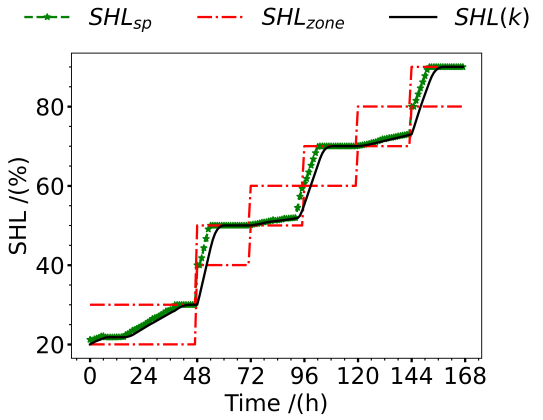

(d) Storage Hydrogen Level (SHL). SHL_{zone} refers to the hydrogen storage level within the zone, SHL_{sp} indicates the target setpoint, and SHL corresponds to the actual storage level at time step k.

Figure 5.10: Operational variables and storage states of the microgrid.

In this simulation, the operation of the microgrid was planned over a 168-hour horizon (one week), with re-planning performed every 24 hours. The primary objective is to fully supply the local load demand and subsequently sell any surplus energy to NSO. However, due to the intermittent nature of renewable energy sources, not all of the generated surplus can be directly injected into the main grid. This limitation is necessary to prevent potential overloads that could lead to network shutdowns caused by power limit violations.

To mitigate this issue, energy storage systems are employed. Figure 5.10a pre-

sents the energy sold to the NSO, regulated through different operational zones, while Figure 5.10b shows the energy stored in the battery bank, also governed by defined operational bands. During periods of high renewable generation, a smaller selling zone and a larger battery charging zone are adopted. The opposite strategy is applied during periods of lower generation, prioritizing energy export over storage. This approach aims to smooth the power injection into the grid by storing excess energy for later use, thus enabling safer integration with the NSO. It is also observed that, at certain moments, the established limits are violated due to momentary surpluses or deficits in the energy generated within the respective range. However, these violations are brief, and the controller quickly acts to bring the variable back within the desired range, thereby maintaining the control objectives.

Figure 5.10c and Figure 5.10d illustrate the operation of the supercapacitor bank and the green hydrogen production system, respectively. For the supercapacitors, a constant operational zone was maintained throughout the simulation, given their high efficiency and ability to handle high energy densities over short periods. In contrast, the hydrogen storage system operated with progressively increasing operational bands over time, aiming to maximize hydrogen production. This strategy enhances the potential for hydrogen commercialization as an industrial feedstock. Accordingly, the power exchange among the microgrid components is illustrated in Figure 5.9.

MPC with feedforward action allows the incorporation of measured disturbances directly into the prediction stage, enabling the controller to adjust the manipulated variables in advance to mitigate the effects of these disturbances on the system outputs (Camacho & Bordons 2004). In this context, Artificial Neural Networks (ANN) can be used as a feedforward strategy, acting as approximate models of the disturbance dynamics or their influence on the system. In Figure 5.11, Figure 5.12 and Figure 5.13 shows the difference in the MPC with and without the feedforward ANN over a 168-hour prediction horizon.

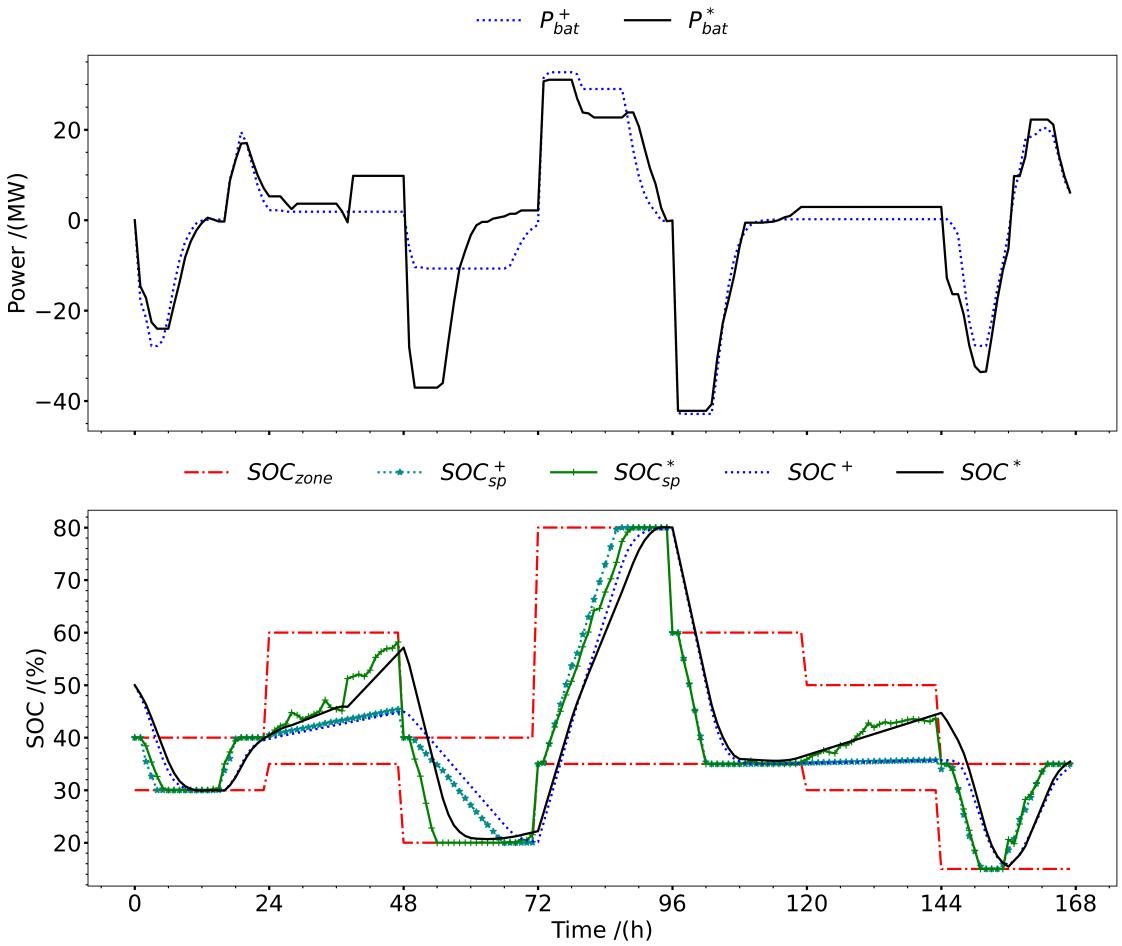

Figure 5.11: Comparison between using ANNs as a disturbance prediction model and without a prediction model for battery. The superscript (+) indicates the result obtained without the feedforward action and the superscript (*) indicates the result obtained with the ANN feedforward action.

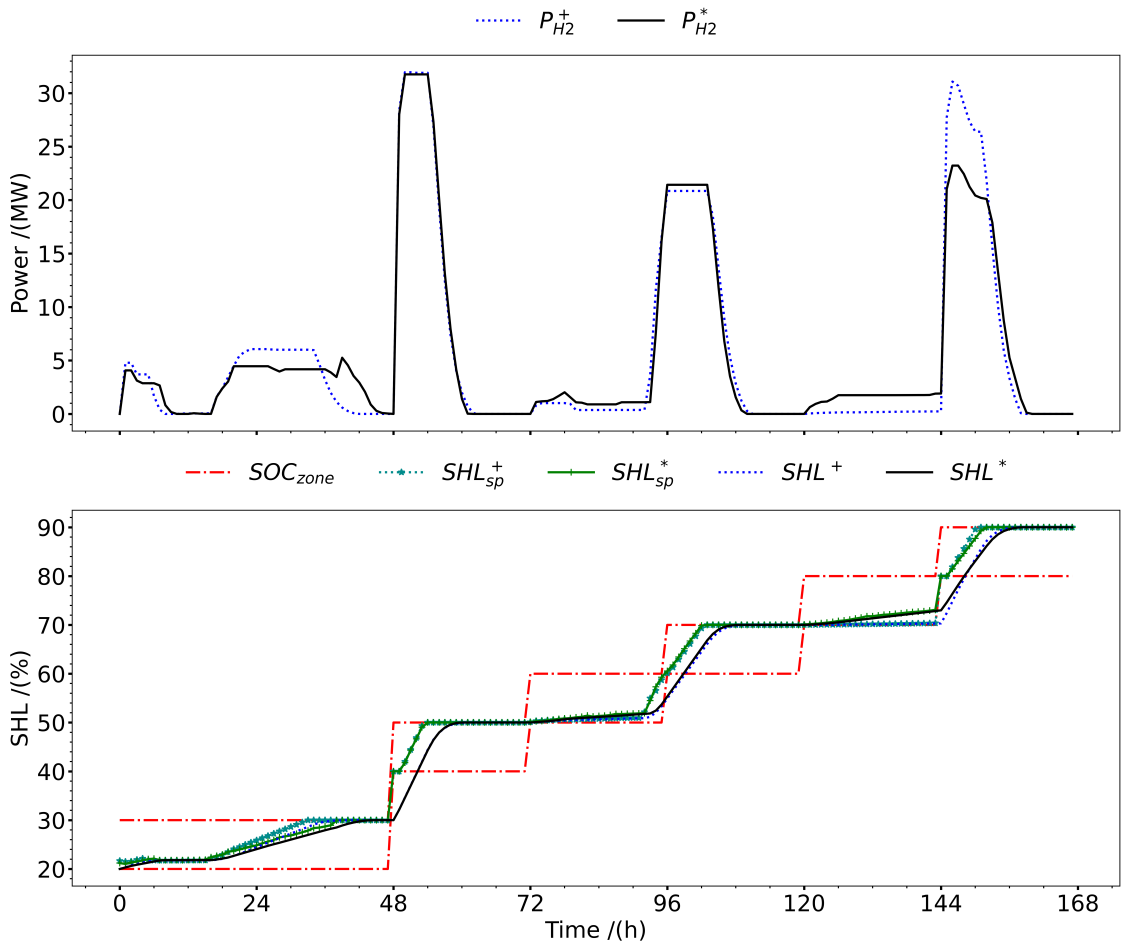

Figure 5.12: Comparison between using ANNs as a disturbance prediction model and without a prediction model for hydrogen. The superscript (+) indicates the result obtained without the feedforward action and the superscript (*) indicates the result obtained with the ANN feedforward action.

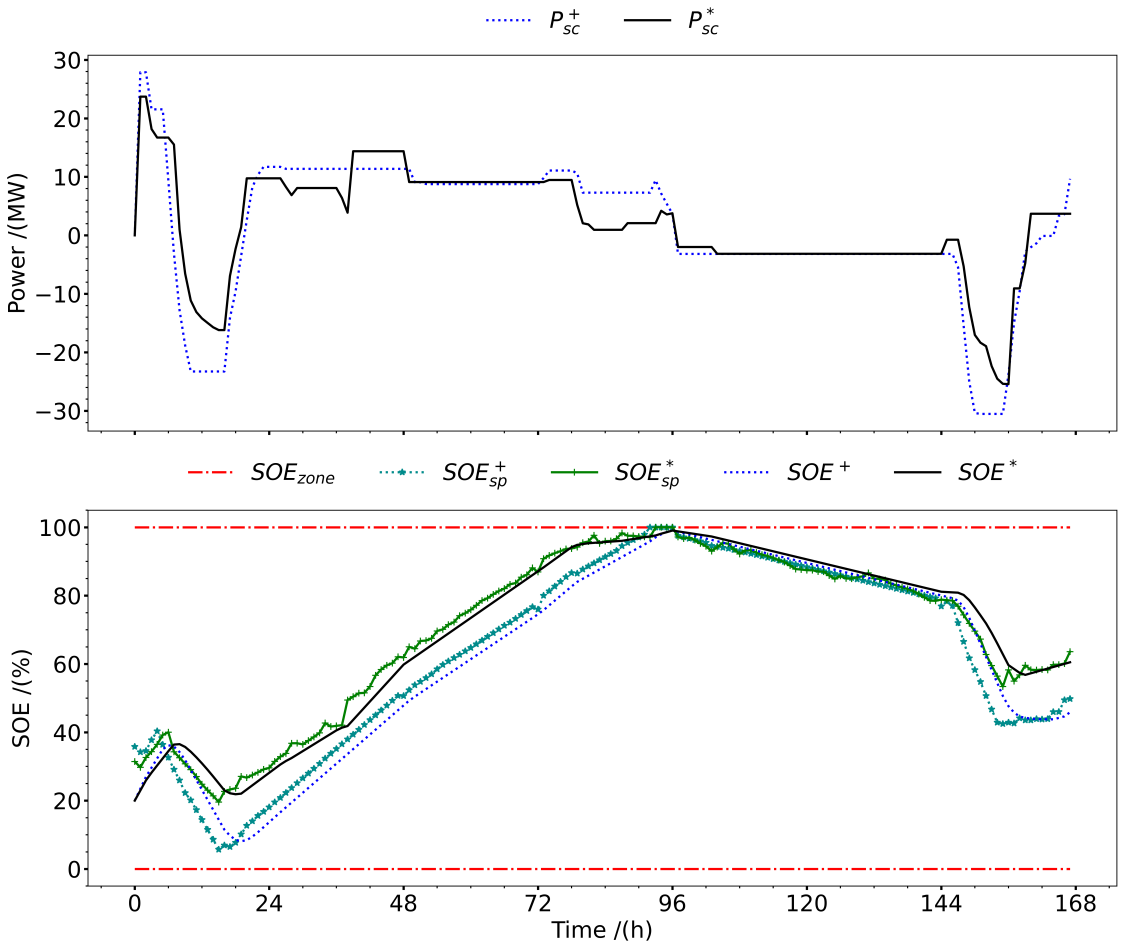

Figure 5.13: Comparison between using ANNs as a disturbance prediction model and without a prediction model for supercapacitor. The superscript (+) indicates the result obtained without the feedforward action and the superscript (*) indicates the result obtained with the ANN feedforward action.

The results demonstrate that in both implementations – with and without the feedforward artificial neural network (ANN) – the controller is able to achieve its operational objectives while respecting system constraints and equipment limits. This confirms the robustness of the control scheme even in the absence of advanced forecasting. The main advantage lies in the predictive capability of the LSTM, which enables the controller to anticipate trends in energy generation and demand more accurately. As a result, the controller can take more proactive actions, such as charging or discharging the battery or charging or discharging the supercapacitor and adjusting hydrogen production more efficiently, thereby minimizing losses and optimizing operation.

For instance, with the use of the LSTM model, the controller is able to anticipate

changes in the system: it starts charging the battery or the supercapacitor before a predicted increase in renewable generation, and increases hydrogen production in anticipation of a forecasted drop in generation. These proactive actions are reflected in the manipulated variables (Figure 5.11, Figure 5.12 and Figure 5.13). Such anticipatory responses are not feasible with the version of the controller without RNN-based forecasting, which reacts only to current conditions. Moreover, energy

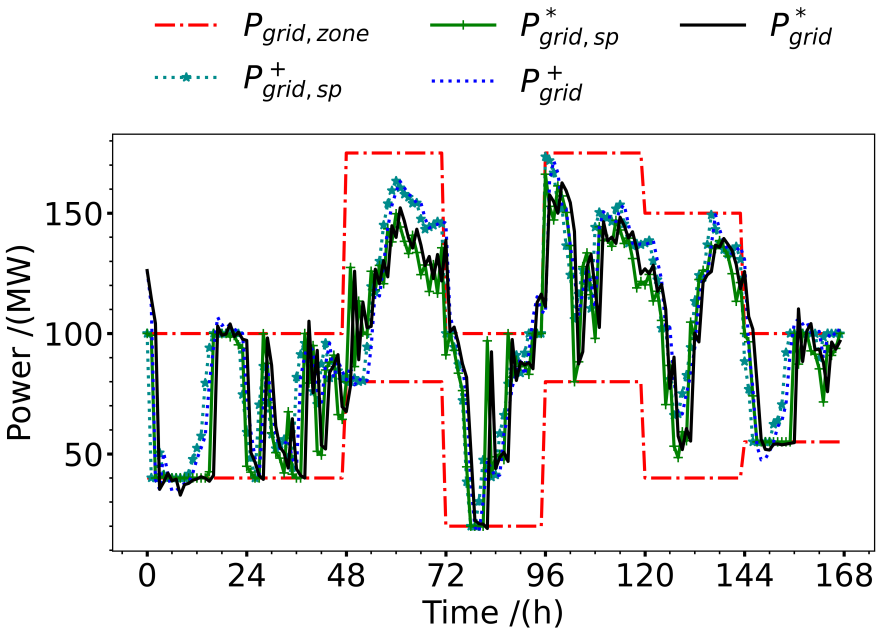

Figure 5.14: Comparison between using ANNs as a disturbance prediction model and without a prediction model for grid power. The superscript (+) indicates the result obtained without the feedforward action and the superscript (*) indicates the result obtained with the ANN feedforward action.

sales to the grid are also optimized with the LSTM approach, as the controller can better capitalize on periods of energy surplus and more favorable selling prices, potentially resulting in higher revenues or reduced operational costs (Figure 5.14).

In summary, although both approaches are feasible, the RNN-based implementation proves more effective in dynamic and uncertain environments — characteristic of energy systems with intermittent renewable sources. By forecasting the system's future behavior, the controller gains a strategic advantage that translates into superior overall performance. For comparison between the results with and without the RNN, the following economic function was adopted. Maximizing energy sale ℓ_{grid}, maximizing hydrogen production ℓ_{H_2}, and accounting for battery-related costs:

cell replacement ℓ_{bat_1}, charge/discharge degradation ℓ_{bat_2}, state-of-charge variations ℓ_{bat_3}ensuring system performance and economic viability; and cell replacement ℓ_{sc},

$$\begin{aligned}\ell_{eco}(x(k),u(k),p_e(k),p_{H_2}(k)) = &\overbrace{p_e(k)T_s\lambda_1 P_{grid}(k)}^{\ell_{grid}} + \overbrace{p_{H_2}(k)T_s\lambda_2 P_{H_2}(k)}^{\ell_{H_2}} \\ &- \lambda_3 \overbrace{\frac{C_{re}T_s}{C_{Wh}}P_{bat}(k)}^{\ell_{bat1}} - \overbrace{\lambda_4 \frac{P_{bat}(k)}{V_{bat}I_{bat}}}^{\ell_{bat2}} \\ &- \overbrace{\|\mathbf{x}(k+1)-\mathbf{x}(k)\|^2_{Q_{bat}}}^{\ell_{bat3}} - \lambda_5 \overbrace{\frac{C_{invest,sc}T_s}{C_{sc,cel}}P_{sc}(k)}^{\ell_{sc}}\end{aligned} \tag{5.35}$$

The microgrid operation is optimized by balancing power sale (P_{grid}), hydrogen production (P_{H_2}), battery charging/discharging (P_{sc}) and supercapacitor charging/-discharging (P_{bat}), with respective weights λ_1, λ_2, λ_3, and λ_4. The model also includes the battery cell replacement cost (C_{re}) and the coefficient λ_4, considering battery voltage (V_{bat}), current (I_{bat}), hydrogen price (p_{H_2}), and electricity price (p_e) to minimize economic and operational impacts, ensuring efficient and cost-effective energy management.

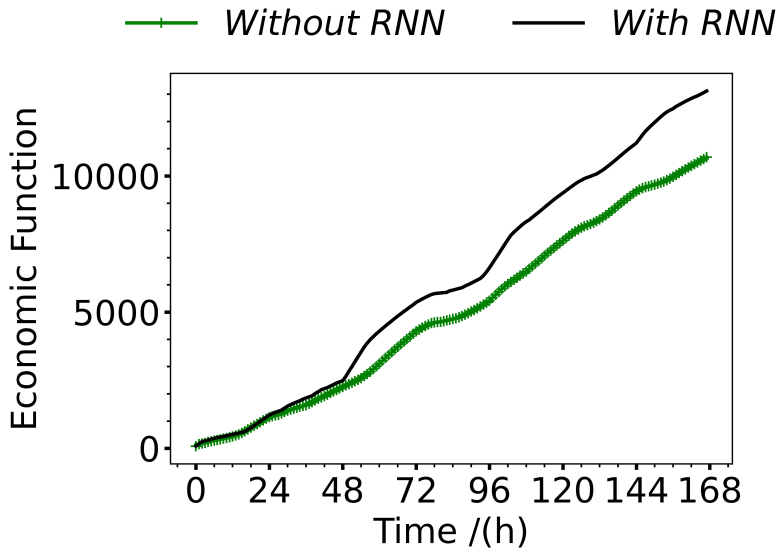

Figure 5.15: Economic Function.

Figure 5.15 the profile of accumulated profit obtained from (5.35). The result indicate that the microgrid operated in an economically viable manner under the

zone-MPC-ANN strategy, demonstrating the effectiveness of the proposed controller in the optimal allocation of energy resources and the maximization of financial returns.

5.5 Conclusion

This Chapter proposes a novel single-layer zone Model Predictive Control (MPC) formulation based on Quadratic Programming, applied to an energy management system supported by artificial intelligence for disturbance forecasting. The proposed approach introduces a new organization state-space representation and structures the optimization problem so that only a single problem is solved over the control horizon. This enables the microgrid operator to steer system operation toward more economically advantageous scenarios by leveraging the predictive capabilities of machine learning models.

The obtained results demonstrate that the proposed formulation is effective and robust under variations in operational setpoints, highlighting the controller's adaptability. Furthermore, the integration of neural networks significantly enhanced system performance by increasing robustness and predictive accuracy.

From a theoretical standpoint, a stabilizing analysis was conducted to demonstrate that the proposed control strategy guarantees recursive feasibility and ensures the monotonic decrease of the cost function, which acts as a Lyapunov function. This behavior confirms the nominal convergence of the closed-loop system toward an economically optimal operating point, provided the system model and forecasts are accurate. By incorporating these stability guarantees into the predictive framework, the controller not only optimizes performance but also provides formal assurances of safety and reliability.

These findings confirm that the combination of predictive control and artificial intelligence supports more efficient and robust decision-making aligned with the economic goals of microgrid operation.

Chapter 6

Conclusion

This dissertation proposes Model Predictive Control (MPC) strategies for implementation within an Energy Management System (EMS) applied to electrical microgrids. The EMS represents the top layer of the hierarchical control structure used to coordinate the various subsystems of the microgrid. Due to its similarity to the hierarchical control architecture widely adopted in process industries, several MPC techniques can be adapted and applied in a similar fashion. Accordingly, the developed controllers aim to meet the main operational objectives of the EMS:

I. Management of the microgrid based on economic criteria;

II. Control of power flow among the subsystems of the microgrid;

III. Interaction of the microgrid with the main power grid;

IV. Active participation of the microgrid in the electricity market.

The first contribution consisted of the development of a two-layer MPC controller based on Quadratic Programming (QP). While most of the MPC literature for microgrids typically relies on Nonlinear Programming to solve the optimization problem, the QP-based approach stands out for its enhanced numerical robustness and reduced computational burden. To evaluate the effectiveness of the proposed method, a process plant model was implemented using AVEVA Process Simulation. The results demonstrated improved algorithm convergence, greater numerical stability, and the feasibility of scaling the proposed strategy to larger systems.

Considering that renewable energy sources and consumer load are treated as disturbances in the control problem, several modeling techniques for such disturbances were explored. Among these, Artificial Intelligence – particularly Artificial Neural

Networks (ANNs) – proved to be highly efficient and robust, positioning itself as a promising tool for integration with smart grids. The second contribution, therefore, involved the modeling of solar and wind generation, as well as consumer load profiles in the city of Guanambi, Bahia, Brazil. In this context, the QP-based MPC strategy was applied to an industrial – scale microgrid, as opposed to the earlier residential-scale application. In addition to preserving the numerical advantages of the QP formulation, the integration of ANN in a feedforward configuration enabled the anticipation of disturbances, improving the controller's decision-making process. This anticipation led to reduced control effort and more effective responses to fluctuations in generation and demand.

Aiming to maximize the profit from energy sales to the main power grid, the third contribution introduced a novel MPC strategy that incorporates economic targets directly into the objective function. To this end, a zone-based MPC controller was proposed, in which setpoints are defined as economically viable regions that can be pre-established by the microgrid operator. The ANN-based disturbance modeling methodology was also applied in this context. Simulations, again based on data from the city of Guanambi, showed that the controller is capable of operating within economically optimal zones while meeting the load demand and complying with long-term economic schedules. Moreover, a stability analysis confirmed that the proposed control scheme guarantees recursive feasibility and nominal convergence, providing theoretical assurance of closed-loop stability alongside practical economic performance

In summary, this dissertation contributes to the development of QP-based MPC controllers supported by artificial intelligence for disturbance modeling. The results demonstrate the efficiency, flexibility, and scalability of the proposed structure, making it suitable for microgrids of varying sizes, with multiple loads and renewable energy sources. The presented contributions have practical implications for microgrids at different scales, emphasizing the economic benefits of the proposed operational strategies.

6.1 Direction of future works

This work has yet to address specific issues, but they could be considered possible areas for future research. These include:

- Implement a single-layer QP-based MPC strategy integrated with a process simulator (Software-in-the-Loop): In Chapter 3, a two-layer MPC strategy based on quadratic programming (QP) was proposed and integrated with the AVEVA Process Simulation environment. However, economically optimal operating points may occur during transient regimes rather than steady state. Therefore, implementing a single-layer MPC directly coupled with the process simulator may enhance the robustness of the control strategy by enabling testing in scenarios that more closely resemble real operational conditions. Similarly, it is recommended to implement the control law proposed in Chapter 5 within a process simulator to validate its performance under dynamic system behavior.

- Propose a data-driven mathematical model: By leveraging process simulation tools, it is possible to extract system-specific behaviors, including losses and scale-dependent effects. This enables the construction of data-driven models using system identification techniques, ranging from classical approaches such as NARX (Nonlinear AutoRegressive with eXogenous input) models to modern artificial intelligence methods, including deep or hybrid neural networks. These models can better capture unmodeled dynamics and improve predictive accuracy.

- Apply the proposed strategies to interconnected microgrid systems: The techniques developed in this work were applied to a single microgrid. However, in more complex scenarios where operators of different microgrids can trade energy directly – either to meet demand or to sell surplus energy – it is essential to expand the proposed strategies to multi-microgrid systems. This extension would require the development of coordination mechanisms between operators and the implementation of distributed or decentralized control architectures.

- Extend the approach to systems with uncertainties and parameter variations:

In real-world applications, system parameters and operating conditions are subject to change. Incorporating robust or stochastic MPC techniques can help explicitly handle such uncertainties, thereby increasing the reliability of the control strategy.

- Develop a real-time monitoring and supervisory interface: To facilitate the practical deployment of the proposed control strategies in industrial environments, the development of graphical user interfaces is recommended. These interfaces would enable real-time visualization of system variables, forecasts, control decisions, and performance indicators.

- Evaluate long-term economic and environmental impacts: Based on the proposed control strategies, long-term simulations under different demand and generation profiles can be conducted to assess economic outcomes (e.g., operational costs, accumulated profit) and environmental benefits (e.g., avoided emissions, increased use of renewable sources).

References

Ackermann, T., Andersson, G. & Söder, L. (2001), 'Distributed generation: a definition', *Electric power systems research* **57**(3), 195–204.

Adetola, V. & Guay, M. (2010), 'Integration of real-time optimization and model predictive control', *Journal of Process Control* **20**(2), 125–133.

Agreement, P. (2015), Paris agreement, *in* 'report of the conference of the parties to the United Nations framework convention on climate change (21st session, 2015: Paris). Retrived December', Vol. 4, HeinOnline, p. 2.

Akyildiz, I. F., Wang, X. & Wang, W. (2005), 'Wireless mesh networks: A survey', *Computer Networks* **47**(4), 445–487.

Alarcón, M. A. (2024), 'Diseño y aplicación de estrategias de control predictivo económico–estocástico para la gestión de microrredes eléctricas'.

Alarcón, M. A., Alarcón, R. G., González, A. H. & Ferramosca, A. (2022), 'Economic model predictive control for energy management of a microgrid connected to the main electrical grid', *Journal of Process Control* **117**, 40–51.

Alarcón, M. A., Alarcón, R. G., González, A. H. & Ferramosca, A. (2023), 'A scenario-based economic-stochastic model predictive control for the management of microgrids', *Sustainable Energy, Grids and Networks* **36**, 101205.

Alarcón, R. G., Alarcón, M. A., González, A. & Ferramosca, A. (2024), 'Artificial neural networks for energy demand prediction in an economic mpc-based energy management system', *Authorea Preprints* .

Andersen, M., Dahl, J. & Vandenberghe, L. (2020), 'Cvxopt: Convex optimization', *Astrophysics Source Code Library* pp. ascl–2008.

Angeli, D., Amrit, R. & Rawlings, J. B. (2012), 'On average performance and stability of economic model predictive control', *IEEE Transactions on Automatic Control* **57**(7), 1615–1626.

Bayindir, R., Colak, I., Fulli, G. & Demirtas, K. (2016), 'Smart grid technologies and applications', *Renewable and sustainable energy reviews* **66**, 499–516.

Bengio, Y. (2012), Practical Recommendations for Gradient-Based Training of Deep Architectures, *in* 'Neural Networks: Tricks of the Trade', 2nd edn, Springer, pp. 437–478.

Bergstra, J. & Bengio, Y. (2012), 'Random search for hyper-parameter optimization', *The journal of machine learning research* **13**(1), 281–305.

Bhojane, P. (2022), 'Recent advances and fundamentals of pseudocapacitors: Materials, mechanism, and its understanding', *Journal of Energy Storage* **45**, 103654.

Biegler, L. T. (2009), Technology advances for dynamic real-time optimization, *in* 'Computer Aided Chemical Engineering', Vol. 27, Elsevier, pp. 1–6.

Bordons Alba, C., García-Torres, F. & Valverde Isorna, L. (2015), 'Gestión óptima de la energía en microrredes con generación renovable', *Revista Iberoamericana de Automática e Informática Industrial, 12 (2), 117-132.* .

Bordons, C., Garcia-Torres, F. & Ridao, M. A. (2020), *Model predictive control of microgrids*, Vol. 358, Springer.

Bouckaert, S., Pales, A. F., McGlade, C., Remme, U., Wanner, B., Varro, L., D'Ambrosio, D. & Spencer, T. (2021), 'Net zero by 2050: A roadmap for the global energy sector'.

Camacho, E. F. & Bordons, C. (2004), *Model Predictive Control*, 2nd edn, Springer.

CCEE (2024), 'Câmara de comercialização de energia elétrica'.

Chatterjee, D. P. & Nandi, A. K. (2021), 'A review on the recent advances in hybrid supercapacitors', *Journal of Materials Chemistry A* **9**(29), 15880–15918.

Connor, J. T., Martin, R. D. & Atlas, L. E. (1994), 'Recurrent neural networks and robust time series prediction', *IEEE Transactions on Neural Networks* **5**(2), 240–254.

Conte, E., Mendes, P. R. & Normey-Rico, J. E. (2020), 'Economic management based on hybrid mpc for microgrids: A brazilian energy market solution', *Energies* **13**(13), 3508.

Conway, B. E. (2013), *Electrochemical supercapacitors: scientific fundamentals and technological applications*, Springer Science & Business Media.

Das, I., Bhattacharya, K. & Canizares, C. (2014), 'Optimal incentive design for targeted penetration of renewable energy sources', *IEEE Transactions on Sustainable Energy* **5**(4), 1213–1225.

De Souza, M. B., Odloak, D. & Zanin, A. C. (2010), 'Real time optimization (rto) with model predictive control (mpc)', *Computers & Chemical Engineering* **34**(12), 1999–2006.

Developers, T. (2022), 'Tensorflow', *Zenodo* .

Dobos, A. P. (2013), Pvwatts version 1: Technical reference, Technical report, National Renewable Energy Laboratory (NREL), Golden, CO (United States).

Driesse, A., Jain, P. & Harrison, S. (2008), Beyond the curves: Modeling the electrical efficiency of photovoltaic inverters, *in* '2008 33rd IEEE photovoltaic specialists conference', IEEE, pp. 1–6.

Engell, S. (2007), 'Feedback control for optimal process operation', *Journal of process control* **17**(3), 203–219.

Erdiwansyah, f., Mahidin, f., Husin, H., Nasaruddin, f., Zaki, M. & Muhibbuddin, f. (2021), 'A critical review of the integration of renewable energy sources with various technologies', *Protection and control of modern power systems* **6**, 1–18.

Fang, X., Misra, S., Xue, G. & Yang, D. (2011), 'Smart grid—the new and improved power grid: A survey', *IEEE communications surveys & tutorials* **14**(4), 944–980.

Galli, S., Scaglione, A. & Wang, Z. (2011), 'Grid communications for smart grid—enabling smart grid communications', *Proceedings of the IEEE* **99**(6), 998–1027.

Garcia, N., Falcon, K., Thomas, C., Robledo, J., Rocha, S. & Yousufuddin, M. (2021), 'Crystal structure of a zirconium based hydrogen storage material', *Acta Cryst* **77**, a10.

Gautier, A., Jacqmin, J. & Poudou, J.-C. (2018), 'The prosumers and the grid', *Journal of Regulatory Economics* **53**(1), 100–126.

Gommers, R., Virtanen, P., Burovski, E., Weckesser, W., Oliphant, T. E., Haberland, M., Cournapeau, D., Reddy, T., Peterson, P., Nelson, A. et al. (2022), 'scipy/scipy: Scipy 1.9. 0', *Zenodo* .

Graham, E., Fulghum, N. & Altieri, K. (2025), Global electricity review 2025, Technical report, Ember.

Greff, K., Srivastava, R. K., Koutník, J., Steunebrink, B. R. & Schmidhuber, J. (2016), 'Lstm: A search space odyssey', *IEEE transactions on neural networks and learning systems* **28**(10), 2222–2232.

Greff, K., Srivastava, R. K., Koutník, J., Steunebrink, B. R. & Schmidhuber, J. (2017), 'LSTM: A Search Space Odyssey', *IEEE Transactions on Neural Networks and Learning Systems* **28**(10), 2222–2232.

Gungor, V. C., Sahin, D., Kocak, T., Ergut, S., Buccella, C., Cecati, C. & Hancke, G. P. (2011), 'Smart grid technologies: Communication technologies and standards', *IEEE Transactions on Industrial Informatics* **7**(4), 529–539.

Hochreiter, S. & Schmidhuber, J. (1997*a*), 'Long short-term memory', *Neural computation* **9**(8), 1735–1780.

Hochreiter, S. & Schmidhuber, J. (1997*b*), 'Long Short-Term Memory', *Neural Computation* **9**(8), 1735–1780.

Hu, J., Shan, Y., Yang, Y., Parisio, A., Li, Y., Amjady, N., Islam, S., Cheng, K. W., Guerrero, J. M. & Rodríguez, J. (2023), 'Economic model predictive control for

microgrid optimization: A review', *IEEE Transactions on Smart Grid* **15**(1), 472–484.

IEEE Standards Association (2011), 'IEEE guide for smart grid interoperability of energy technology and information technology operation with the electric power system (eps), end-use applications, and loads'. Standard IEEE 2030-2011.

Jais, I. K. M., Ismail, A. R. & Nisa, S. Q. (2019), 'Adam optimization algorithm for wide and deep neural network.', *Knowl. Eng. Data Sci.* **2**(1), 41–46.

Jordan-Korte, K. (2011), *Government promotion of renewable energy technologies*, Springer.

Kadam, J. V. & Marquardt, W. (2007*a*), Integration of economical optimization and control for intentionally transient process operation, *in* 'Assessment and future directions of nonlinear model predictive control', Springer, pp. 419–434.

Kadam, J. V. & Marquardt, W. (2007*b*), Integration of economical optimization and control for intentionally transient process operation, *in* 'Assessment and Future Directions of Nonlinear Model Predictive Control', Vol. 358 of *Lecture Notes in Control and Information Sciences*, Springer, Berlin, Heidelberg, pp. 419–434.

Kelleher, J. D. (2019), *Deep learning*, MIT press.

Kularatna, N. & Gunawardane, K. (2021), *Energy storage devices for renewable energy-based systems: rechargeable batteries and supercapacitors*, Academic Press.

Lasseter, B. (2001), Microgrids [distributed power generation], *in* '2001 IEEE power engineering society winter meeting. Conference proceedings (Cat. No. 01CH37194)', Vol. 1, IEEE, pp. 146–149.

Limon, D., Pereira, M., De La Peña, D. M., Alamo, T. & Grosso, J. M. (2014), 'Single-layer economic model predictive control for periodic operation', *Journal of Process Control* **24**(8), 1207–1224.

Liu, X., Cheng, X., Wang, T., Wang, D. & Chen, B. (2012), 'Cyber security and privacy issues in smart grids', *IEEE Communications Surveys & Tutorials* **14**(4), 981–997.

Ma, Z., Wang, C., Li, X. & Zhang, L. (2014), 'Model predictive control for the operation of a distribution network with distributed generation', *IEEE Transactions on Smart Grid* **5**(1), 303–311.

Mayne, D. Q., Rawlings, J. B., Rao, C. V. & Scokaert, P. O. (2000), 'Constrained model predictive control: Stability and optimality', *Automatica* **36**(6), 789–814.

Mohsenian-Rad, A.-H., Wong, V. W., Jatskevich, J., Schober, R. & Leon-Garcia, A. (2010), 'Demand response in smart grids: A survey', *IEEE Communications Magazine* **49**(12), 68–75.

Muske, K. R. (1997), Steady-state target optimization in linear model predictive control, *in* 'Proceedings of the 1997 American control conference (Cat. No. 97CH36041)', Vol. 6, IEEE, pp. 3597–3601.

NVIDIA Corporation (2023), 'CUDA Deep Learning Training Guide'.
URL: *https://docs.nvidia.com/deeplearning/performance/index.html*

Olama, A., Mendes, P. R. & Camacho, E. F. (2018), 'Lyapunov-based hybrid model predictive control for energy management of microgrids', *IET Generation, Transmission & Distribution* **12**(21), 5770–5780.

Pereira, M., De La Pena, D. M. & Limón, D. (2017), 'Robust economic model predictive control of a community micro-grid', *Renewable Energy* **100**, 3–17.

Pereira, M., Limon, D., de la Peña, D. M., Valverde, L. & Alamo, T. (2015), 'Periodic economic control of a nonisolated microgrid', *IEEE Transactions on industrial electronics* **62**(8), 5247–5255.

Petrollese, M., Valverde, L., Cocco, D., Cau, G. & Guerra, J. (2016), 'Real-time integration of optimal generation scheduling with mpc for the energy management of a renewable hydrogen-based microgrid', *Applied Energy* **166**, 96–106.

Prechelt, L. (1998), Early Stopping — But When?, *in* 'Neural Networks: Tricks of the Trade', Springer, pp. 55–69.

Rawlings, J. B., Angeli, D. & Bates, C. N. (2012), Fundamentals of economic model predictive control, *in* '2012 IEEE 51st IEEE conference on decision and control (CDC)', IEEE, pp. 3851–3861.

Rodrigues, R. F. (2021), 'Centro cultural beija-flor: intervenção no centro cultural de guanambi', PDF. Estudo Preparatório de Trabalho de Curso (Arquitetura e Urbanismo) – Pontifícia Universidade Católica de Minas Gerais, Campus Liberdade, Belo Horizonte, 2021.

Roychoudhury, S., Deb, A., Sarkar, G. & Bera, J. (2014), 'Virtual laboratory for performing tests on a single-phase power transformer', *IETE Journal of Education* **55**(1), 11–25.

Singh, S. N. (2008), *Electric power generation: transmission and distribution*, PHI Learning Pvt. Ltd.

Smith, L. N. (2017), Cyclical Learning Rates for Training Neural Networks, *in* 'IEEE Winter Conference on Applications of Computer Vision (WACV)', pp. 464–472.

Tatjewski, P. (2008), 'Advanced control and on-line process optimization in multilayer structures', *Annual Reviews in Control* **32**(1), 71–85.

Vattanapuripakorn, W., Sonsupap, S., Khannam, K., Bamrungwong, N., Kaewkhiaw, P., Sarasamkan, J. & Bubphachot, B. (2022), 'Advanced electric battery power storage for motors through the use of differential gears and high torque for recirculating power generation', *Clean Technologies* **4**(4), 987–1000.

Xiao, W., Dunford, W. G. & Capel, A. (2004), A novel modeling method for photovoltaic cells, *in* '2004 IEEE 35th Annual Power Electronics Specialists Conference (IEEE Cat. No. 04CH37551)', Vol. 3, IEEE, pp. 1950–1956.

Yan, Y., Qian, Y., Sharif, H. & Tipper, D. (2013), 'A survey on smart grid communication infrastructures: Motivations, requirements and challenges', *IEEE Communications Surveys & Tutorials* **15**(1), 5–20.

Ying, C.-M. & Joseph, B. (1999), 'Performance and stability analysis of lp-mpc and qp-mpc cascade control systems', *AIChE Journal* **45**(7), 1521–1534.

York, R. (2016), 'Decarbonizing the energy supply may increase energy demand', *Sociology of development* **2**(3), 265–272.

Zanin, A. C., De Gouvea, M. T. & Odloak, D. (2002), 'Integrating real-time optimization into the model predictive controller of the fcc system', *Control Engineering Practice* **10**(8), 819–831.

Zhang, G. P. (2003), 'Time series forecasting using a hybrid arima and neural network model', *Neurocomputing* **50**, 159–175.

Zhang, Y., Zhang, T., Wang, R., Liu, Y. & Guo, B. (2015), 'Optimal operation of a smart residential microgrid based on model predictive control by considering uncertainties and storage impacts', *Solar Energy* **122**, 1052–1065.

Zheng, Y., Li, S. & Tan, R. (2017), 'Distributed model predictive control for on-connected microgrid power management', *IEEE Transactions on Control Systems Technology* **26**(3), 1028–1039.

UFBA
UNIVERSIDADE FEDERAL DA BAHIA
ESCOLA POLITÉCNICA
PROGRAMA DE PÓS-GRADUAÇÃO EM ENGENHARIA INDUSTRIAL - PEI
Rua Aristides Novis, 02, 6º andar, Federação, Salvador-BA
CEP: 40.210-630
Telefone: (71) 3283-9800
E-mail: pei@ufba.br
Home page: http://www.pei.ufba.br